Mechanistic Insights towards the Electrochemical Reduction of Carbon Dioxide to Methanol Facilitated by Benzannulated Pyridine and Dihydropyridine Additives

By

Patrick Kendall Giesbrecht

A Thesis submitted to the Faculty of Graduate Studies

of the

University of Manitoba

in partial fulfillment of the requirements of the degree of

Master of Science (M.Sc.)

Department of Chemistry

University of Manitoba

Winnipeg

ABSTRACT

The ability to recycle carbon dioxide (CO_2) to liquid fuels such as methanol offers the potential for meeting global energy demands in a sustainable fashion. Coupling of this process to renewable energy sources electrochemically is one promising approach, where the interaction of the (photo)electrode and electrocatalyst is vital for ensuring high selectivity and efficiency for the reduction of CO_2 to one product, with minimal external energy input.

As such, this work investigates the ability of benzannulated pyridines (ANHs) and isolable dihydropyridines (DHPs) towards electrochemical reduction of CO_2. The DHPs and ANHs investigated were found to reduce CO_2 to methanol and formic acid at comparable efficiencies, providing the first experimental evidence for the participation of DHPs in electrochemical CO_2 reduction. Electrochemical reduction of formic acid to methanol using ANHs and DHPs was also conducted, with simultaneous generation of a DHP from the ANH under CO_2 reducing conditions.

ACKNOWLEDGEMENTS

First and foremost, I want to thank my supervisor, Dr. David E. Herbert for all the knowledge, guidance, and support he has given me. Throughout the last few years, Dr. Herbert has helped me grow as a scientist, patiently letting me wander through a forest of ideas while ensuring that I never lost sight of the end goal; teaching me to be critical every step of the way.

I would like to thank my committee members, Dr. Georg Schreckenbach and Dr. Derek Oliver. You have kept me on track throughout the last two years, and I thank you for all of your input and considerations throughout my Master's degree.

To all the past and former members of the Herbert Group that I have had the pleasure to work, interact and discuss chemistry with. You guys made going to the lab a fun thing to do. In no particular order: Jason Braun, Peter Trokajlo, Pavan Mandapati, Rajarshi Mondal, Issiah Lozada, Talon Murray, Oscar Sze, Ravina Moirangthem, Kevin Szkop, Thorben Haubold, Jan Makow, Bin Huang, Gabriel Martins da Silva Almeida Duarte, Gabrielle Wilson, Michael Adeyemi, and Onkar Singh Kang. I expect nothing but great things from you guys, and wish you all the best.

To all the colleagues that I've interacted with and had the pleasure of knowing/working with over the past few years, in no particular order: Joey Lussier, Arzoo Lussier, Ewan McRae, Matt McDougall, Jorge Duorado, Dr. Dave Davidson, Kirk Marat, Tom Ward, Dr. Mario Bieringer, Dr. Gregg Tomy, Dwayne Chrusch, Sridhar Majety, Dr. Rebecca Davis, Dr. Jaime Ritch, Dr. Kevin McEleney, Jennifer Low McEleney, Dr. Carl Bartels, Dr. Scott Kroeker, Lesa Cafferty, Dr. Joe O'Neil, Krystyna Koczanski, Kirill Levin, Jeffery Perkins, Sophia Schreckenbach, Tristan Smythe,

Xiaobin, Navneet, Thor Halldorson, Dr. John Sorenson, Dr. Sean McKenna, Dr. Horace Luong, Dr. Oleg Roussak, Dr. James Xidos, Abdul Khan, Ravinder Sidhu, Nasser Rahimi, Eric Cuthbert, Nan Zhang, Andrew, Yuri, Tanner, Dr. Jennifer van Wijngaarden, Dr. Mazdak Khajehpour, Amit Kour, Robin, Vaibhav, Sharon Mullen, and Keith Travis.

I would be disingenuous if I did not acknowledge those that helped me throughout my undergraduate degree before I entered the Master's Program; in particular Dr. Michael Freund, who took on a young and naïve kid early on and sparked his interest in research, as well as the rest of the former Freund group: Jared Bruce, Mike McDonald, Megan McClarty, Iman Yahyaie, Ramesh Kumar, Shaun Ryman, and Akin Iyogun.

I would finally like to thank my family; my grandparents Oma and Opa Friesen, my dad Dan, my mom Karen, my siblings Jacqueline, Steve & Andrea, Danny & Vanessa, and their kids Adan, Matt, Lauren, Arya; and my friends: the 'Physics Crew' (Scott, Simon, Chris, A.J., Dan), Keagan, Kelvin, Justin, James, and Kavi. You guys have had my back since day one, and I just want to thank you for all of your support throughout the last few years.

I would also like to thank NSERC and the University of Manitoba for all the financial support you have provided for me to conduct this research over the last few years.

TABLE OF CONTENTS

LIST OF TABLES

LIST OF FIGURES

LIST OF COPYRIGHTED MATERIAL*

*** ALL COPYRIGHTED MATERIAL APPEARING IN CHAPTER 2 AND THE APPENDIX OF THIS THESIS HAS BEEN ORIGINALLY PRODUCED AND PUBLISHED BY THE AUTHOR OF THIS THESIS, AND PERMISSION HAS BEEN GRANTED FROM THE ORIGINAL PUBLISHERS AND AUTHORS FOR THEIR USE IN THIS THESIS.**

LIST OF ABBREVIATIONS

[cat]	Catalyst concentration, in M	$J_{ANH/[ANH-H]+}$	Current density of ANH redox couple, in mA cm^{-2}
[sub]	Substrate concentration, in M	J_{CO2}	Current density for CO_2-only, in mA cm^{-2}
% (v:v)	Percent by volume	$J_{CO2+ANH}$	Sum of ANH and CO_2 current densities, in mA cm^{-2}
%FE	Faradaic Efficiency	J_{HH}	^1H NMR coupling constant, in Hz
A	Geometric Area in cm^2	k_{cat}	Rate constant for catalysis
AA	Acetic Acid	LC	Liquid Chromatography
ANH	Aromatic *N*-Heterocycle	M/Z	Mass-to-charge ratio
Ar	Argon	mA	milliAmpere
atm	Atmosphere	mg	Milligram
bipy	Bipyridine	MHz	MegaHertz
C	Concentration in mol mL^{-1}	min	Minute
C_1	Consisting of one carbon atom	mL	Milliliter
C_2	Consisting of two carbon atoms	MS	Mass Spectrometry
CH_3OH	Methanol	n	Number of electrons
CO	Carbon Monoxide	N	Nucleophilicity number
CO_2	Carbon Dioxide	n_{cat}	Moles of catalyst
CPE	Controlled Potential Electrolysis	NHE	Natural Hydrogen Electrode
CV	Cyclic Voltammetry	NMR	Nuclear Magnetic Resonance
cyclam	1,4,8,11-tetraazacyclotetradecane	PCET	Proton-Coupled Electron Transfer
D	Diffusion coefficient in $cm^2\ s^{-1}$	PCHT	Proton-Coupled Hydride Transfer
d	Doublet	pK_a	Acid dissociation constant
Da	Dalton	pK_b	Base dissociation constant
dd	Doublet of doublets	ppm	Parts per million
DHP	Dihydropyridine	PS	Photosensitizer

DSSC	Dye-sensitized solar cells	PT	Proton Transfer
E^0	Thermodynamic Redox Potential, in V	Pt	Platinum
$E_{1/2}$	Experimental Redox Potential, in V	Py	Pyridine
$E_{applied}$	Applied Potential, in V	Q	Charge, in C
E_{peak}	Peak Potential, in V	Q_{prod}	Charge Passed for Product formation, in C
$E_{solvent}$	Solvent Overpotential, in V	Q_{tot}	Total Charge Passed, in C
F	Faraday's Constant, in C mol^{-1}	R	Ideal Gas Constant, in J K^{-1} mol^{-1}
FA	Formic Acid	RVC	Reticulated Vitreous Carbon
FcH	Ferrocene	s	Second
FID	Flame Ionization Detection	SCE	Saturated Calomel Electrode
GC	Gas Chromatography	SERS	Surface Enhanced Raman Spectroscopy
GC-FID	Gas Chromatography-Flame Ionization Detection	STM	Scanning Tunneling Microscopy
GCE	Glassy Carbon Electrode	T	Temperature, in K
H_2	Hydrogen	t	Triplet
HA	Brønsted Acid	td	Triplet of doublets
H_{ads}	Surface adsorbed Hydride	THF	Tetrahydrofuran
HCOOH	Formic Acid	TOF	Turnover frequency, in hr^{-1}
HPLC	High-Pressure Liquid Chromatography	TON	Turnover number
HSQC-DEPT	Heteronuclear Single Quantum Coherence-Distortionless Enhancement by Polarization Transfer	UV	Ultraviolet
HT	Hydride Transfer	V	Volt
I_{cat}	Catalytic current, in mA	Z	Number of electrons
I_{Pa}	Peak anodic current, in mA	η	Overpotential, in V
I_{Pc}	Peak cathodic current, in mA	ν	Scan rate, in mV s^{-1}
IR	Infrared	Γ	Surface coverage of electrode by redox active species
J	Current density, in mA cm^{-2}	$\Omega * cm$	Unit for resistivity of solution

CHAPTER 1: INTRODUCTION

1.1 The Need for Alternative Energy

The development and implementation of alternative energy sources is one of the biggest challenges facing the scientific community today in order to accommodate the projected increase in global energy consumption from 15 TW to 40 TW by 2050 in a sustainable, carbon-neutral fashion.[1] Current implementation of alternative energy sources involve mechanical methods such as wind and hydroelectric; thermal methods such as nuclear, and solar energy.[2] However, while the majority of the mechanical methods exhibit high energy conversions (90% mechanical-to-electrical conversion efficiency), they still can not compensate for the total increase in the projected energy consumption, with hydroelectric and wind projected to only contribute ~8 TW combined.[1] Nuclear energy offers the best alternative energy that can compensate for the increased energy demand without being dependent on external environmental factors (weather, geological location). The collection efficiency of the thermal energy generated is low (33%), however, with implementation of the ~10 000 nuclear plants required to meet the 40 TW goal not possible due to time constraints (1 plant must be built every 1.6 days until 2050), the economic feasibility of such a feat ($4-9 billion per reactor), and the exhaustion of terrestrial uranium sources.[1] Due to the enormous amount of incident energy on Earth by the Sun (1.2 $x10^5$ TW), the ability to extract electrical energy from solar radiation using photovoltaics, even at low efficiencies, is extremely appealing, but suffers from a host of environmental factors (clouds, dust, temperature) and safety concerns due to the introduction of toxic substances such as CdTe, a common solar harvesting material, to the environment.[3]

One of the major limitations of all the alternative energy sources currently being explored is their ability for long-term energy storage and transport. Due to the high extraction efficiency of electrical energy by mechanical methods (e.g. hydroelectric), most nuclear and hydroelectric plants store any excess energy generated in the form of hydroelectricity or a flywheel.[4] These methods suffer from the inability to transport the energy produced or use directly as a transportation fuel, and require large electric grid networks for efficient storage, with storage lifespans on the order of days to months. Other approaches involve batteries (e.g. Li-ion), which allow for longer storage times and the ability for electrical energy to be transported and stored off-site. However, battery storage suffers from its own host of problems, including a low specific energy and energy density that limits use in transportation (Figure 1.1), degradation of the electrode materials, slow discharge over time (1-2% per month), and the use of potentially toxic, and explosive materials such as lithium, perchlorate salts, and propylene carbonate.[5] Furthermore, the energy cost, or energy debt, of battery technology is still equivalent to the amount it is capable of storing, limiting its viability as a large-scale, long-term 'green' energy storage device.[6] By instead storing alternative energy in the form of chemical fuels, a more transportable and long-term fuel can be developed, analogous to the fossil fuels utilized today.[3a, 7] In the case of solar energy storage, the production of a solar fuel is intriguing due to the possibility of producing liquid fuel sources in remote areas such as Northern Canada, reducing the need of a centralized electrical grid while helping develop isolated areas both at home and globally.[8]

1.2 Alternative Chemical Fuels.

Current approaches to the development of alternative chemical energy carriers to fossil fuels largely focus on hydrogen gas, where the only combustion product on

utilization is water.[9] The majority of hydrogen being produced today involves steam reforming of fossil fuels, however, resulting in a large amount of emitted CO_2, increasing the environmental cost of hydrogen utilization.[10] Thus, there has been a big push towards investigating the production of hydrogen gas through electrolysis of water, or water-splitting, thereby creating a transportable, carbon-free, and more environmentally friendly fuel source.[1] Hydrogen, due to its gaseous nature has a low energy density compared to fossil fuels (Figure 1.1), which can be increased slightly when pressurized to form a liquid.[11] This property makes hydrogen an ideal fuel source for on-site storage similar to natural gas or methane, but a poor fuel for transportation purposes. Implementation of H_2 as a fuel requires the development of novel combustion engine architectures and hydrogen storage infrastructure, and is the major limitation for large-scale implementation. The development of a sustainable carbon-based liquid fuel instead would provide an energy feedstock that could easily be transported and implemented in both modern-day infrastructure and internal combustion engines, while supplying a higher energy density and specific energy than that of battery or hydrogen storage technologies.

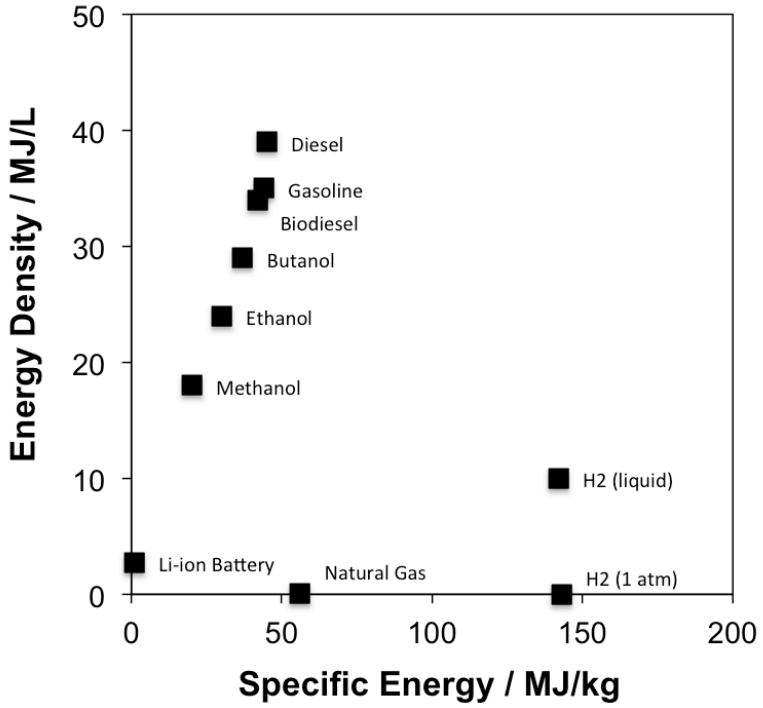

Figure 1.1. Energy Density and Specific Energy of Common Chemical and Battery Energy Sources.[5c, 11]

To do this, one has to do no more than look at the reduction of CO_2 to liquid fuels such as formic acid, methanol, and ethanol.[12] By recycling CO_2 to generate a fuel source, a sustainable, potentially carbon-neutral energy source could be used, minimizing additional CO_2 generated from fuel consumption. Such a system offers the benefits of maintaining use of modern infrastructure designed for carbon-based fuels while also reducing the reliance on fossil fuels, diversifying the carbon-based fuel market. Due to the stability of CO_2, however, a large energy barrier exists towards CO_2 reduction, with a wide resulting product distribution (*vide infra*). One promising avenue towards CO_2 reduction to value-added products involves the reduction of CO_2 to CO, shown in Figure 1.2, where only 2 protons (H^+) and $2e^-$ are required, with the generation of a water molecule as a byproduct.[12-13] Generation of CO allows for easy extraction from any solid or liquid systems utilized given its gaseous nature, simplifying post-production

purification processes. While CO itself is not useful as a fuel, further refinement through the Fischer-Tropsch process, a technique readily available at the industrial level, can be used to produce liquid hydrocarbons that can be readily used as a fuel source.[14]

Similar to the reduction of CO_2 to CO, another $2H^+/2e^-$ process that can occur is the reduction of CO_2 to formic acid, HCOOH, without the loss of water. By itself, HCOOH offers the ability to store hydrogen as a liquid under ambient conditions (4 wt%), removing the necessity of pressurized H_2 tanks.[15] Extraction of H_2 from HCOOH is easily achieved through formic acid dehydrogenation processes, whereby CO_2 is regenerated once more.[16] Since no byproducts are generated (i.e. no water generated), this offers a reversible H_2 storage system. HCOOH is non-toxic, has low flammability, and is an environmentally friendly chemical, reducing the impact of major spillages. These properties would allow a safe method of transport of H_2 as an energy source from site-of-production to site-of-distribution via ground or water transport.[16]

As formic acid offers hydrogen storage as a liquid, the use of formic acid as a fuel is also being explored in an effort to diversify the fuel market, with current research exploring the viability of formic acid fuel cells.[17] While formic acid shows low combustibility rates relative to fossil fuels or H_2 itself, any inefficiencies that can arise from H_2 extraction from formic acid processes are avoided, while providing a carbon-based fuel without the presence of toxic nitrogen oxides (NO_x) or sulfur-based compounds being burnt, the byproducts of which can be potent greenhouse gases in their own right. The energy density for formic acid is low, however, and is comparable to that of hydrogen, limiting its use as a transport fuel.[15] Further refinement of formic acid can result in higher energy density fuels such as methanol, a more attractive alternative for

CO_2-based fuels. Given the solubility of formic acid with water and other organic media, however, extraction of formic acid from solutions used for synthesis is challenging, with most methods involving either distillation or organic solvent extractions.[18]

Methanol is one of the most attractive products to generate from CO_2 due to its prominence as a solvent, a synthetic precursor, and its promising energy density and specific energy in relation to current liquid fuels being used today.[15, 18b] Since methanol exhibits similar physical properties to fossil fuels, implementation of methanol as a fuel is simplified, with only minor modifications needed to current combustion engine infrastructure. Given the $6H^+/6e^-$ necessary for methanol formation, however, production of methanol as the sole product from CO_2 reduction is challenging, with the possibility of forming byproducts and intermediates such as formic acid or formaldehyde. Additionally, given its solubility with water and organic media, methanol extraction from solution, similar to formic acid, is another challenging step.

Methanol as a fuel has a low cetane value (5), i.e. a slow combustion rate, making it viable for use in gasoline-based combustion engines (cetane value of 0-5), but incompatible for diesel engines (cetane value of 40-55).[15] One method for enhancing the cetane value of the methanol produced while also increasing the energy density is through dehydrative coupling of methanol under acidic conditions, producing dimethyl ether.[15] Dimethyl ether has a high cetane value (>55), making it more compatible with diesel engines.[19] Unlike most ethers, dimethyl ether does not undergo peroxy-degradation under ambient conditions, and is a gas at room temperature (melting point of -25 ^oC) similar to that of propane. By pressurizing dimethyl ether in a similar fashion as for

propane tanks, the use of dimethyl ether as a liquid fuel can be achieved, and could also be implemented in propane-based engines with minor modifications.

1.3 Current Approaches to CO_2 Reduction

A few of the reduction processes that CO_2 can undergo are shown in Figure 1.2 along with their respective redox potentials, where a carbon-based product and water are generated.[13] While the redox potentials of these events are within 0.3 V of proton reduction under the same conditions (-0.41 V vs. NHE), there exist kinetic barriers to product formation due to the destabilization of CO_2 from a linear compound to a bent species, as well as the requirement for multiple protons/electrons to encounter CO_2, creating a competition between proton and CO_2 reduction processes in aqueous environments. This kinetic barrier results in large amounts of energy in excess of the thermodynamic potential (η, overpotential) required to drive this reaction, unless suitable (electro)catalysts can be found that can access lower energy mechanisms (Figure 1.2).[20] Furthermore the solubility of CO_2 as a substrate and particular reductive pathway taken by CO_2 is strongly dependent on the solvent mixture used. In aqueous environments, low concentrations of dissolved CO_2 are observed (30 mM), whereas in organic media, a higher solubility of CO_2 is observed (0.3 M in acetonitrile).[21] Production of formic acid can be enhanced in water compared to organic media, due to the stabilization of formic acid production by solvating water molecules.[18b] Introduction of an electrocatalyst to the solution is anticipated to lower the energy barriers/overpotential towards product formation, potentially increase the efficiency and/or increase the selectivity towards the desired reductive process, with the electrocatalyst either in solution or adsorbed/appended onto a surface.[20, 22]

In order for an electrocatalyst to be viable for catalyzing a reduction process, the following criteria must be met: (i) fast electron transfer to/from the electrocatalytic species, (ii) fast chemical kinetics when reacting with CO_2, (iii) a good thermodynamic match between the redox potential at which this occurs for the electrocatalyst and the CO_2-reduction process desired.[20] Furthermore, the electrocatalyst must be cheap, robust, and compatible with the type of catalytic system employed. In the case of CO_2 reduction, these types of systems include (i) photochemical, (ii) chemical, (iii) electrochemical, and (iv) photoelectrochemical frameworks.

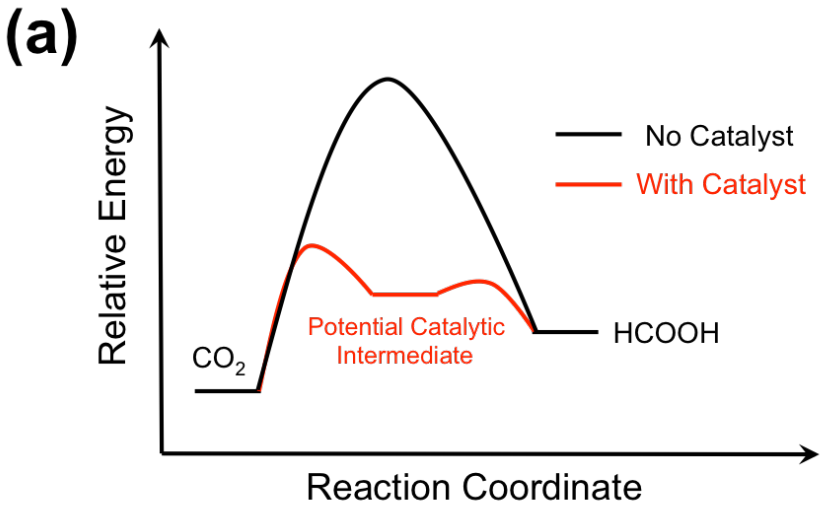

(b)

$$CO_2 + 2H^+ + 2e^- \longrightarrow CO + H_2O \qquad E^0 = -0.53\ V$$

$$CO_2 + 2H^+ + 2e^- \longrightarrow HCO_2H \qquad E^0 = -0.61\ V$$

$$CO_2 + 6H^+ + 6e^- \longrightarrow CH_3OH + H_2O \qquad E^0 = -0.38\ V$$

$$CO_2 + 8H^+ + 8e^- \longrightarrow CH_4 + 2H_2O \qquad E^0 = -0.24\ V$$

Figure 1.2. (a) Depiction of the reaction pathway taken for CO_2 reduction to HCOOH, as an example, in the absence (black) and presence (red) of an (electro)catalyst. Lower energy pathways can be accessed with an electrocatalyst, forming possible intermediates to do so. (b) Electrochemical CO_2 reduction pathways producing hydrogenated products in pH 7 aqueous solution, vs. normal hydrogen electrode (NHE), 25 °C, 1 atm, 1 M solutes.[13]

1.3.1 (Photo)chemical Approaches to CO_2 Reduction

One of the simplest designs for CO_2 reduction involves the coupling of light to electron transfer from a donor to CO_2 in a photochemical system (Figure 1.3). To help lower the energy barrier to this process, the reduction of CO_2 is typically conducted under acidic conditions, enabling proton transfer to CO_2.[13, 23] Typical designs for a photochemical system involve a photosensitizer (PS), an electrocatalyst, a sacrificial proton/electron donor that could also act as the PS, and CO_2. The reaction is initiated through light absorption by the PS, bringing it into an excited state. The reduction process can then occur in one of two scenarios: (i) the electron donor donates an electron to the excited PS, which in turn transfers the electron to the catalyst, or (ii) the excited PS transfers an electron to the catalyst, with the electron donor reducing the newly oxidized PS. The catalyst then transfers the electron to CO_2 either separately or coupled with a proton transfer. Typical PSs include organic dyes such as *p*-terphenyl, or organometallic complexes such as ruthenium(II) tris(bipyridine) salts ($[Ru(bipy)_3]^{2+}$); compounds that are able to strongly absorb in the UV-visible region of the light spectrum and exhibit strongly negative reduction potentials in their excited states.[13, 23]

The selection of an electrocatalyst depends on the desired reduction process for CO_2. High selectivity towards CO production is observed in systems with Re/Ru(bipy)$(CO)_3$X-based electrocatalysts in organic media, with moderate turnover numbers (TON) reported (TON ~ 100). By simply altering either the metal centre (Re/Ru to Mn) or the ligand framework employed, such as going from a bipy-based framework to a 1,4,8,11-tetraazacyclotetradecane (cyclam) ligand, the production of formate, $HCOO^-$, could instead be observed (Figure 1.3).[23] In an even simpler system, an aqueous mixture

of pyridine, KCl and a sacrificial reductant, ascorbate, in the presence of a $[Ru(bipy)_3]^{2+}$ dye exhibits the ability to produce formic acid and methanol at low TONs (0.1-10).[24]

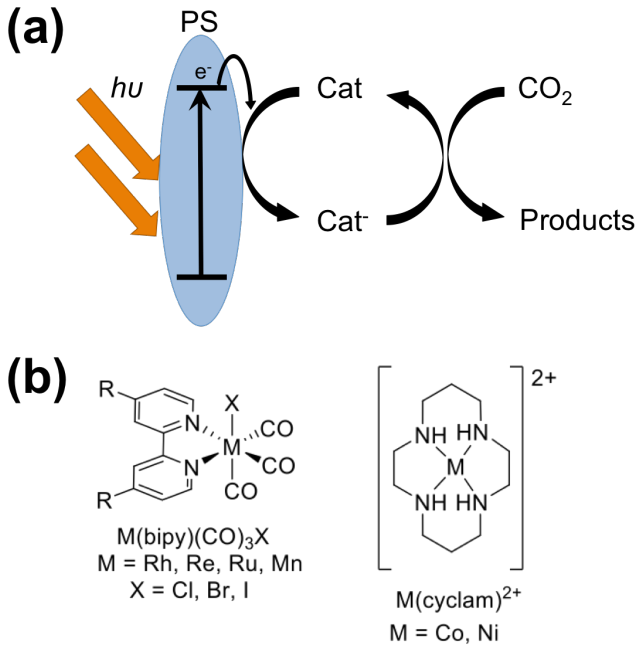

Figure 1.3. (a) General schematic for photochemical reduction. Light is absorbed by the photosensitizer (PS) photoexciting an electron that is transferred to the electrocatalyst in solution. The electrocatalyst then transfers the electron to CO_2 along with possible proton transfers to generate CO_2 reduced products. (b) Chemical structures of $M(bipy)(CO)_3X$ and cyclam complexes used in examples of photochemical catalytic systems.

While photochemical systems are simple in design, the current benchmark standards for homogenous catalytic reactions for CO_2 reduction still require the use of precious metals such as Rh, Ru and Ir, or involve complex ligand design such as developing biologically relevant cubane structures.[12] More generally, photochemical systems also require stoichiometric amounts of sacrificial electron/proton donors, with the strong likelihood of degradation of the PS or electrocatalyst over time. Under aqueous conditions, the pH required for CO_2 reduction must stay constant to ensure efficient H^+/e^- transfer from the electrocatalysts and donors to CO_2.[13] Some work has tried to address these issues through covalent attachment of the PS to the catalyst, forming

supramolecular structures, enhancing the charge transfer rate between complexes. These dinuclear supramolecular catalysts have also shown reasonable TONs (10-3000), and show more durability to environmental factors.[25] Furthermore, these supramolecular, as well as macromolecular assemblies have also been attached to semiconducting particles such as TiO_2 to form a hybrid system, allowing the electrons to be supplied by the TiO_2 in a method similar to dye-sensitized solar cells (DSSC),[23, 26] creating a heterogeneous photoelectrocatalytic system while helping stabilize both the PS and electrocatalyst from degradative effects that arise from staying in solution. However, the main limitation towards introduction of photochemical CO_2 reduction at the industrial scale is the low TON and turnover frequency (TOF) reported, as well as the inability of the hybrid systems to utilize water as the electron donor.[23, 25]

1.3.2 Electrochemical Approaches to CO_2 Reduction

While photochemical systems are appealing due to the simplicity of their design, they are severely limited by the requirement of a light source. By instead reducing CO_2 in an electrochemical system, other alternative energy sources such as hydroelectricity can now be coupled to chemical fuel formation. In such an electrochemical framework, a sufficiently reducing current/potential is applied to electrodes in a CO_2-saturated solution, resulting in CO_2 reduced products forming at the cathode, and oxygen or other oxidized species forming at the anode. Thus the rate and/or thermodynamic capability of the system towards CO_2 reduction can be manipulated based on the applied current/potential, allowing control of the overpotential required, and with the efficiency of the reduction process determined based on the amount of charge passed (Faradaic efficiency, %FE).[20,

[22] As with photochemical systems, the electrocatalyst can either be in solution or appended to the electrode surface.

As product formation occurs at or near the electrode surface, a few new design features are necessary for continuous large-scale production of CO_2 reduced species: (i) a method for product removal, (ii) continuous feedstock of CO_2-saturated solution, and (iii) separation of the cathode and anode to prevent product crossover and re-oxidation of the reduced compounds. This can be achieved in a flow-cell design, where a constant potential/current is applied to the system to generate products, the solution is pumped through the system, removing products from the electrode surface while providing fresh CO_2-saturated solution to the electrode surface, and with the products either collected separately (gaseous) or stored in a reservoir awaiting extraction (Figure 1.4).[18a, 27] To ensure the reduced species cannot reach the anode, a cation-exchange membrane is used to separate the electrodes and electrostatically prevent CO_2 reduced products from passing through.

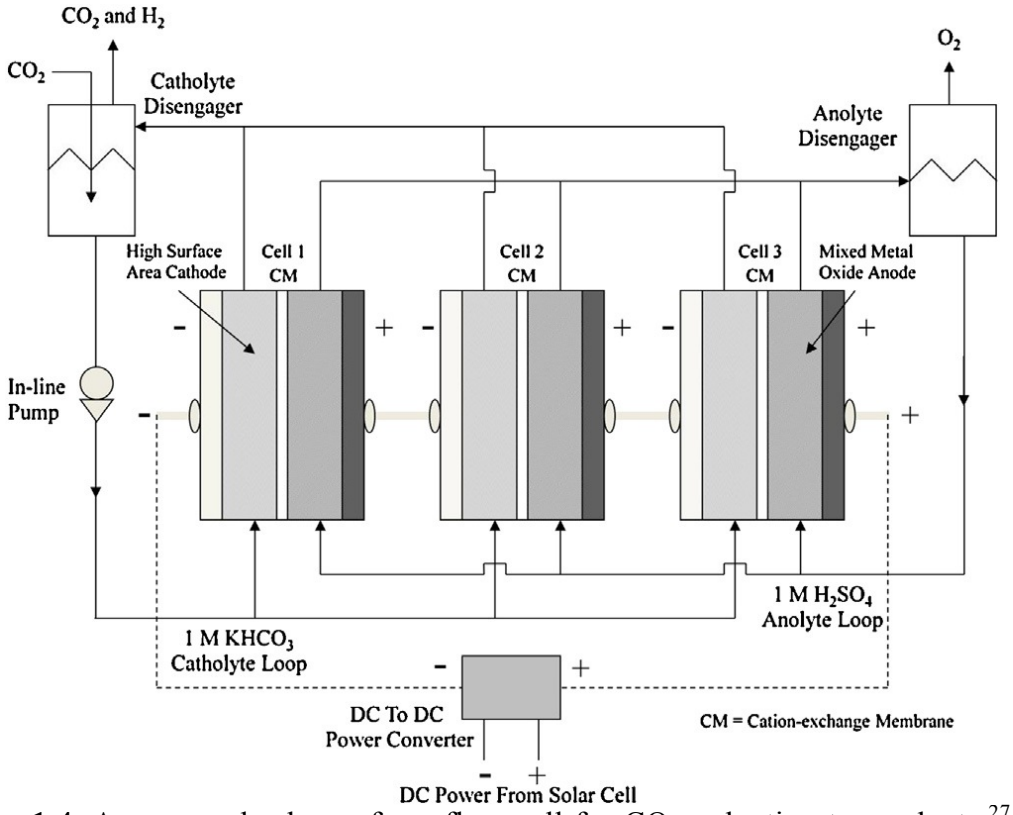

Figure 1.4. A proposed scheme for a flow cell for CO_2 reduction to products.[27] CO_2 enriched solutions pass by a high-surface area cathode, with the products then shuttled back to the catholyte reservoir. A cation-exchange membrane is used to prevent product crossover to the anode, with the anode producing oxygen to complete the system. Taken from Reference [27]. Copyright 2014 Elsevier Ltd.

As with photochemical approaches to CO_2 reduction, the application of organometallic complexes towards electrochemical CO_2 reduction is currently being actively explored. In fact, there is a large crossover of organometallic electrocatalysts being utilized in photochemical and electrochemical routes, and are briefly described in Section 1.3.1. Under electrochemical conditions, Re/Ru(bipy)$(CO)_x$-based catalysts exhibit high %FE (>90 %FE) towards CO formation at glassy carbon electrodes, with moderate reported TOFs (~100-1000 s^{-1}).[28] Furthermore, the selectivity towards CO or HCOOH generation could be manipulated by the applied potential in these cases, where more HCOOH was observed when the applied reduction potential was lowered.[28c] The selectivity and the efficiency of the reduction process can also be manipulated based on

the ancillary ligand environment used. Current 'benchmark' electrocatalysts employed in electrochemical setups still require the use of precious metals such as Rh, Re, Ru and Ir, significantly increasing the cost of production.[12] Biologically-inspired cubane complexes containing Ni, Fe and Mo show remarkable abilities to reduce CO_2 to formate or CO, but are challenging to synthesize.[12] Simpler organometallic complexes utilizing similar cheap metal centres such as Fe, Ni, Mn or Co are being explored in an effort to reduce the cost associated with organometallic complex and ligand design, but exhibit low TON and resulting TOF, limiting their application to date.[29]

In a simpler design, the reduction of CO_2 has also been shown to be electrocatalyzed by the electrode material used, obviating the need for a redox mediator. Instead of a ligand framework guiding the reduction process, the geometry of the electrode surface can be used to guide CO_2 binding and stabilize the intermediates formed, with the stabilization of the intermediates dependent on the binding energy of the electrode surface.[30] The majority of electrodes that exhibit the ability to catalyze the reduction of CO_2 are transition metals. These can be broken into three categories: (i) formic acid producing (Sn, Hg, Pb, Bi), (ii) CO producing (Au, Ag, Zn), and copper, which can result in up to 16 distinct products.[30-31] Fe, Co, and Ni are typically used in the Fischer-Tropsch process as a catalyst, but have been shown to reduce CO_2 to HCOOH and C_1 and C_2 hydrocarbons at high CO_2 pressures.[30]

Electrochemical reduction of CO_2 at Cu-electrodes has become an area of interest due to the large number of products that are generated with minimal H_2 generation and the number of different avenues in which the selectivity and efficiency of this system can be manipulated based on the applied potential, temperature, electrolyte type and

concentration, pH, and electrode surface structure. Studies involving a Cu-sheet cathode found that methane production disappeared and C_2H_4 production increased as the temperature was increased.[32] Furthermore, increasing the applied potential was found to decrease CO generation and promote hydrocarbon and alcohol formation.[33] The selectivity of reduced species was also found to be dependent on the identity of the electrolyte, with methane production promoted at concentrated solutions of bicarbonate salts.

Introduction of new surface orientations and sites/defects was also found to change the selectivity and efficiency of Cu-electrodes. Investigations of single-crystal Cu-surfaces revealed an alteration from a CH_4 formation pathway at Cu(111), to ethylene formation at Cu(100).[34] Theoretical studies have revealed that this is due to the stabilization of CO_2 reduction intermediates by the different facets observed at the different Cu surfaces.[35] Given these fundamental results, Cu-electrodes were then nanostructured and developed in a variety of manners to further investigate the role the surface structure has on the selectivity. When nanoparticulate Cu is deposited onto glassy carbon, a significant increase in the current passed at the electrode for product formation was observed, relative to at a Cu-foil under the same conditions.[36] Thus, not only can the efficiency and selectivity of the reduction mechanism be manipulated based on the surface, but also the relative current density due to the increased number of surface sites available to react with CO_2 in the nanoparticulate surface.

In a similar vein, there has been recent progress in the reduction of CO_2 at carbon electrodes, a cheaper alternative to the metallic electrodes investigated. Carbon is very inert towards both CO_2 reduction and H_2 generation, with large overpotentials associated

with both processes.[37] When the surface of the carbon electrode is nano-structured or chemically treated to introduce dopants at the surface, a significant increase in catalytic ability towards CO_2 reduction is observed.[37] For instance, when graphene quantum dot electrodes are treated to introduce N-dopants into the graphene honeycomb structure, a significant increase in the total %FE is observed (30 to 100% FE), with a wider product distribution observed.[38] Furthermore, given the well-known surface chemistry of graphene and carbon-based surfaces, the immobilization of known electrocatalysts to the surface can be achieved with relative ease, either through covalent modification or adsorptive techniques.[37, 39] While the current densities achieved at carbon-based electrodes are still low (and with them, low TONs), this approach to CO_2 reduction is expected to gain momentum and interest due to the ease of integration into industrial-scale processes.

1.3.3 Photoelectrochemical Approaches to CO_2 Reduction

Similar to a photochemical system, the reduction process occurring at the electrode surface can also be coupled to light absorption, allowing the energy necessary for the electrochemical process to be facilitated by the absorption of sunlight in a photoelectrochemical cell. Instead of a PS in solution, a p-type semiconducting photoelectrode is utilized for reducing conditions. Upon illumination, a photoexcited electron is generated in the photoelectrode, going from the conduction band to the valence band, Figure 1.5, which can then reduce the electrocatalyst at the electrode interface, with CO_2 reduction then occurring.[13] This process relies on the relative positions of (i) the valence band (ii) redox potential of the electrocatalyst and (iii) the CO_2 reduction process desired. The highest energy level should be the valence band,

allowing the electron to have sufficient enough energy to reduce the electrocatalyst, which can then reduce CO_2.

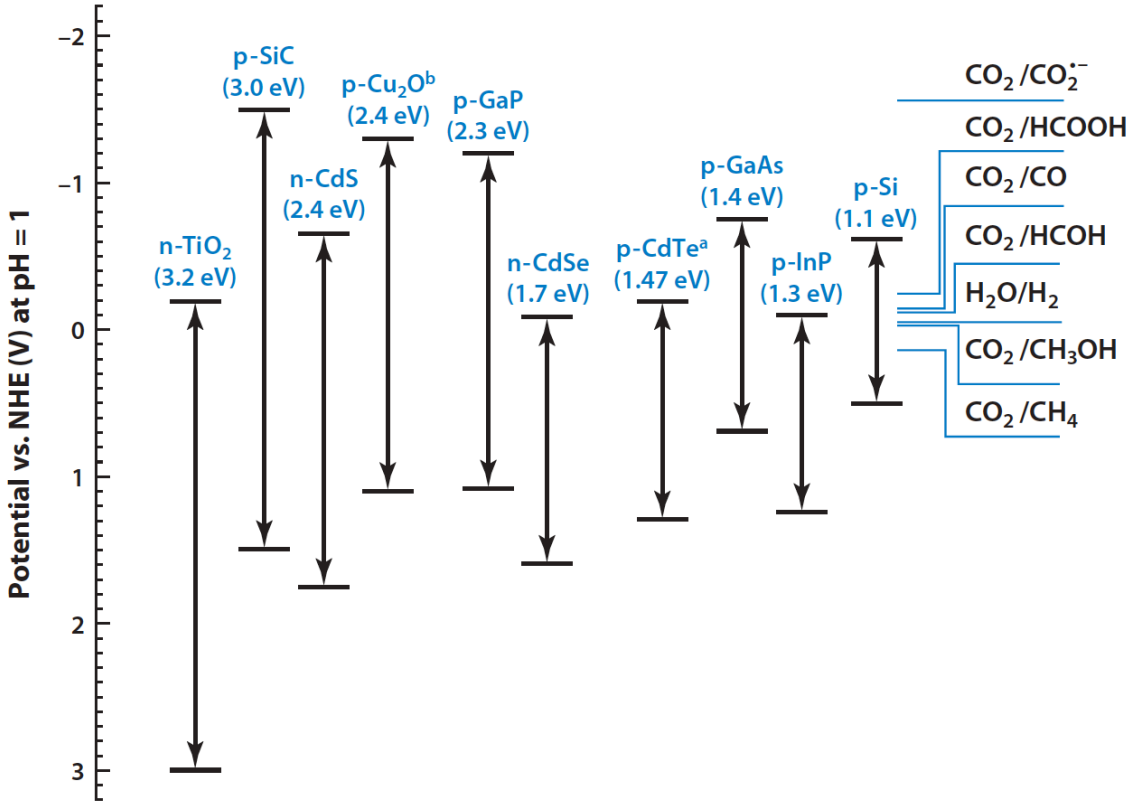

Figure 1.5. Energy Diagram depicting the Valence and Conduction Bands of Common Semiconductors in relation to the potentials required for CO_2 reduction processes. Taken from Reference [13]. Copyright 2012 Annual Reviews.

As can be seen in Figure 1.5, p-Si, an abundant semiconducting material, shows promising application towards facilitating CO_2 reduction under acidic conditions. In fact, Cu-coated p-Si electrodes have been shown to exhibit CO_2 reduction to C_1 and C_2 products with low efficiencies (10-40%) similar to that at Cu, but with a light-driven 700 mV decrease in the necessary applied potential.[40] In a similar set-up, CO_2 reduction was attempted at p-GaP electrodes with an organic additive, pyridine, in solution. Interestingly, high selectivity, high Faradaic and quantum efficiency, and a 300 mV light-driven underpotential was observed for the reduction of CO_2 to methanol.[41] Despite the

low overall TON and resulting TOF of this process, this simple system offers a promising method towards CO_2 reduction to methanol, prompting a larger investigation into pyridine-based CO_2 reduction to methanol.

1.4 Pyridine-Based CO_2 Reduction

Due to the simplicity of the design, the selective reduction of CO_2 in the presence of pyridine is an appealing concept given the remarkable ability to produce methanol with high Faradaic efficiency at p-GaP electrodes.[41] When pyridine-based CO_2 reduction was conducted at another light-absorbing electrode, pyrite, the efficiency was found to drop significantly, with HCOOH being favoured instead of methanol.[42] Studies at metallic electrodes such as Pt,[43] Pd,[44] Au,[43b, 45] Cu,[43b] and Ir[46] have also shown CO_2 reduction behavior, with efficiencies ranging from 10-40% for methanol and/or formic acid production depending on the electrode surface employed. Furthermore, studies at Pt surfaces also indicate no dependence on the applied potential towards methanol production, but rather the applied potential was found to be dependent on the electrode material used.[47] These results suggest a surface-based or surface-coupled reduction process is operative.

Cyclic voltammetry (CV) studies have been employed to investigate the electrocatalytic mechanism observable in these systems on the CV timescale. At Pt surfaces, the predominant mechanism observed under the acidic conditions is the $1e^-$ reduction associated with the pyridinium/pyridine redox couple, whereby a surface-hydride, H_{ads}, is generated upon reduction of the protonated pyridine ring, resulting in the formation of pyridine.[43a] This type of process is referred to as a 'weak acid' reduction mechanism (see Section 1.5.1).[48] When CO_2 is introduced to the system, an increase in the current passed is observed, similar to the introduction of an electrocatalytic event

observable at the CV timescale. CV analysis of this reductive process suggests it is also a solution-based $1e^-$ reduction similar to pyridine-based weak acid reduction at the electrode surface.[43a] When the rate law for the reduction of CO_2 facilitated by pyridine was investigated, a first order dependence on CO_2 and on pyridine content was observed.[49] Increasing the pyridine concentration was found to decrease the H_2 generation at the electrode surface, and promote CO_2 reduction.[50] Furthermore, the reduction potential at which this process occurs was found to also be dependent on the pyridine derivative used, whereby the potential at which this reduction takes place at is directly related to the pK_b, the base dissociation constant of the pyridine derivative, further indication of a weak-acid mechanism occurring at the CV timescale.[51] Analyses of bulk electrolyses also conclude a similar trend in the %FE for total CO_2 reduced product formation, where the compounds with the lowest pK_b exhibited the greatest selectivity towards CO_2 reduction.[52] When an alternative weak acid with a pK_a similar to pyridine was used (acetic acid) however, no CO_2 reduced species were observed, indicating that the pyridine ring plays some role in the stabilization of the CO_2 reduction intermediates.[48]

From these results, Batista and coworkers proposed a CO_2-reduction mechanism based on a weak-acid type mechanism occurring at Pt surfaces (Figure 1.6).[53] Under the acidic conditions employed (pH ~5), pyridine is protonated to form its conjugate acid, pyridinium. Pyridinium can then undergo a weak-acid reduction at the Pt surface, forming a surface-hydride (H_{ads}). This hydride undergoes an electrophilic attack by CO_2, leading to a two-electron proton-coupled hydride transfer facilitated by a secondary pyridinium ion reducing at the electrode surface, producing formic acid. Batista's model

fits well with simulated CVs by Bocarsly,[43a] as well as the CV studies conducted in his work. However, this increase in current could also be attributed to the introduction of a H_2CO_3/HCO_3^- buffer, which can artificially increase the current observed.[48] This supports the absence of current enhancement under non-aqueous conditions, where instead a decrease in the current is observed under CO_2, and contradicts the rate law determination results conducted earlier.[43b] Furthermore, studies investigating the time dependence on pyridine-based CO_2 reduction revealed that methanol could only be observed after 1 hour of bulk electrolysis, indicating that the resulting process for CO_2 reduction might also be occurring at a much slower rate.[47] Also, due to the difference in the electrode surface of Pt in comparison to p-GaP, this argument cannot explain the mechanism occurring at the p-GaP surface given the large difference in surface hydride stability at Pt compared with p-GaP electrodes.

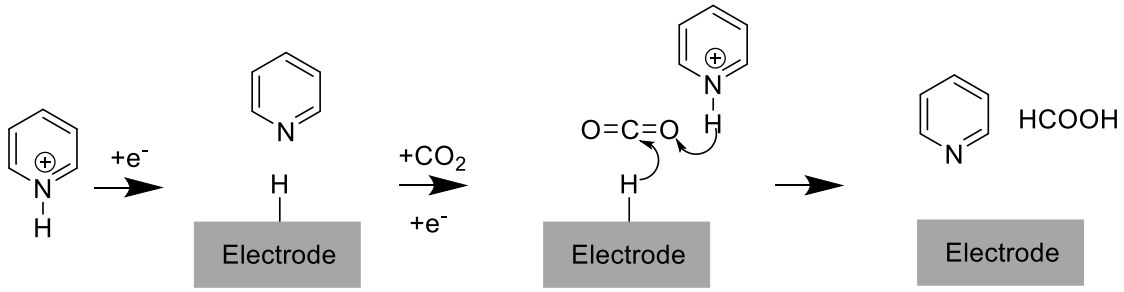

Figure 1.6. A surface-coupled CO_2 reduction mechanism facilitated by pyridine in solution, as proposed by Batista. Pyridinium reduces at the electrode surface to form pyridine and a surface hydride. A secondary pyridinium then approaches the surface in the presence of CO_2, facilitating a surface-coupled PCHT to CO_2. Adapted from Reference [53].

An alternative mechanism to help explain the CV characteristics of the pyridine (Py) reduction event under acidic conditions was investigated by Carter,[54] whereby the initial hypothesis was that the reduction of $[Py\text{-}H]^+$ occurs via one electron reduction to form a [Py-H]* radical which can then bind to CO_2, and form formic acid through a

secondary H^+/e^- transfer to CO_2, with pyridine again formed. The predicted redox potential for this event in aqueous environments is too negative (-1.4 V vs. SCE) to occur when compared to the experimental potential required for CO_2 reduction (-0.55 V vs. SCE). Instead, an alternative mechanism was determined, whereby a dihydropyridine species (DHP) was proposed to be generated at the potentials used for CO_2 reduction at Pt surfaces.[54b, 55] This DHP can then react with CO_2 in solution, forming formic acid and pyridine, with this reaction stabilized by water molecules present in solution (Figure 1.7).

Spectroelectrochemical studies investigating the reduction of pyridine/pyridinium at various electrodes indicate that a weak-surface adsorption process can occur at metallic electrodes. Analysis by surface-enhanced Raman spectroscopy (SERS) at Cu-electrodes revealed this to be adsorption of a pyridine molecule, with no dihydropyridine or pyridine-based radicals adsorbed onto the electrode surface.[43b] Further analysis of pyridine reduction under acidic and CO_2 conditions via IR-spectroscopy at Pt surfaces also indicates that no solution-phase dihydropyridine, pyridinal radical or surface-adsorbed pyridine molecules are observed.[56] Instead, CO and COOH surface sites were observed at Pt surfaces, similar to the observations of CO_2 reduction at metallic electrodes, with pyridine reported to play only a minor role in the formation of formic acid, with low methanol yields reported (<1% FE). To determine if the DHP could chemically react with CO_2, NMR-scale chemical reaction of DHP with CO_2 was investigated, with no CO_2 reduced species or H/D scrambling of the DHP observed.[51] Thus, if a DHP-species is used for CO_2 reduction, it must be a short-lived species and must require an appropriate electrochemically reducing potential and surface to react with CO_2.

While these results help explain the reduction process that is occurring at metallic electrodes, none of the reported mechanisms can be applied to p-GaP electrodes, as the surface hydrides on Pt are more labile than on p-GaP electrodes. Furthermore, the ability of pyridine to adsorb to Pt is very similar to the adsorption process predicted and observed at p-GaP electrodes. Carter and co-workers then began investigating the reduction processes of pyridine at p-GaP electrodes under CO_2-reducing conditions.[57] In brief, a secondary mechanism was developed, whereby a dihydropyridine species is formed at the p-GaP electrode surface, shown in Figure 1.7, either as a surface-adsorbed DHP or as a surface-adsorbed DHP radical, which can then react with CO_2 in a proton-coupled hydride transfer, forming HCOOH and a surface adsorbed pyridine which can desorb from the electrode surface. The reduction potential of this process is within the range necessary for CO_2 reduction to occur under the experimental conditions, with the reduction potential strongly dependent on the crystal face to which the pyridine molecule was adsorbing to, as well as the position of the hydride formation on the pyridine molecule, with the *ortho*-position calculated to be the more likely species generated at p-GaP surfaces.

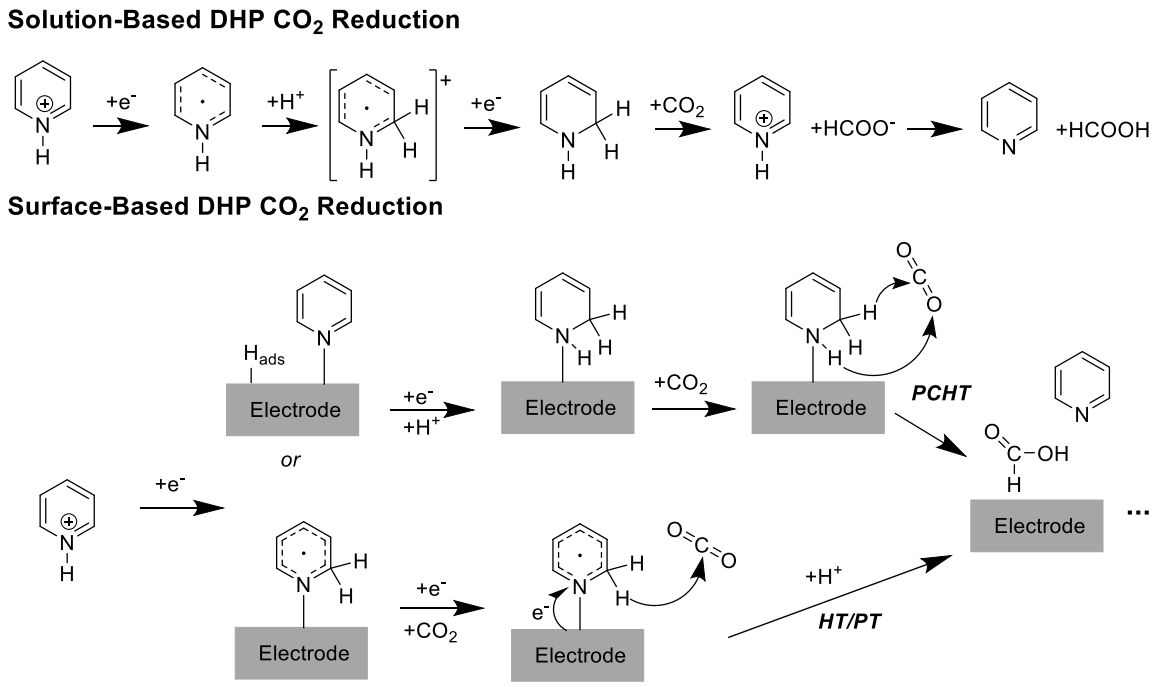

Figure 1.7. Possible DHP-based CO_2 reduction mechanisms as proposed by Carter and Musgrave.[55b] In solution, a DHP is electrochemically generated, and attacks CO_2 in a single PCHT. Alternatively, a surface-based DHP can occur, where an adsorbed DHP species can attack CO_2 at the surface in a PCHT transfer. Mechanisms displayed adapted from References [57-58].

Further work by Keith investigated the thermodynamic properties of pyridine and other aromatic *N*-heterocycles (ANH) under CO_2 reducing conditions in aqueous environment, by comparing the Pourbaix diagrams calculated for the ANHs to the Pourbaix diagram for CO_2 (Figure 1.8).[59] Instead of relying solely on the acidity of the conjugate acid, $[ANH\text{-}H]^+$, or the hydricity, i.e. the ability of the DHP, $ANH\text{-}H_2$, to act as a hydride donor; the ability to reduce CO_2 was predicted to be dictated by the position of the ANH's Pourbaix triple-point, the pH and applied potential necessary for a $ANH/[ANH\text{-}H]^+/ANH\text{-}H_2$ mixture in solution, relative to the pH and applied potential necessary for CO_2 reduction. From this work, Keith predicted the ability of other ANHs, such as quinoline, to reduce CO_2 in a similar fashion as pyridine. Thus, from a

thermodynamic consideration, the ability of the ANH to reduce CO_2 was dependent not only on the acidity of the conjugate acid, but also the hydricity of the DHP.

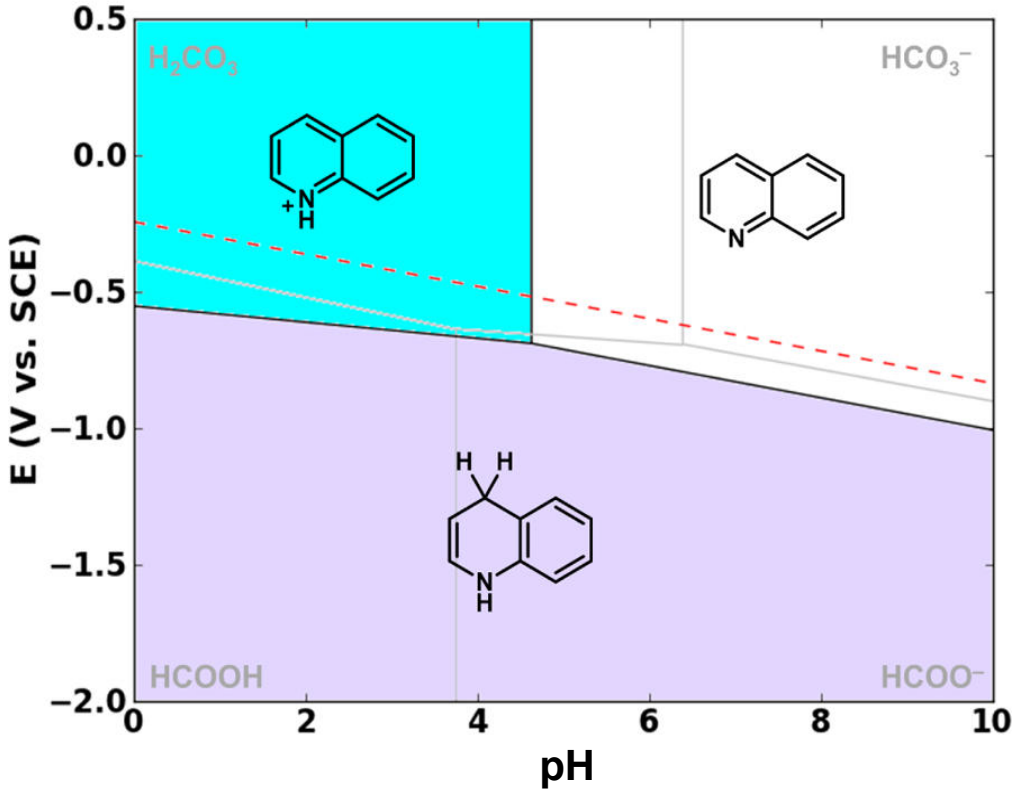

Figure 1.8. Computational Pourbaix Diagram of a potential CO_2 reducing ANH, quinoline, plotted in relation to the Pourbaix Diagram for CO_2 in aqueous conditions. The Pourbaix triple-point of the ANH, corresponding to the presence of ANH/[ANH-H]$^+$/ANH-H_2 in solution, is close to the thermodynamic reduction potential of H_2CO_3 to $HCOO^-$ under conditions relevant to pyridine-based CO_2 reduction (E ~ -0.55 V vs. SCE, pH ~ 5.3). Taken from Reference [59a]. Copyright 2016 American Chemical Society.

Given the large role DHPs appear to play in this process computationally, little has been done experimentally to verify their generation under electrochemical conditions or their ability to reduce CO_2. One study investigated the ability of mercaptopteridine to reduce CO_2 at glassy carbon electrodes, with a dihydro-mercaptopteridine species generated in solution.[60] Methanol and formic acid production in this system is under dispute, however, with no CO_2 reduced species observed via Gas Chromatography Flame

Ionization Detection (GC-FID) or Nuclear Magnetic Resonance (NMR) techniques under the same conditions when Saveant and co-workers conducted the same experiment.[61] Furthermore, computational studies investigating the thermodynamic ability of the dihydro-mercaptopteridine to reduce CO_2 to methanol observed that the energy barriers towards methanol formation is too great for the dihydro-mercaptopteridine to overcome.[62]

1.5 Electrochemical Techniques

1.5.1 Cyclic Voltammetry

Theory

Cyclic voltammetry (CV) is one of the most common methods in electrochemical methods to analyze a chemical compound or electrochemical process, where the applied potential is increased or decreased linearly with time, and the resulting current response measured (Figure 1.9).[63] When used to analyze a redox active species in solution, an increase in the current passed will occur as the potential is swept past the thermodynamic redox potential, E^0, of the redox event. Due to the competition between the kinetics of electron transfer and the mass transfer of the redox-active species to/from the electrode surface, this current response will result in a peak generated past E^0. In the reverse scan, provided the redox event is a reversible process, a similar peak will result, producing the so-called 'duck-wave', with the current peak heights being the same magnitude. In the case of quasi-reversible and irreversible processes, lower peak heights will typically be observed on the reverse scan for $1e^-$ events, as some of the oxidized/reduced species decomposed in that timeframe. The experimental potential of the redox event, $E_{1/2}$, can simply be determined by taking the average potential value of the peaks observed for

reversible and quasi-reversible processes. For irreversible processes, as there is no peak on the return scan, the $E_{1/2}$ is typically taken as the potential at half of the peak current height.[64]

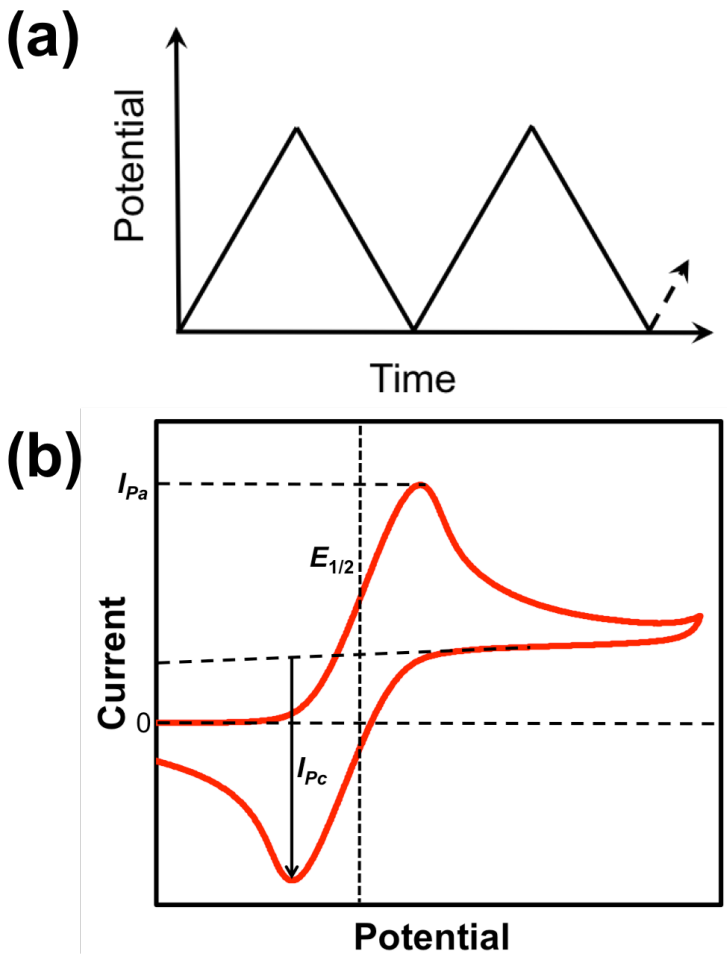

Figure 1.9. (a) Potential versus time plot during a cyclic voltammetric experiment. (b) Typical Current versus Potential plot for a reversible redox process. Determination of $E_{1/2}$ of the redox event, and the peak current associated with the onset (I_{Pa}) and return peak (I_{Pc}) is shown.

For reversible and quasi-reversible redox events, the redox event can be probed by changing the potential 'scan rate', providing a peak current dependence on the scan rate, allowing the redox process to be identified as a surface or solution-based process. For solution-based redox processes, the current is largely dependent on the diffusion of

redox active species to the electrode surface. As such, the peak current, I_P, becomes dependent on the square root of the scan rate, as defined by the Randles-Sevcik equation (Equation 1.1), where n is the number of electrons associated with the process, F is Faraday's Constant, A is the electrode surface area, C is the concentration of redox-active species in solution, D is the diffusion coefficient of the redox species, R is the ideal gas constant, T is the temperature, and ν is the scan rate.[63] In the case of a surface-based event, no diffusion of redox active species can occur, with the peak current now linearly dependent on the scan rate (Equation 1.2), where Γ is the surface coverage of the electrode by the redox active species.[63]

$$I_P = 0.4463nFAC\left(\frac{nF\nu D}{RT}\right)^{\frac{1}{2}} \quad (1.1)$$

$$I_P = \frac{n^2F^2}{4RT}\nu A\Gamma \quad (1.2)$$

CV studies can also be used to explore electrocatalytic events that are able to occur on the CV timescale in homogeneous (solution-based) and heterogeneous (surface-based) events.[64b, 65] In brief, there are four mixtures that are of interest: (a) the electrolyte only; (b) the catalyst and electrolyte; (c) the substrate and electrolyte; and (d) the catalyst, substrate and electrolyte. To properly identify if a catalytic process is indeed occurring at a particular potential, the current density observed in solution (d) must be larger than the sum of the background currents; i.e. $J_d > J_a + J_b + J_c$.

Similarly, another type of CV study that is employed to study the ability of an electrocatalyst is a CV titration.[65] In these studies, the substrate loading, or concentration, is increased, with the current response measured. A rate law for the catalytic process can be determined, provided the catalytic event occurs at the redox potential of the

electrocatalyst, with the order of the substrate determined based on the amount added into solution, given by Equation 1.3, where [cat] is the concentration of the catalyst, [Sub] the concentration of the substrate, and y the order of the substrate. It should be noted that this type of analysis could only be conducted if the electrocatalytic process being investigated is the major/dominant process occurring at the CV timescale. The effectiveness of the catalyst can then be determined by calculating the rate constant for catalysis, k_{cat}. In the event that the electrocatalytic process being investigated is not the dominant mechanism or the kinetically fastest process, a CV titration can also be done to observe the growth of any secondary processes that arise from excess substrate.

$$I_{cat} = n_{cat}FA[cat](Dk_{cat}[Sub]^{y})^{\frac{1}{2}} \quad (1.3)$$

Weak-Acid Model

The reduction of protons at Pt surfaces has been the subject of extensive study in electrochemistry. Of great interest is the shift of the reduction potential with the pH of the solution and the acid dissociation constant of the acid used (pK_a). A linear relationship was found to exist between the pH/pK_a and the corresponding shift in the $E_{1/2}$ relative to the thermodynamic value regardless of the solvent investigated (Equation 1.4). In the event that the pH > pK_a, the term in Equation 1.4 would vary with pH. When the pK_a and the resulting $E_{1/2}$ are determined for each ANH at a Pt electrode in the solution mixture used, our results can be compared to the 'weak acid' model, governed by Equation 1.4.[51, 63, 66]

$$E_{1/2}(\text{p}K_a) = E^{\circ}(\text{H}^{+}/\text{H}_2, \text{Pt vs. FcH}^{0/+}) - 0.059\text{p}K_a(\text{solvent}) - E_{solvent} \quad (1.4)$$

The E_{solvent} term factors in any overpotential associated with the dissolution of H_2 from the Pt surface into the solvent mixture used [E_{H_2O} = 0 V, $E_{CH_3CN/H_2O} \neq 0$ V].[66] This work

uses this relation to determine if the ANH systems investigated are governed by a 'weak-acid' model on the CV timescale.

Experimental Setup

CV studies conducted in this work used a three-electrode setup, where the applied potential at a working electrode with a defined geometry and area is with respect to a quasi-reference electrode (Ag/AgCl) in contact with the solution through a frit, and a counter electrode to help drive the current to maintain the applied potential. The experimental setups used for ambient electrochemical methods and air-sensitive electrochemical methods are shown in Figure 1.10.

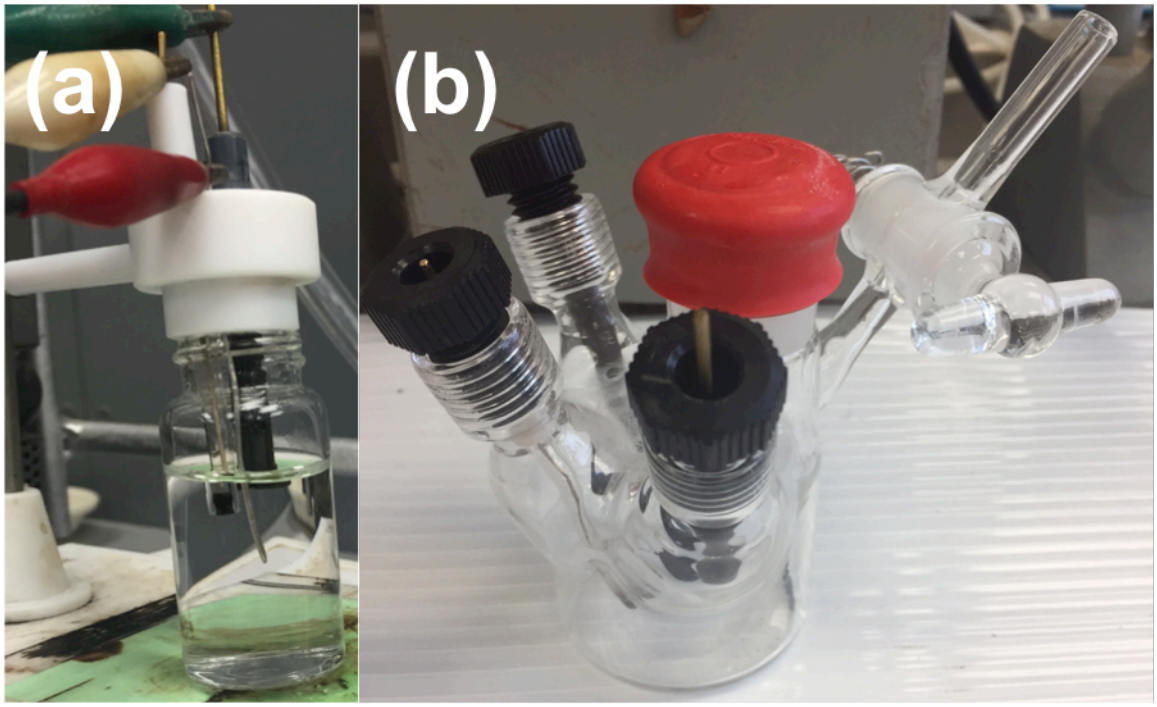

Figure 1.10. (a) Set-up used for air-stable compounds. A Teflon holder is used to place the working disc electrode (black electrode), reference electrode (fritted tube) and counter electrode (Pt wire) in solution. (b) Set-up used for air-sensitive compounds. The electrodes are screwed-into place, creating an air-tight seal with an O-ring, and a septum placed on the large port to allow for sparging of the solution. Ar/CO_2 is bubbled into solution prior to CV experiments.

1.5.2 Bulk Electrolysis

Theory

While CV experiments provide preliminary information about the types of processes occurring electrochemically at the electrode surface, none of the resulting intermediates, number of electrons, or products of a catalytic process can be determined due to the relatively small proportion of substrate being oxidized/reduced on the CV timescale. As such, a larger-scale electrochemical process is required, allowing quantification and characterization of the reduced/oxidized products using other analytical techniques. Bulk electrolysis can be used, where a high-surface area electrode is used as the working electrode, and the counter electrode used is kept inside a compartment separated by a frit to prevent any product crossover (Figure 1.11). These can be conducted either at constant potential (potentiostatic) allowing control over the processes occurring at the electrode surface, or constant current (amperostatic), enabling control over the rate of the redox reaction.[63]

After identification and quantification of the products arising from bulk electrolysis, the current efficiency, or Faradaic efficiency (%FE), can be determined for each process, where the charge associated with product formation is compared to the total charge passed (Equation 1.5). If all products are accounted for and no Ohmic losses occur, the total %FE should be 100%. To determine the charge associated with product formation, Faraday's law of electrolysis can be used (Equation 1.6), where n is the number of moles of product, Z the number of electrons associated with the product formation, Q the charge, and F Faraday's constant.[63]

$$\%FE_{Prod} = \frac{Q_{Prod}}{Q_{tot}} \quad (1.5)$$

$$n = \frac{Q}{ZF} \quad (1.6)$$

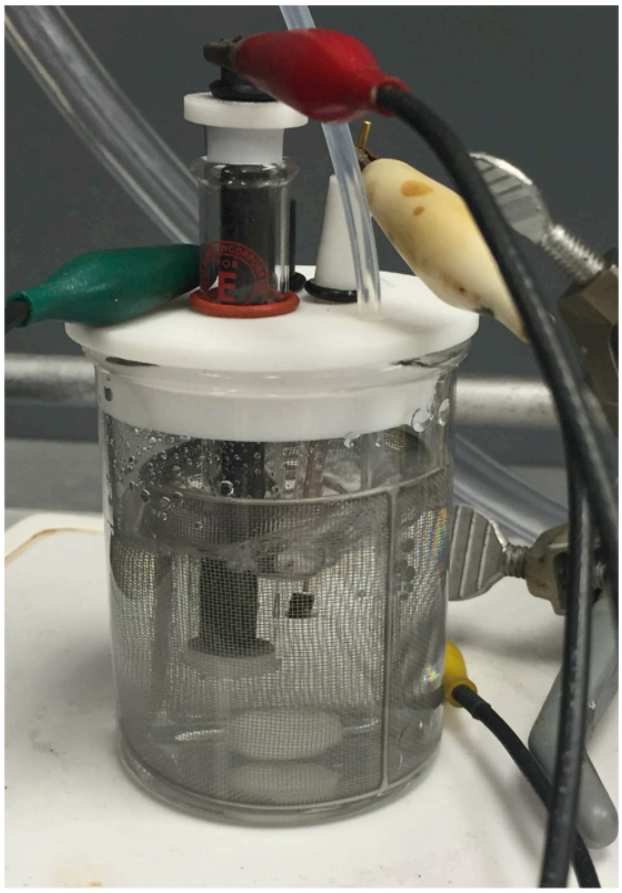

Figure 1.11. Bulk Electrolysis setup used in this work. Ar/CO_2 is bubbled into solution, with the solution stirred in the working electrode compartment (Pt mesh electrode shown) where the reference electrode (white electrode) is placed. The counter electrode (graphite rod) is placed in a separate glass-tube, connected to the working electrode solution through a frit to prevent product crossover.

1.6. Thesis Overview

Despite computational studies proposing that a DHP is capable of reducing CO_2 to methanol under electrochemically reducing conditions, there has been no experimental examination into the ability of DHP to facilitate electrochemical reduction of CO_2, nor has there been any evidence of DHP generation with conclusive generation of formic acid or methanol. As such, the work presented in this thesis investigates the ability of

benzannulated pyridines, and related DHP species towards CO_2 reduction to methanol and formic acid under electrochemically reducing conditions (Figure 1.12) at Pt and glassy carbon surfaces (GCE) in Chapter 2.[67] The electrochemical properties of these systems will be investigated as described in Section 1.5, with product characterization and quantification conducted using analytical techniques as described in Section 2.2, with the results therein put into the context of Section 1.4. In Chapter 3, the ability of ANH/DHPs to facilitate the electrochemical reduction of formic acid to methanol will be explored in Chapter 3 using the techniques described in Section 1.5 and Section 3.2; a process not yet attempted using ANHs, allowing mechanistic insight towards the reactivity of a key intermediate in CO_2 reduction to methanol, as proposed in Section 1.4. In addition, the ability to electrochemically generate a DHP species under CO_2 reducing conditions in ANH-containing solutions with simultaneous methanol generation is detailed in Chapter 3, utilizing techniques described in Section 1.5 and Section 3.2. These results should provide key insights as to the role ANHs and DHPs play in the CO_2 reduction mechanism under electrochemically reducing conditions, as well as elucidate the rate-limiting step of ANH-based electrochemical CO_2 reduction to methanol. Lastly, Chapter 4 will summarize key findings of this thesis and offer an outlook as to the direction of further progress.

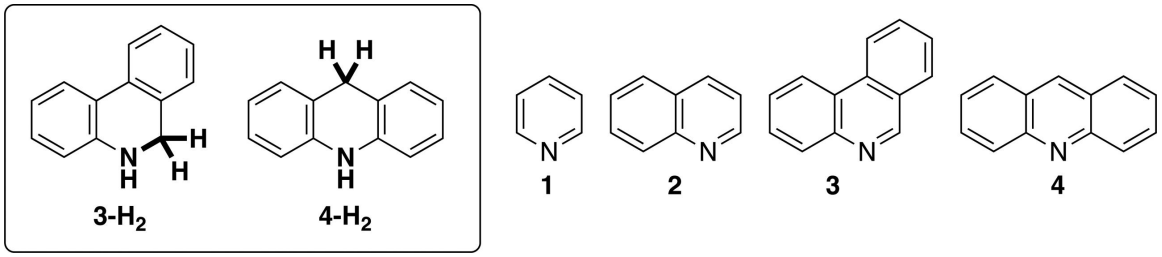

Figure 1.12. Benzannulated pyridines and dihydropyridines investigated as additives for electrochemical CO_2 and HCOOH reduction in this work. Taken from Reference [67]. Copyright 2017 American Chemical Society.

Chapter 2: Electrochemical Reduction of Carbon Dioxide to Methanol in the Presence of Benzannulated Dihydropyridine Additives (Adapted from Reference [67])

2.1 Introduction.

Despite their prominence in computed mechanisms, the ability of isolated DHPs to facilitate methanol production in a fashion similar to that of parent ANHs has not been tested to date. We hypothesized that if DHPs are to be competent intermediates, they should exhibit activities comparable to those of their parent ANHs. Compared with pyridine (**1**) and quinoline (**2**), phenanthridine (**3**) and acridine (**4**) offer the ability to form more easily isolable (less reactive) dihydro-species **3-H$_2$** and **4-H$_2$** (Figure 2.1). In addition, as **3-H$_2$** and **4-H$_2$** exhibit *ortho* and *para* positions for DHP formation, the relative activity of 1,2- and 1,4-DHPs towards CO_2 reduction can be determined. Computational studies by Carter *et al.* investigating electrochemical DHP formation predicted that while the 1,4-DHP is more thermodynamically stable, the 1,2-DHP is the active species for CO_2 reduction based on the steric interactions at p-GaP surfaces.[54b, 57-58] Scanning-tunneling microscopy (STM) of **1** adsorbed on p-GaP confirms this hypothesis, where both the 1,2-DHP and the 1,4-DHP had the ability to form on the surface.[68]

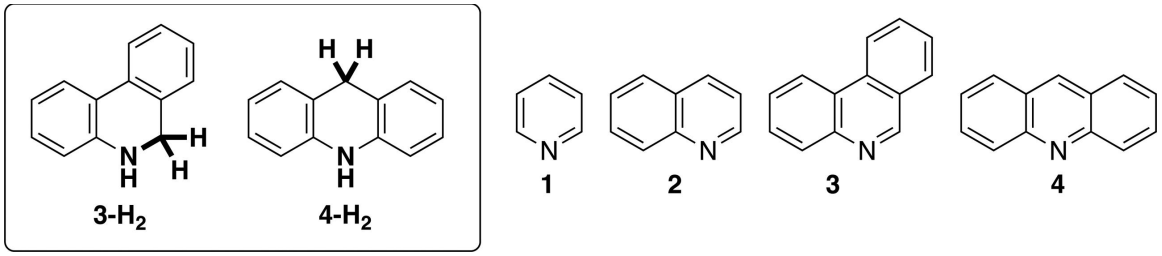

Figure 2.1. Benzannulated pyridines and dihydropyridines investigated as additives for electrochemical CO_2 reduction in this work. Taken from Reference [67]. Copyright 2017 American Chemical Society.

Furthermore, the hydricity, or ability to donate a hydride to a substrate, of the DHPs **3-H$_2$** and **4-H$_2$** also differ. The calculated hydride nucleophilicity (N) of **3-H$_2$** (N ~ 8.1) is found to be comparable to that of Hantzsch's ester (N = 9.00), while the hydride nucleophilicity of the *N*-methyl derivative of **4-H$_2$**, 10-methyl-9,10-dihydroacridine, was experimentally determined to be lower (N ~ 5.54).[55b] As a comparison, the hydride nucleophilicity of 1,2-**1-H$_2$** is predicted to be around 11.4, indicating that **1-H$_2$** is the strongest proposed hydride donor used in this work towards CO_2 reduction. Quinoline (**2**) was predicted to also exhibit CO_2-reducing characteristics based on the work by Keith (see Chapter 1, Figure 1.8), and was also investigated in this work to observe the effect pyridine benzannulation has on CO_2 reduction efficiency and product distribution. The hydride nucleophilicity of *ortho*-1,2-dihydroquinoline (**2-H$_2$**) is reasoned to be intermediate between that of *ortho*-1,2-dihydropyridine (**1-H$_2$**) and 1,2-dihydrophenanthridine (**3-H$_2$**). This is on the basis that the remaining olefinic subunit in the partially hydrogenated *ortho*-**2-H$_2$** retains conjugation with an intact aromatic benzo ring and is therefore stabilized with respect to the diene fragment of **1-H$_2$**.

The reactivity of the isolated C=N bond toward hydrogenation in **3** is highlighted by the fact that the "imine-bridged, biphenyl" resonance contributor dominates the ground-state structure of **3**, in accordance with Clar's postulate.[69] **3-H$_2$** has been used in the transfer hydrogenation of C=O bonds in α-ketoesters under acidic conditions, indicating that it might also participate in the reduction of CO_2.[70] Combined with the calculated or experimental hydride nucleophilicities of the rest of the series, the order of decreasing hydride donor ability can be estimated as **1-H$_2$** > **2-H$_2$** > **3-H$_2$** > **4-H$_2$**. Thus, isolated DHPs [1,2-dihydrophenanthridine (**3-H$_2$**) and 9,10-dihydroacridine (**4-H$_2$**)] were

screened as additives in electrochemical CO_2 reduction at both Pt and glassy carbon electrodes (GCEs), with comparison to the parent ANHs **1**-**4**.

2.2 Experimental

2.2.1 Materials

All chemicals and reagents were used as received unless otherwise noted. Solutions for electrochemical experiments were made using MilliQ water (18.2 Ω·cm) and HPLC grade CH_3CN, with $LiClO_4$ (98%, Sigma) as the supporting electrolyte. Pyridine (**1**, 98%, Fisher Scientific), quinoline (**2**, 99%, Acros Organic), phenanthridine (**3**, 98%, Acros Organic) and acridine (**4**, 98%, Alfa Aesar) were used as received in 1 to 10 mM concentrations in non-aqueous (CH_3CN), and mixed solutions (60% (v:v) H_2O /CH_3CN). Perchloric acid ($HClO_4$) was used as received in 3 to 1000 mM concentrations. The pH of the solutions investigated under Ar was adjusted using $HClO_4$ to the pH observed for identically constituted solutions under CO_2 atmosphere. $LiAlH_4$ (Sigma) and diethyl ether were used as received for synthesis of DHP-species **3-H$_2$** and **4-H$_2$**. Tetrahydrofuran (THF) was dried using sodium wire (benzophenone indicator) prior to use.

2.2.2 Synthetic Methods

Synthesis of 1,2-Dihydrophenanthridine (3-H$_2$)

The synthesis of 1,2-dihydrophenanthridine (**3-H$_2$**) was adapted from a previous report.[71] In brief, a nitrogen-purged solution of $LiAlH_4$ (0.508 g, 13.4 mmol) in THF (7 mL) was added drop-wise to a solution of **3** (0.400 g, 2.22 mmol) in THF (10 mL) under nitrogen, and the resulting green mixture stirred at room temperature for 16 hours. The solution was then cooled to 0 °C and 7 mL of argon-purged water was added. The mixture was

kept at this temperature for one hour then warmed to room temperature, at which point any solid was filtered off and the filtrate dried to give a yellow white powder. Yield = 0.350 g (87%, 95% pure, Figure 2.2). ^{1}H NMR (300 MHz, CD_3CN, 22 °C): 7.50 (t, 2H, J_{HH} = 7.5 Hz), 7.11 (t, 1H, J_{HH} = 7.5 Hz), 7.03 (overlapped doublets, 1H, J_{HH} = 7.5 Hz, 1.5 Hz, Ar C*H*), 6.96 (d, 1H, J_{HH} = 7.5 Hz, Ar C*H*), 6.89 (m 1H, Ar C*H*), 6.58 (m, 1H, Ar C*H*), 6.51 (d, 1H, J_{HH} = 7.6 Hz, Ar C*H*), 4.48 (broad, 1H, N*H*), 4.12 ppm (singlet, 2H, CH_2).

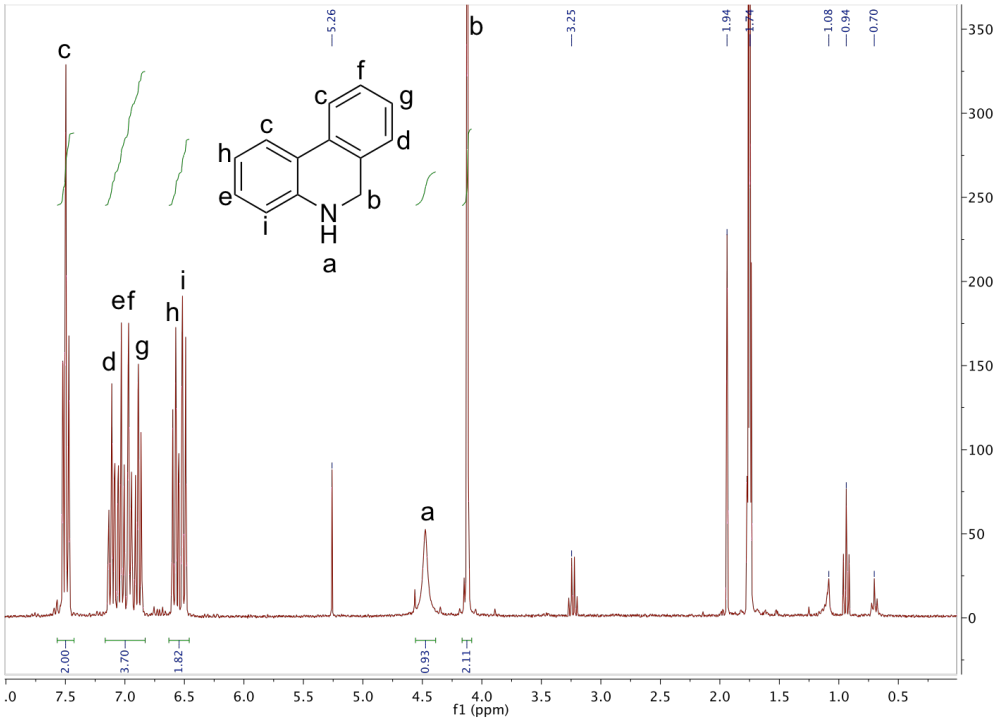

Figure 2.2. ^{1}H NMR spectrum (CD_3CN) of **3-H$_2$**. Residual solvent peaks are indicated. Taken from Reference [67]. Copyright 2017 American Chemical Society.

Synthesis of 9,10-Dihydroacridine (4-H$_2$)

The synthesis of 9,10-dihydroacridine (**4-H$_2$**) was conducted using the same procedure as for **3-H$_2$**. A nitrogen-purged solution of $LiAlH_4$ (0.384 g, 10.1 mmol) in THF (10 mL) was added drop-wise to a solution of **4** (0.400 g, 2.23 mmol) in THF (10 mL) under nitrogen, and the resulting green-grey solution stirred at room temperature for

16 h. At this point, 6 mL of argon-purged water was added drop-wise to the solution at 0 °C, and the mixture kept at this temperature for 1 h prior to warming to room temperature. Argon-purged diethyl ether (75 mL) was used to extract the organic product and dried, providing a yellow-white powder. Yield = 0.176 g (44% isolated, 100% NMR conversion, see Figure 2.3). ^{1}H NMR (300 MHz, CD_3CN, 22 °C): 7.06 (t overlapping, 4 H, J_{HH} = 7.8 Hz), 7.04 (broad singlet overlapping, 1 H), 6.81 (t, 2 H, J_{HH} = 7.5 Hz), 6.74 (d, 2H, J_{HH} = 7.5 Hz), 4.00 ppm (singlet, 2H).

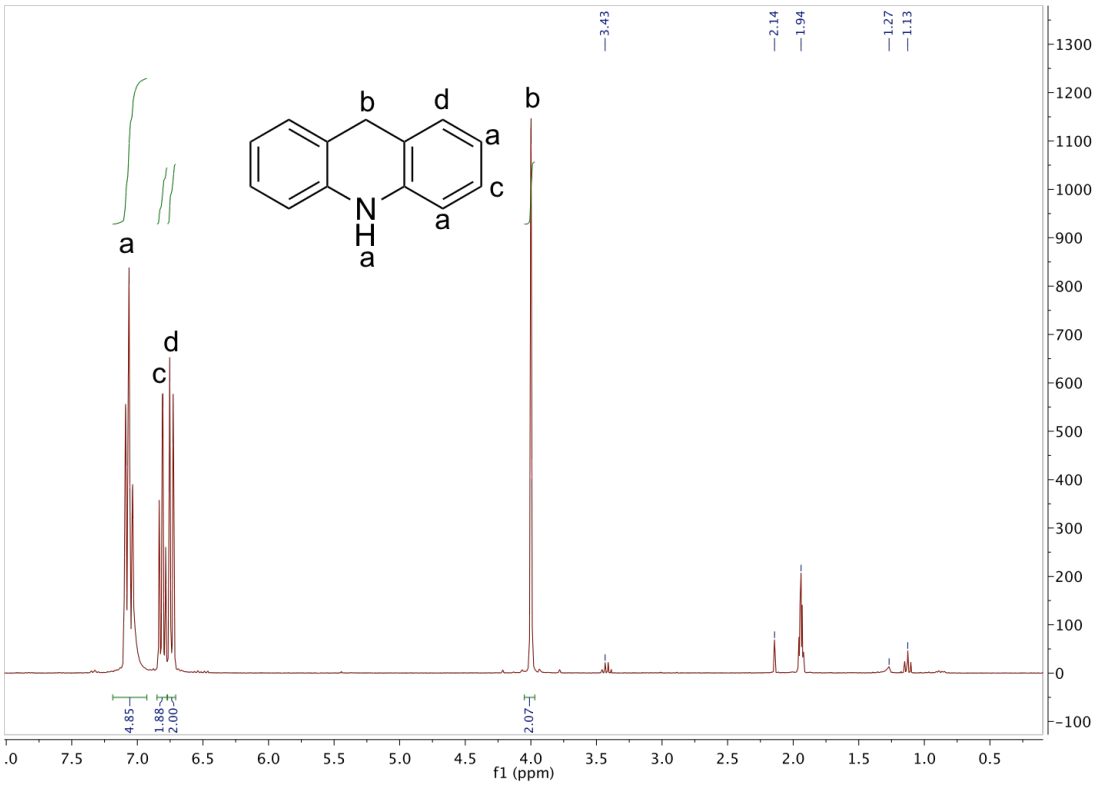

Figure 2.3. ^{1}H NMR spectrum (CD_3CN) of **4-H$_2$**. Residual solvent peaks are indicated. Taken from Reference [67]. Copyright 2017 American Chemical Society.

2.2.3 CV Experiments

CV experiments were performed on a CHI 760c bipotentiostat at scan rates of 50-800 mV s^{-1} using freshly polished (with 0.05 μm alumina paste) Pt or glassy carbon (GCE) disc working electrodes, a Pt wire counter electrode, and a Ag/AgCl aqueous

quasi-reference electrode. Ferrocene (FcH) was added as an internal standard to each solution upon completion of all cyclic voltammetry experiments, allowing potentials to be referenced to the ferrocene/ferrocenium ($FcH^{0/+}$) redox couple. To account for the use of a mixed solvent system, any shift of the $FcH^{0/+}$ redox couple due to the CH_3CN/H_2O ratio employed relative to SCE was considered, as previously described.[72] In the 60% (v:v) H_2O/CH_3CN solution used, the shift of the $FcH^{0/+}$ redox couple placed the redox potential at +0.24 V vs. SCE. For the electrochemical characterization of **3-H$_2$** and **4-H$_2$**, an air-tight electrochemical cell was employed to prevent ambient oxidation of the DHPs, with a graphite rod counter electrode and a Ag/AgCl quasi-reference electrode.

2.2.4 Bulk Electrolysis Experiments

Bulk electrolyses were conducted using a Pt mesh electrode (125 cm^2) and a reticulated vitreous carbon (RVC) electrode (~ 700 cm^2) with CO_2 constantly bubbled into the solution (1 atm) and the solution stirred, with a Ag/AgCl quasi-reference electrode (total volume of 90 mL). A graphite rod was used as the counter electrode to prevent reoxidation of any CO_2-reduced species produced at the working electrode, and was stored in a glass-fritted tube.[73] A potential of -0.50 V vs. Ag/AgCl (-0.75 V vs. $FcH^{0/+}$) at Pt mesh, and –0.95 V versus Ag/AgCl (-1.20 V vs. $FcH^{0/+}$) at a RVC electrode, was applied for all ANHs investigated for approximately 10 000 s, resulting in 15-30 C of charge being passed in each experiment.

2.2.5 Product Analysis

NMR Characterization Protocol

NMR Technique for Synthetic Products

For analyses of isolated, synthetic products, NMR experiments were performed on a 300 MHz NMR spectrometer (Bruker) on 5-30 mg of the product in 0.6 mL $CDCl_3$ or CD_3CN.

NMR Technique for Electrolyzed Solutions.

Due to the relatively low concentrations of carbon-containing species produced, ^1H NMR spectroscopic analyses were performed on a 500 MHz spectrometer (Bruker) using aliquots (0.6 mL) taken directly from the electrolyzed solution and mixed with 0.06 mL D_2O, using a pulse-sequence suppression of the water (~4.7 ppm) and acetonitrile (~2.4 ppm) peaks, with a delay time of 3.0 s, a 12 μs pulse width, and 0.82 s acquisition time. Standard solutions of methanol (~3.4 ppm) and formic acid (8.5 ppm) were used to determine the peak positions under these conditions, with a large suppression in the integrals of the methanol peak relative to the formic acid peak observed under the NMR experimental conditions employed (see Appendix, Figure A1). As such, methanol quantification was not conducted using ^1H NMR. ANHs **1**-**4** also exhibit resonances that overlap with formic acid, with the formic acid peak occurring in the range of 8.2-8.7 ppm, precluding accurate identification and quantification by ^1H NMR spectroscopy.

GC-FID Characterization Protocol

Methanol quantification was conducted using Gas Chromatography with Flame Ionization Detection (GC-FID). Before GC analysis, the electrolyzed solution was desalted using a bulb-to-bulb transfer to allow injection into the GC. A 1.0 μL aliquot of

the desalted solution in a 50/50 split was injected into the GC, with the headspace heated to 250 °C and a CP-Sil 8 CB Chrompack column heated at 120 °C for 1 min, raised to 150 °C over 2 min, and maintained for another 4 min, at a flow rate of 1 mL/min. Methanol content was determined by analyzing the peak produced at a retention time of 2.92 min in the chromatogram using CompassCDS 3.0 Software (Bruker) (solvent peak arises at 3.0 min). A linear baseline correction was used for all GC-FID peak integrations conducted in this work, with the peak area determined for each sample to be in the range of 0.2-4.0 μV*min, and with an error of 0.1 μV*min (corresponding to integrating the noise in the blank samples at 2.92 min, 4-50% of the corresponding peak area in the bulk electrolysis samples) from the integration method used. To ensure no residual methanol arose from the bulb-to-bulb transfer or the bulk electrolysis procedure, bulk electrolysis of control solutions with no ANH/DHP added were subjected to the bulb-to-bulb transfer protocol and run using the same GC-FID method, with no discernable signal registered (Figure 2.16).

GC-MS Characterization Protocol

Prior to GC analysis, the electrolyzed solution was desalted using a bulb-to-bulb transfer to allow injection into the GC. A 1.0 μL aliquot of the desalted solution in a 50/50 split was injected into the GC, with the headspace heated to 250 °C and a CP-Sil 8 CB Chrompack column heated at 120 °C for one minute, raised to 150 °C over two minutes, and maintained for another four minutes, at a flow rate of 1.0 mL/min. The M/Z region investigated was +30-34 Da, allowing observation of the methanol content in each sample.

LC-MS Characterization Protocol

Identification and quantification of formate content was conducted using Liquid Chromatograph-Mass Spectrometry (LC-MS). In brief, a 20.0 μL aliquot of the electrolyzed solution, without any pretreatment, was injected into the LC and passed through an Aminex HPX-87H column at 40 °C at 0.5 mL/min. Analysis of the formate content was conducted through analysis of the signal at M/Z = -45 Da on a QTrap LC-MS. Methanol detection could not be conducted due to the insensitivity of our LC-MS method to the low concentrations of methanol generated by bulk electrolysis.

Determination of the pK_a of 1-4

The determination of the pK_a for the conjugate acid of **1-4** was determined using a weak base-strong acid titration, with $HClO_4$ acting as the strong acid. The acid solution, prepared in a 60% (v:v) H_2O/CH_3CN solution, was added to 10 mM **1-4** in 60% (v:v) H_2O/CH_3CN in 0.1 mL increments, with the pH of the solution determined using an Accumet benchtop pH meter. Once the equivalence point was determined, the pK_a was taken as the pH value where half the acid needed for the equivalence point was added.

2.3 Results.

2.3.1 CV Results

CVs of ANHs **1**−**4** at Pt in the absence of CO_2 but under similar acidic conditions (i.e., at the pH observed in saturated CO_2 solutions, resulting from the formation of a buffered H_2CO_3/HCO_3^-) show a quasi-reversible reduction at ca. −0.7 V vs. $FcH^{0/+}$

(Figure 2.4). Introduction of CO_2 to the ANH solution results in an increase in the current observed on the CV timescale for **1**−**3** (Figure 2.4), though only for **1** and **2** is the enhancement above the sum of the background currents ($J_{\mathbf{ANH/[ANH\text{-}H]^+}} + J_{CO2}$) at the scan rates employed (Table 2.1; compare columns 3 and 5). In aqueous solution, increased cathodic current for solutions of **1** in the presence of CO_2 was detected only at scan rates less than 10 mV s^{-1}.[43a] For **3**, the enhancement is not significant compared to the sum of the background currents ($J_{\mathbf{3/[3\text{-}H]^+}} + J_{CO2}$). At the scan rates employed (100 mV s^{-1}), this current enhancement is likely a result of the presence of dissolved CO_2/H_2CO_3 in solution, augmenting the available protons that can undergo proton reduction, increasing the current observed.[48] In the case of **4**, no current enhancement was observed, but instead a 50 mV anodic shift in the redox potential was observed. This could again result from the presence of a H_2CO_3/HCO_3^- buffer, helping stabilize the reduction process **4** undergoes.

In a recent study, Rybchenko *et al.* confirmed that, in addition to methanol production, hydrogen evolution is the dominant electrochemical reaction in **1**-containing aqueous electrolyte solution at Pt, even under high CO_2 pressure.[47] Methanol production with %FE of up to 10% for the first 5−10 C cm^{-2} can be reproducibly detected but only after one hour of electrolysis. As a result, only a small to negligible current enhancement is expected on the CV time scale (milliseconds to seconds) for CO_2 reduction in the presence of ANH additives chemically similar to **1**.

Table 2.1. Peak Current Values for the ANH/[ANH-H]$^+$ Couple under Ar and CO_2.

ANH	$J_{ANH/[ANH-H]+}$ (mA cm^{-2})	$J_{CO2+ANH}$ (mA cm^{-2})	J_{CO2} (mA cm^{-2})	$J_{ANH/[ANH-H]+} + J_{CO2}$ (mA cm^{-2})
1	-0.48	-1.1	-0.20	-0.68
2	-0.45	-0.76	-0.20	-0.65
3	-0.20	-0.43	-0.20	-0.40
4	-1.0	-1.0	-0.20	-1.2

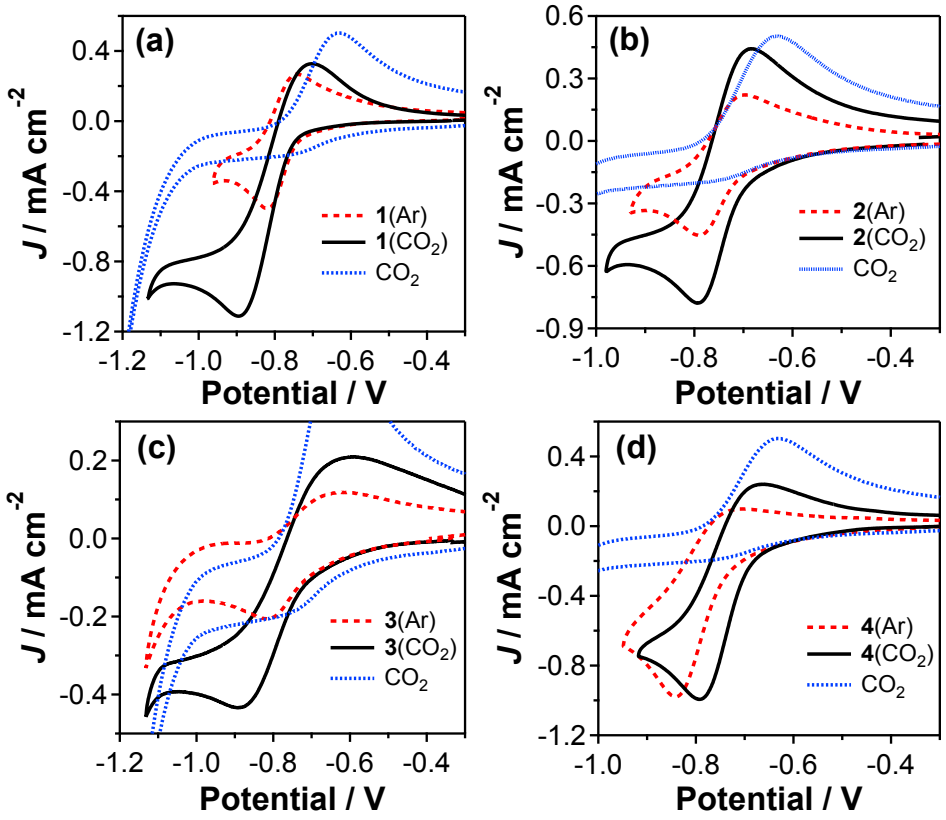

Figure 2.4. CVs. 1 atm CO_2 (black); under Ar in acid (red); and CO_2 alone (1 atm, blue) for 10 mM of (a) **1**, pH = 5.5; (b) **2**, pH = 5.3; (c) **3**, pH = 5.2; (d) **4**, pH = 5.7. ν = 100 mV/s; 0.1 M $LiClO_4$, Pt disc; Potential vs. $FcH^{0/+}$. Taken from Reference [67]. Copyright 2017 American Chemical Society.

To determine if the process observed for the ANHs was due to a 'weak acid' mechanism at the CV timescale, the reduction potential, $E_{1/2}$, was compared to the experimentally determined pK_a of the ANHs. Previous studies examining the dependence of the reduction potential observed on the derivative of pyridine used have observed a linear relationship between $E_{1/2}$ and the pK_a of the pyridine derivative used, with a slope

of -60 mV/[unit pH], and an intercept at the thermodynamic potential for proton reduction.[51] Similarly, a linear correlation is observed between $E_{1/2}$ and ANH pK_a (Figure 2.5a), with a slope of −0.054 V/[unit pH], indicating the 'weak acid' relationship observed in water is preserved in the mixed CH_3CN/H_2O solvent used. As a mixed solvent system was used, and the potentials referenced to $FcH^{0/+}$, the intercept is shifted from the value determined vs. SCE due to the overpotential required to dissolve H_2 from the Pt surface into the mixed water/acetonitrile mixture ($E_{solvent}$).[66] For accurate comparison with reduction potentials of **1/[1-H]**$^+$ taken from the literature,[51] the dependence of the ferrocene redox couple on water content in acetonitrile had to be taken into account, allowing an accurate comparison of the predicted redox potentials in water to the experimentally obtained values in the CH_3CN/H_2O mixture, shown in Table 2.2 referenced to SCE.[72] This was conducted to ensure no alteration in the reduction process at the CV timescale was occurring. The $E_{1/2}$ values observed for ANHs **1**, **2**, and **4** in Table 2.2 all agree with the values predicted using pK_a's in pure water (and in the case of **1**, with the reported experimental values); while **3** shows a large change in acidity moving from water to the solvent mixture used, and accordingly the $E_{1/2}$ observed for **3** is more anodic than predicted using the pK_a of **3** in pure water. The change in acidity could be a result of preferential solvation due to the poor solubility of **3** in water, leading to a low formation of the conjugate acid of **3**, lowering its apparent pK_a more than that observed for **1**, **2** and **4**.[74]

Table 2.2. Experimental (CV) and predicted values for the reduction potential of ANHs at a Pt electrode in aqueous solution. Copyright 2017 American Chemical Society.

Compound	pK_a(H_2O)	pK_a(CH_3CN/H_2O)	$E_{1/2}$[a](H_2O) / V	$E_{1/2}$[a] (CH_3CN/H_2O) / V
1	5.15	4.5	-0.56	-0.56
2	4.92	4.0	-0.54	-0.53
3	5.58	3.6	-0.58	-0.49
4	5.58	4.4	-0.58	-0.55

[a] Referenced to SCE.

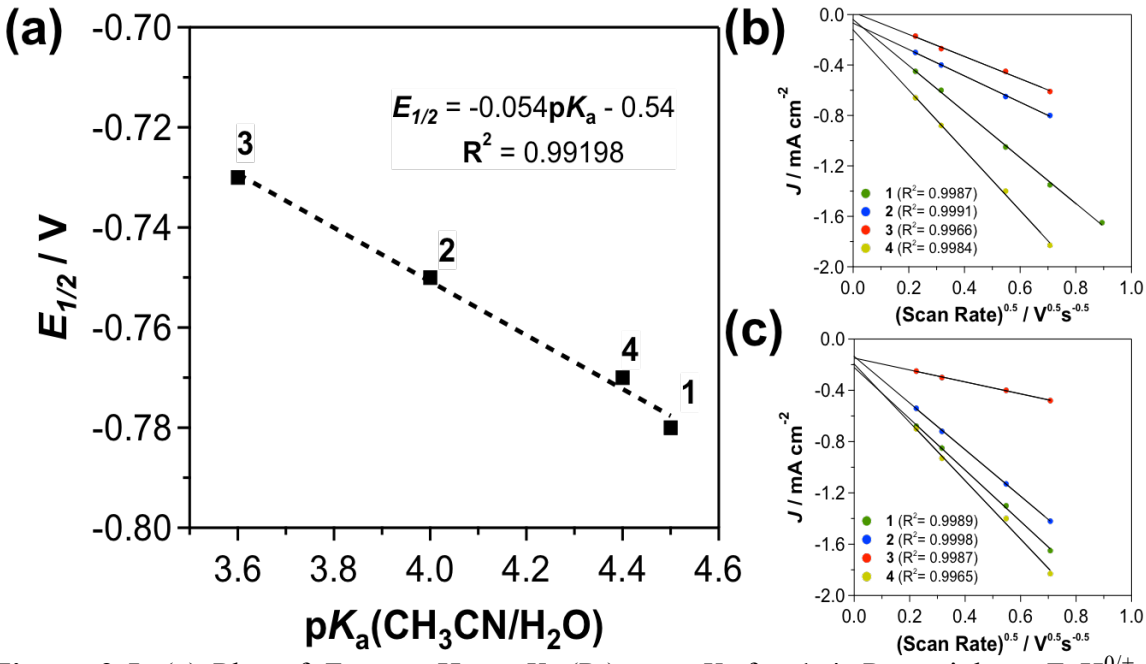

Figure 2.5. (a) Plot of $E_{1/2}$ at pH = pK_a (Pt) vs. pK_a for **1-4**. Potential vs. $FcH^{0/+}$. Randles-Sevcik plots for the ANHs **1-4** under (b) Ar (same pH as under CO_2) and (c) CO_2 (1 atm). 0.1 M $LiClO_4$, Pt disc electrode. Adapted from Reference [67]. Copyright 2017 American Chemical Society.

To determine if the reduction event in Figure 2.4 was a result of a solution-based or surface-based process, the scan rate dependence was determined based on Randles-Sevcik plots, shown in Figure 2.5 (b) and (c) for Pt surfaces under Ar and CO_2. In both cases, the reduction process was determined to be solution-based, with the current showing a square-root dependence on the scan rate. Furthermore, the reduction process under CO_2 showed no peak current saturation with the scan rate, indicating that it is

unlikely that an electrocatalytic event involving the ANH is occurring at these timescales or is a minor contributor to the current response (see Chapter 1, Section 1.5.1).[64b] Previous studies involving **1** have also shown diffusion control under acidic and CO_2 conditions, with the reduction couple associated with the $1e^-$ reduction corresponding to the ANH/$[ANH\text{-}H]^+$ couple, resulting in the ANH and a surface adsorbed hydride H_{ads}.[43, 51]

CVs were next conducted using a GCE, which is a less reactive electrode material than Pt in regards to proton reduction of weak acids and therefore H_{ads} formation.[46, 75] CVs carried out in acid and under CO_2 show a cathodic shift in E_{peak} for all ANHs (~ -1.5 V under CO_2), but not by a commensurate amount as would be expected from a weak acid reduction mechanism (Figure 2.6). Furthermore, **4** deposited onto the electrode upon reduction in acid. ^{1}H NMR of the material deposited confirms the identity of acridinium as the main deposition species, with no polymerized species observed (see Appendix, Figure A3). Pyridinium has been reported to form an insulating film after one reductive scan on GCE in pure CH_3CN.[64a] Only **4** was observed to form a noticeable film upon reduction under CO_2 in this work. Thus, the importance of a 'weak-acid' mechanism at the GCE surface has been superceded by other electrochemical mechanisms, such as surface interactions (deposition) or π-based reduction.[46, 75]

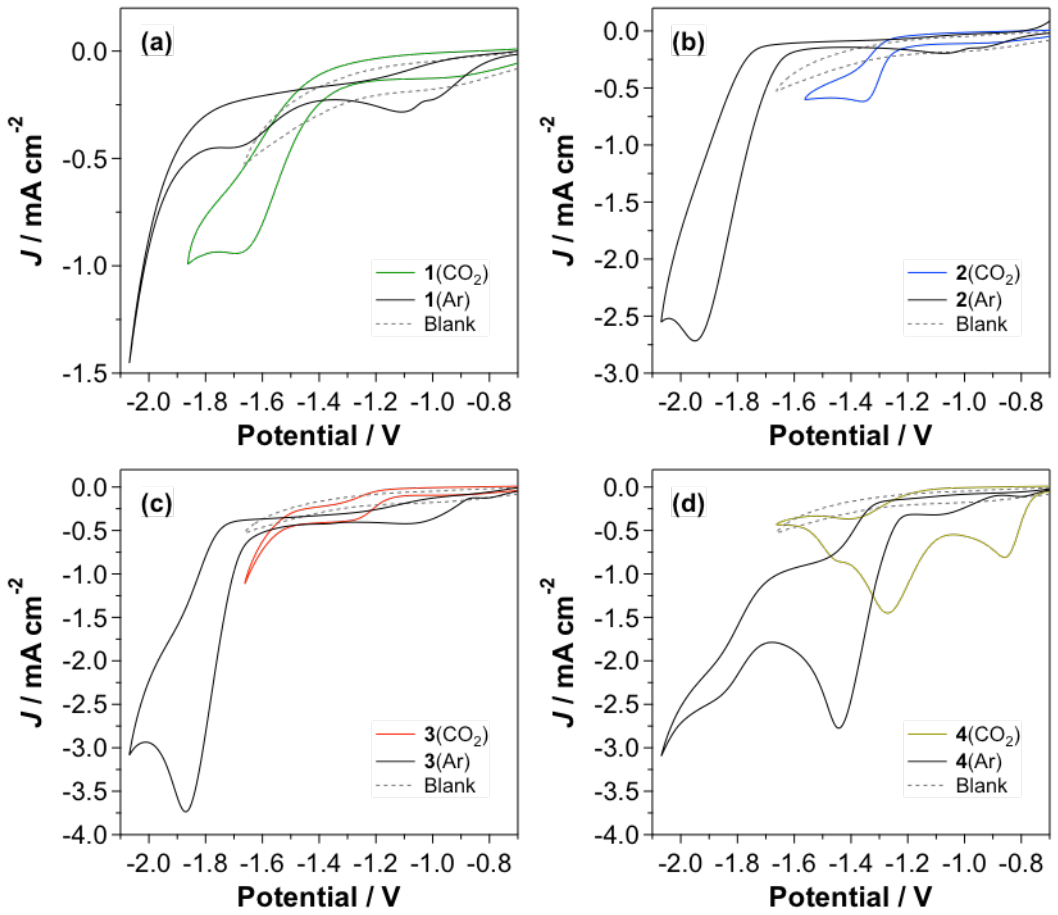

Figure 2.6. CVs of 10 mM (a) **1**, (b) **2**, (c) **3** and (d) **4** in 40% v/v CH_3CN/H_2O under acidic conditions (pH = 5.5, 5.3, 5.2, 5.7 respectively) (black) and CO_2 using a GC disk electrode, 0.1 M $LiClO_4$. Scan rate 100 mV/s. All potentials referenced to $FcH^{0/+}$. Film deposition observed for **4** after 1 CV scan under CO_2. Taken from Reference [67]. Copyright 2017 American Chemical Society.

To probe the influence of water on the CO_2 reduction process[43b, 55b, 76] while simultaneously increasing the amount of absorbed CO_2 gas in solution, dry CH_3CN was used as the electrolyte solvent, with 0.5 equivalents of $HClO_4$ added to the solution to provide an appropriately acidic environment. As no water was present in the solvent, the pH of the solution could not be determined. However, the addition of 0.5 equivalents of strong acid should result in a 1:1 mixture of ANH:$[ANH\text{-}H]^+$, creating an acidic environment similar to that formed under CO_2 in purely aqueous conditions (~4:1 ANH:$[ANH\text{-}H]^+$). CVs of **1-4** under these conditions are shown in Figure 2.7, where no

enhancement in the current was observed under CO_2 atmosphere. Instead, a decrease in the reduction peak current and a cathodic shift in E_{peak} is observed for **1**-**4**. Acridine (**4**) also exhibited an irreversible deposition process under these conditions. Bulk electrolyses did not yield observable CO_2 reduction products ($E_{applied}$ = -0.9 V vs. $FcH^{0/+}$) or DHP formation, indicating that proton reduction and deposition processes dominate the reduction current at the Pt electrode surface in the absence of water.[43b]

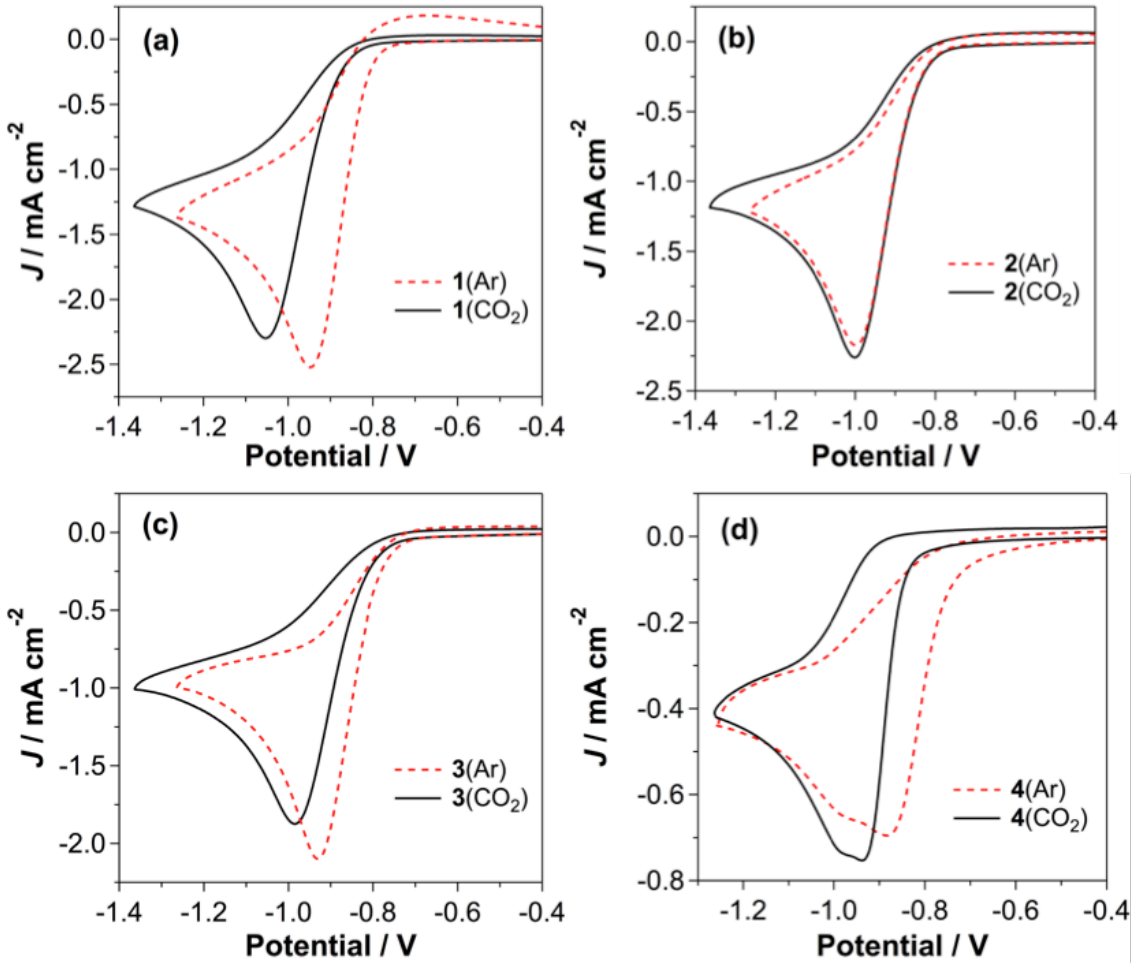

Figure 2.7. Cyclic voltammograms of 10 mM (a) **1**, (b) **2**, (c) **3** and (d) **4** in 5 mM $HClO_4$ 0.1 M $LiClO_4$ CH_3CN under Ar (red dashed) and CO_2 (black). Scan rate of 100 mV s^{-1}, Pt disk electrode. All potentials referenced vs. $FcH^{0/+}$. Taken from Reference [67]. Copyright 2017 American Chemical Society.

CVs of DHPs **3-H$_2$**/**4-H$_2$** in the absence of CO_2 show no reductive events in initial cathodic scans of neutral or acidic solutions at Pt or GCE (Figure 2.8). Cathodic current

can be observed after cycling through a $2e^-/ 2H^+$ electrochemical oxidation (0.3−0.5 V vs. $FcH^{0/+}$) (Figure 2.8), similar to other reported values for the oxidation of dihydrophenanthridine species.[77] To ensure proper assignment and to ensure that the oxidation process was not due to the presence of ANH, the CV of ANH oxidation under the same conditions was conducted, with no significant oxidation peak registered (see Appendix, Figure A4). This new reductive event is in the same $E_{1/2}$ range as the reduction of **3** in acidic conditions, and is thus accordingly assigned to the reduction of newly formed **[3-H]$^+$/[4-H]$^+$** in solution following oxidation of the DHP.[77]

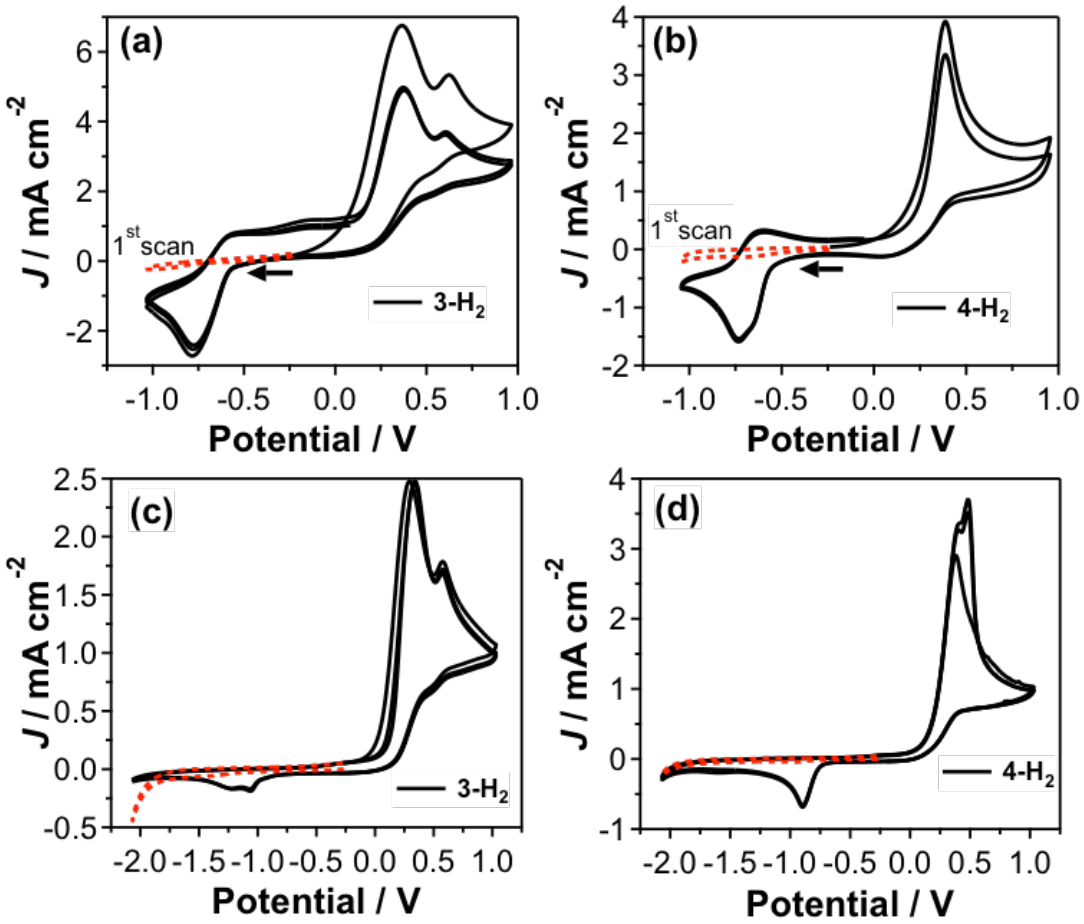

Figure 2.8. CVs. of 10 mM **3-H$_2$** and **4-H$_2$** under Ar at pH = 5.5 at (a,b) Pt and (c,d) GCE, with growth of a reduction wave after oxidation of the DHP-species. Scan rates of 100 mV/s; 0.1 M $LiClO_4$; all potentials referenced vs. $FcH^{0/+}$. Taken from Reference [67]. Copyright 2017 American Chemical Society.

Introduction of CO_2 at Pt electrodes results in the appearance of an irreversible reduction at −0.8 V vs. $FcH^{0/+}$ when the potential is initially swept from the open circuit potential for **3-H$_2$**, with a large current enhancement compared to the initial cathodic scan under acidic conditions (Ar) and for a CO_2 saturated solution without any **3-H$_2$** present (Figure 2.9), indicative of an additional electrochemical event.[48, 64b, 65] The current enhancement for **3-H$_2$** under CO_2 is 5-fold larger in magnitude with a 25% increase in the total current passed under CO_2 compared to its parent ANH **3**. No current enhancement above the background currents was observed for **4-H$_2$** under CO_2, similar to **4**. Thus, from the CV experiments, it appears that the 1,2- orientation of the DHP is more reactive towards CO_2 reduction than the 1,4- orientation, as predicted by Carter when investigating the ability of DHPs to reduce CO_2 at GaP electrodes.[54b, 57] At GCE surfaces, a cathodic shift in the $E_{1/2}$ was observed similar to the ANH-based solutions, with reduction peaks observed at -1.2 V vs. $FcH^{0/+}$ (Figure 2.9). No apparent current enhancement was observed, however, potentially due to a slower reduction mechanism at RVC surfaces. Thus, at the potentials applied in the bulk electrolysis reactions, DHPs **3-H$_2$/4-H$_2$** exhibit an appreciable current response by CV at the scan rates examined only in the presence of CO_2 and at Pt surfaces.

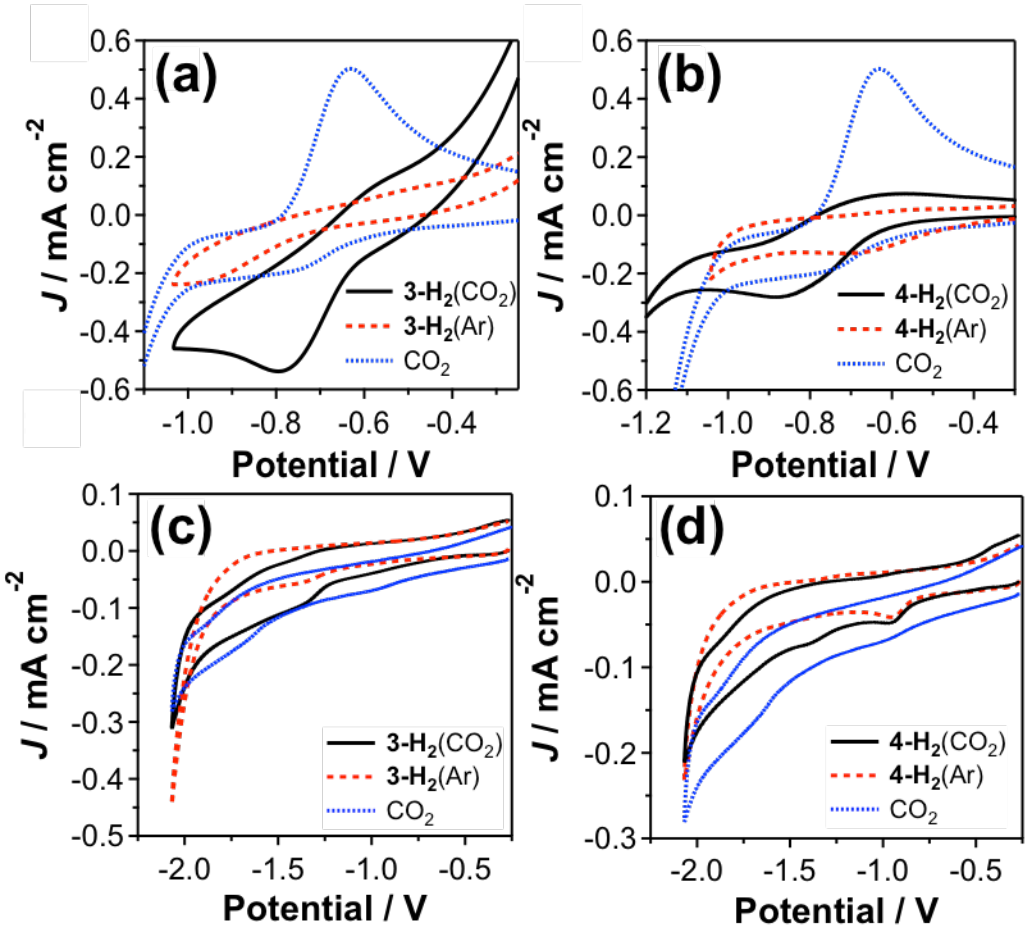

Figure 2.9. CV comparison of the first scans of CO_2 alone (blue dash), **3-H$_2$/4-H$_2$** under Ar (red), and under an atmosphere of CO_2 (black) at (a, b) Pt and (c, d) RVC electrodes. Scan rates of 100 mV/s; 0.1 M $LiClO_4$; Potential vs. $FcH^{0/+}$. Adapted from Reference [67]. Copyright 2017 American Chemical Society.

2.3.2 Bulk Electrolyses

Bulk electrolyses were conducted to quantify yields of liquid fuel candidates methanol and formate. Potentiostatic electrolyses were used to ensure selectivity of the reductive processes, with $E_{applied}$ and the charge passed chosen based on previously reported optimizations for **1**[47] with a shift in the potential scale versus $FcH^{0/+}$ due to the use of a mixture of solvents taken into account for accurate comparison of $E_{applied}$.[72] The $E_{applied}$ = −0.75 V vs. $FcH^{0/+}$ used for experiments at Pt is at the onset of the reduction

peak observed by CV for all the ANHs under CO_2, while for RVC electrodes, $E_{applied}$ = −1.20 V vs. $FcH^{0/+}$ at the onset of the reduction peaks observed in CVs of **1**−**3** at GCEs.

Representative controlled potential electrolysis (CPE) plots for ANH-based reduction at Pt and RVC surfaces are shown in Figure 2.10. While the overpotential applied was greater at RVC electrodes relative to Pt electrodes, the same amount of charge is passed, allowing for comparison of product formation at both surfaces. Multiple runs are shown for **1**-**4**, indicating the reproducibility of the same operational conditions. Interestingly, **4** saturates at 15-16 C at Pt surfaces, with surface deposition of acridine again observed (Figure 2.10h). This charge corresponds to 0.2 e^- passed per acridine molecule present, and is assigned to being involved in proton reduction or CO_2 reduction before acridine passivates the electrode surface. A similar current saturation was also observed for **3** at RVC electrodes, where again, the number of passed electrons is sub-stoichiometric to the amount of **3** present in solution. However, no film deposition of **3** was observed. Due to the significant deposition of **4** observed in CV experiments, bulk electrolyses of **4** at RVC electrodes were not conducted.

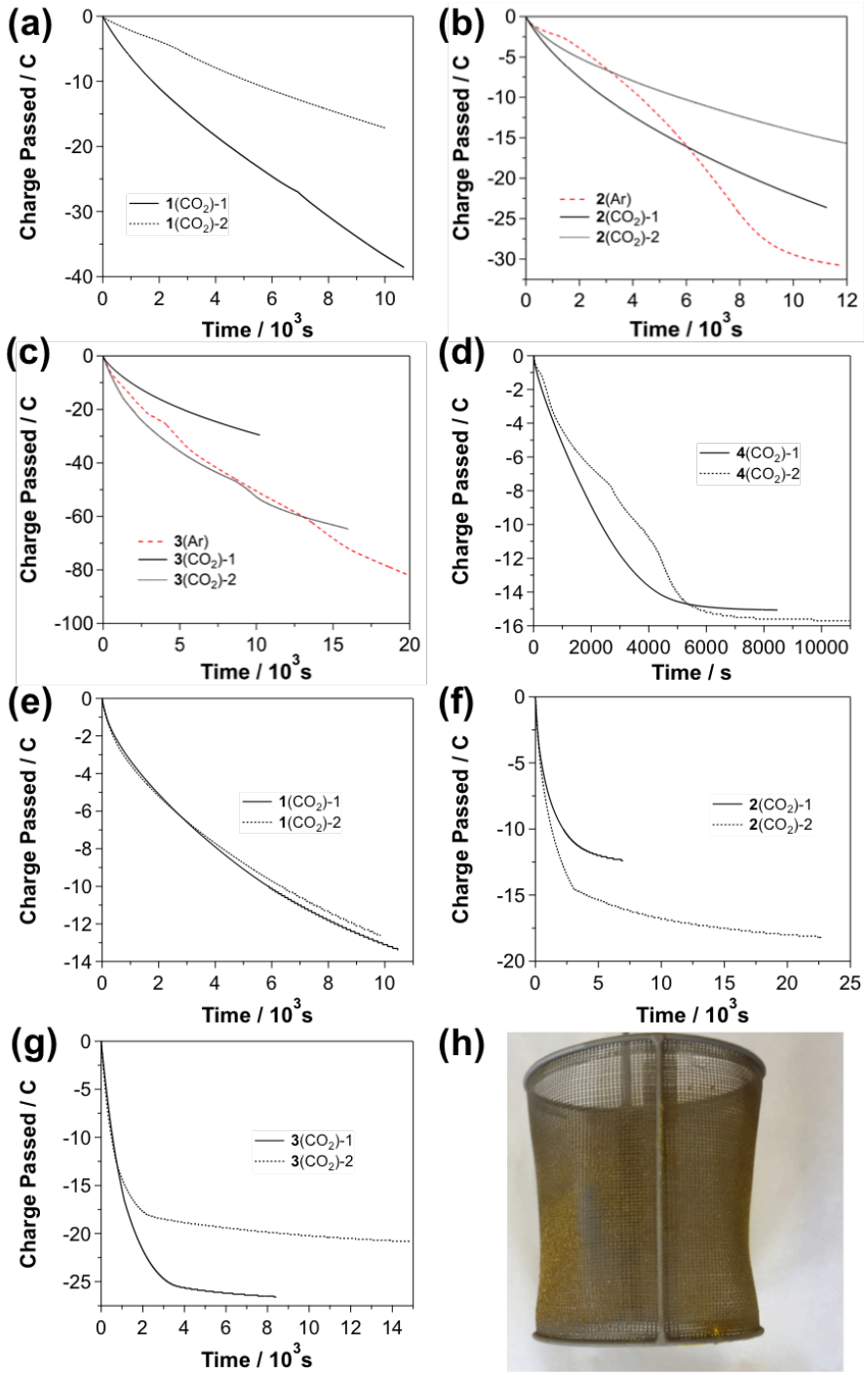

Figure 2.10. Representative plots of charge passed during bulk electrolyses of (a) **1**, (b) **2**, (c) **3**, (d) **4** under Ar (red-dashed) and CO_2 (black traces) at a Pt mesh electrode. 0.1 M $LiClO_4$, $E_{applied}$ = -0.75 V vs. $FcH^{0/+}$. Representative plots of charge passed during bulk electrolyses of (e) **1**, (f) **2**, (g) **3** under CO_2 at a RVC mesh electrode. 0.1 M $LiClO_4$, $E_{applied}$ = -1.20 V vs. $FcH^{0/+}$. (h) Film deposition of **4** after a potentiostatic bulk electrolysis at a Pt mesh electrode under CO_2. 0.1 M $LiClO_4$, $E_{applied}$ = -0.75 V vs. $FcH^{0/+}$. Adapted from Reference [67]. Copyright 2017 American Chemical Society.

To determine if additional current associated with CO_2 reduction was being observed, solutions of **2** and **3** were run under the same pH conditions (pH ~ 5) without CO_2 present. As shown in Figure 2.10, no current enhancement is seen. Rather, in the case of **2**, less charge is passed in the presence of CO_2 versus under acid alone. This could be due to a competition between CO_2 reduction and proton reduction at the electrode surface, where the reduction of CO_2 is kinetically slower than proton reduction, resulting in less charge being passed. Regardless, the majority of the charge in the case of the ANHs is attributed to proton reduction and adsorption of the ANH to the electrode surface.

Using the same CO_2 reducing conditions as the ANHs, bulk electrolyses of DHPs **3-H$_2$** and **4-H$_2$** were also conducted at Pt and RVC electrodes, with the CPE plots shown in Figure 2.11. As **4** was found to significantly deposit on RVC surfaces, **4-H$_2$** was not run on RVC electrodes for bulk electrolysis purposes. Relative to the ANH CPE plots, less overall charge is passed. This can be explained by simply looking at the CVs (Figures 2.4 and 2.9), where the relative currents of the ANHs are larger than that of the DHPs, as they can more readily undergo a weak-acid reduction mechanism, whereas the DHPs cannot. To ensure that the charge being passed in the presence of the DHPs was not simply due to background processes, **3-H$_2$** was electrolyzed in a solution under the same pH without CO_2 present at Pt surfaces. As shown in Figure 2.11, a significant enhancement in the charge passed is observed under CO_2, double the amount of charge passed under acidic conditions alone at the same timescale, indicating that an electrocatalytic event is likely occurring under these electrolytic conditions.

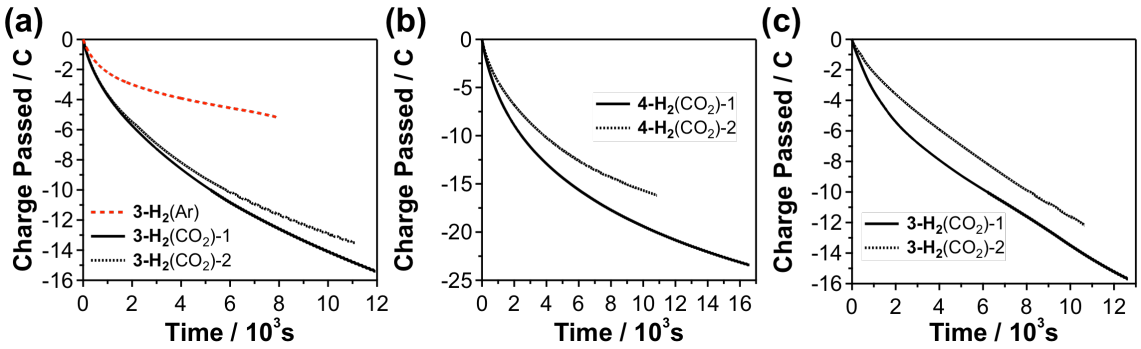

Figure 2.11. (a) Charge passed in bulk electrolyses of 10 mM **3-H$_2$** ($E_{applied}$ = -0.75 V vs. $FcH^{0/+}$, Pt mesh electrode) under Ar (red dash) and two separate runs under CO_2 (black traces); Representative CPE plots for (b) 10 mM **4-H$_2$** ($E_{applied}$ = -0.75 V vs. $FcH^{0/+}$, Pt mesh electrode) and (c) 10 mM **3-H$_2$** ($E_{applied}$ = -1.20 V vs. $FcH^{0/+}$, RVC mesh electrode). 0.1 M $LiClO_4$. Adapted from Reference [67]. Copyright 2017 American Chemical Society.

As a preliminary identification of the species resulting from ANH-based CO_2 electrochemical reduction, ^{1}H NMR spectra were collected for ANH/DHP containing electrolyzed solutions, with representative plots shown in Figures 2.12 and 2.13 for Pt and RVC surfaces. For observation of the ANH/DHP peaks as well as to qualitatively determine methanol content in electrolyzed solutions, a solvent suppression process was used, whereby the water and acetonitrile signals are suppressed during data collection. To determine if quantification of methanol could be conducted, a standard solution of methanol was used in the same solvent system and suppression method, with the methanol peak (~3.5 ppm) also being suppressed under these conditions in relation to the formic acid signal (see Appendix, Figures A1-A2). As such quantification of methanol content was not conducted. Trace amounts of methanol can be observed (singlet at ~3.5 ppm), indicating that CO_2 reduction may be occurring under the applied conditions. To ensure that the methanol observed was not due to some contaminant or background process not involving the ANH/DHP, bulk electrolysis under the same conditions was also conducted without any ANH/DHP present, with no methanol peak observed (see

Appendix, Figure A2). As no degradation of the ANH was observed via ^{1}H NMR, it can be concluded that the methanol observed is in fact a result of ANH/DHP-based CO_2 reduction.

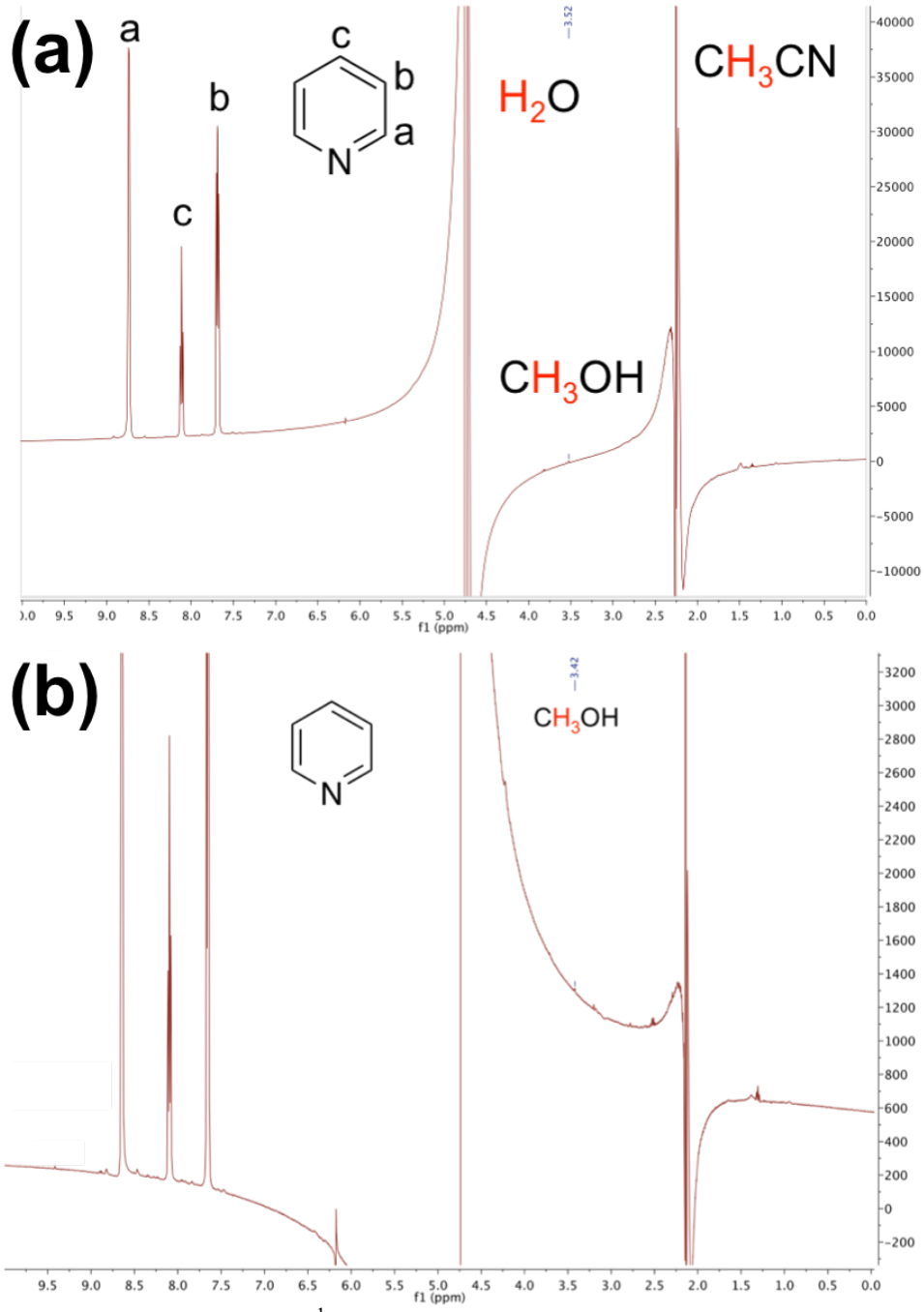

Figure 2.12. Representative ^{1}H NMR spectrum of an aliquot taken from bulk electrolysis by **1** under CO_2 at (a) Pt and (b) RVC electodes. Methanol, pyridine, water, and acetonitrile peak positions indicated on the spectrum. Adapted from Reference [67]. Copyright 2017 American Chemical Society.

When the DHP solutions are analyzed, conversion to the ANH is observed, with the DHP still the majority species in solution. Since the DHP is still relatively intact, it is likely that the DHP (rather than freshly formed ANH) is the major contributor to CO_2 reduction in these solutions (Figure 2.13). The observed methanol and formic acid are therefore not simply products of an ANH-mediated process resulting from conversion of the DHP to its parent ANH under the conditions employed. To ensure that this conversion to the ANH is not simply due to the acidic conditions or applied potentials used, the DHP was electrolyzed under similarly acidic conditions without CO_2 present. Only a small amount of the DHP was found to convert to the ANH (10% by NMR integration) under the similar acidic conditions as under CO_2, where up to 60% of the DHP was converted to the ANH (Figure 2.14). Thus, the majority of the decomposition of the DHP to the ANH is a result of the combination of an applied potential and presence of CO_2.

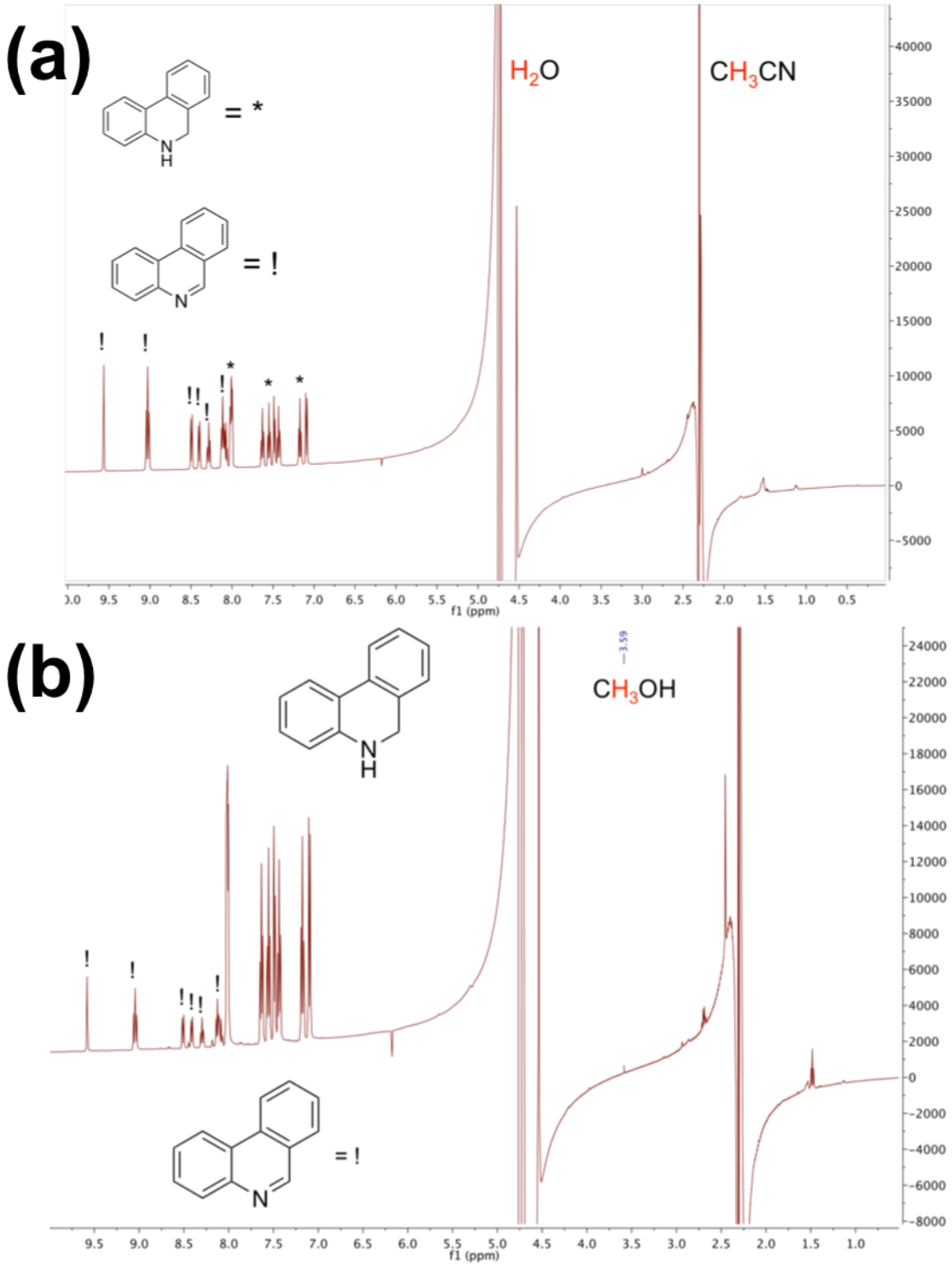

Figure 2.13. Representative ^{1}H NMR spectrum of an aliquot taken from a bulk electrolysis by **3-H$_2$** at (a) a Pt electrode and (b) a RVC electrode under CO_2. No methanol is observed in the Pt electrolysis, with overlapping aromatic peaks obscuring the formic acid region. Peaks corresponding to **3** and **3-H$_2$** are indicated. Adapted from Reference [67]. Copyright 2017 American Chemical Society.

Investigating the ANH peaks in the ANH-containing electrolyzed solutions, no formation of the DHP was observed under CO_2 reducing conditions. To try and isolate the DHP species rather than have it potentially react with CO_2, **3** was electrolyzed under the same pH conditions (pH = 5.5). No peaks corresponding to a DHP being formed were observed by ^{1}H NMR when the organic species were extracted from the solution (Figure 2.14). All the aromatic peaks observed (6-10 ppm) correspond to **3**, with no **3-H$_2$** generated. This agrees with surface studies of the electrochemical reduction of the ANH under acidic conditions and under CO_2, where no DHP generation was observed by SERS or surface-based IR-spectroscopic techniques.[43b, 56] Furthermore, no methanol was observed under these applied conditions, consistent with the methanol observed resulting from CO_2 reduction.

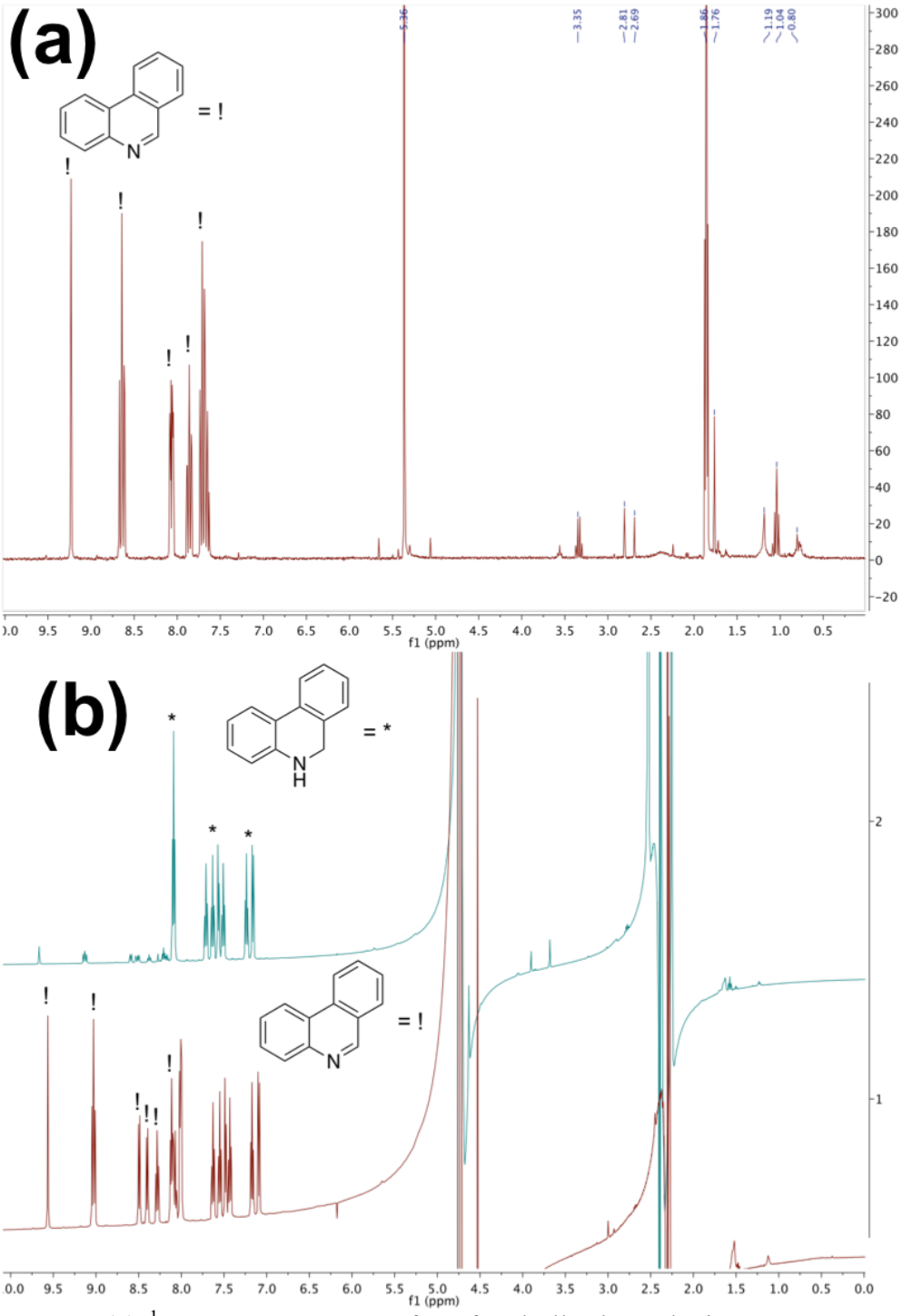

Figure 2.14. (a) ^{1}H NMR spectrum of **3** after bulk electrolysis at $E_{applied}$ = -0.75 V vs. $FcH^{0/+}$ with 0.2 equivalent $HClO_4$, at a Pt electrode. No peaks corresponding to **3-H$_2$** are observed. Residual solvent peaks are indicated. (b) Comparison of bulk electrolysis of **3-H$_2$** under Ar (blue, top) and CO_2 (red, bottom) at -0.75 V vs. $FcH^{0/+}$, at a Pt electrode, for 10 000s. 0.1 M $LiClO_4$. Peaks corresponding to **3** and **3-H$_2$** are indicated. Adapted from Reference [67]. Copyright 2017 American Chemical Society.

Confirmation of methanol content in bulk electrolyzed solutions was conducted using GC-MS and GC-FID on desalted solutions (Procedure in Section 2.2). To initially identify the presence of methanol in solution, GC-MS was conducted, with the chromatogram and mass spectra shown in Figure 2.15. Due to the co-elution of oxygen (M/Z = +32 Da) with methanol, we hesitated to quantify methanol content using GC-MS. However, the M/Z spectra corresponding to methanol is observed (isotopic peaks observed at 30.1 Da, 30.9 Da, 31.9 Da, and 33.1 Da), overlaid with the mass spectra of oxygen, indicating that methanol is in fact being produced under the CO_2 reducing conditions employed.

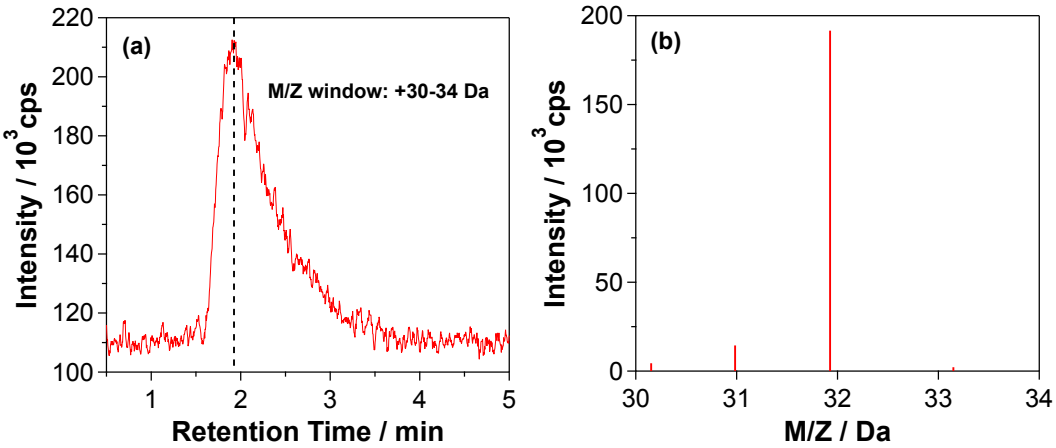

Figure 2.15. (a) GC-MS chromatogram and (b) MS signal corresponding to methanol peak in chromatogram from a bulk electrolysis sample of **3** under CO_2. An increase is observed in the peak at M/Z = +31.9 Da due to the presence of oxygen. Taken from Reference [67]. Copyright 2017 American Chemical Society.

For quantification of methanol content, GC-FID on bulk electrolyzed samples was conducted, with the retention times determined using standard solutions of methanol in similar solvent mixtures (see Appendix, Figure A5). To address concerns over the sensitive nature of this analytical technique to pre-treatment of the instrument[48, 61] and the low concentrations generated from bulk electrolysis, a CH_3CN/H_2O blank mixture was passed through the column in quintuplicate before and after analyses of electrolysis (run

first) and standard solutions, respectively. The GC-chromatograms for bulk electrolyzed solutions at Pt and RVC surfaces are shown in Figure 2.16. As can be seen, while methanol is observed, it is in low amounts (10-250 μM), with the acetonitrile peak occurring shortly after. Furthermore, there is a reduction in the amount of methanol generated from bulk electrolyses conducted at RVC surfaces in comparison to the Pt surfaces while still passing the same amount of charge, indicating that a secondary process is likely becoming more prominent at RVC surfaces.

The largest component of the error in the reported values based on GC-FID is attributed to sample-to-sample reproducibility in bulk electrolysis rather than the detection limit or consistency of the instruments used. No increase or decrease in methanol content was observed over a storage period of three months. To ensure that the methanol observed was not due to some impurity that could not be observed under ^{1}H NMR, electrolyzed solutions without ANH/DHP present were put under the same conditions, with no methanol peak occurring, again confirming that methanol is a result of the electrolysis of ANH/DHP under CO_2 reducing conditions.

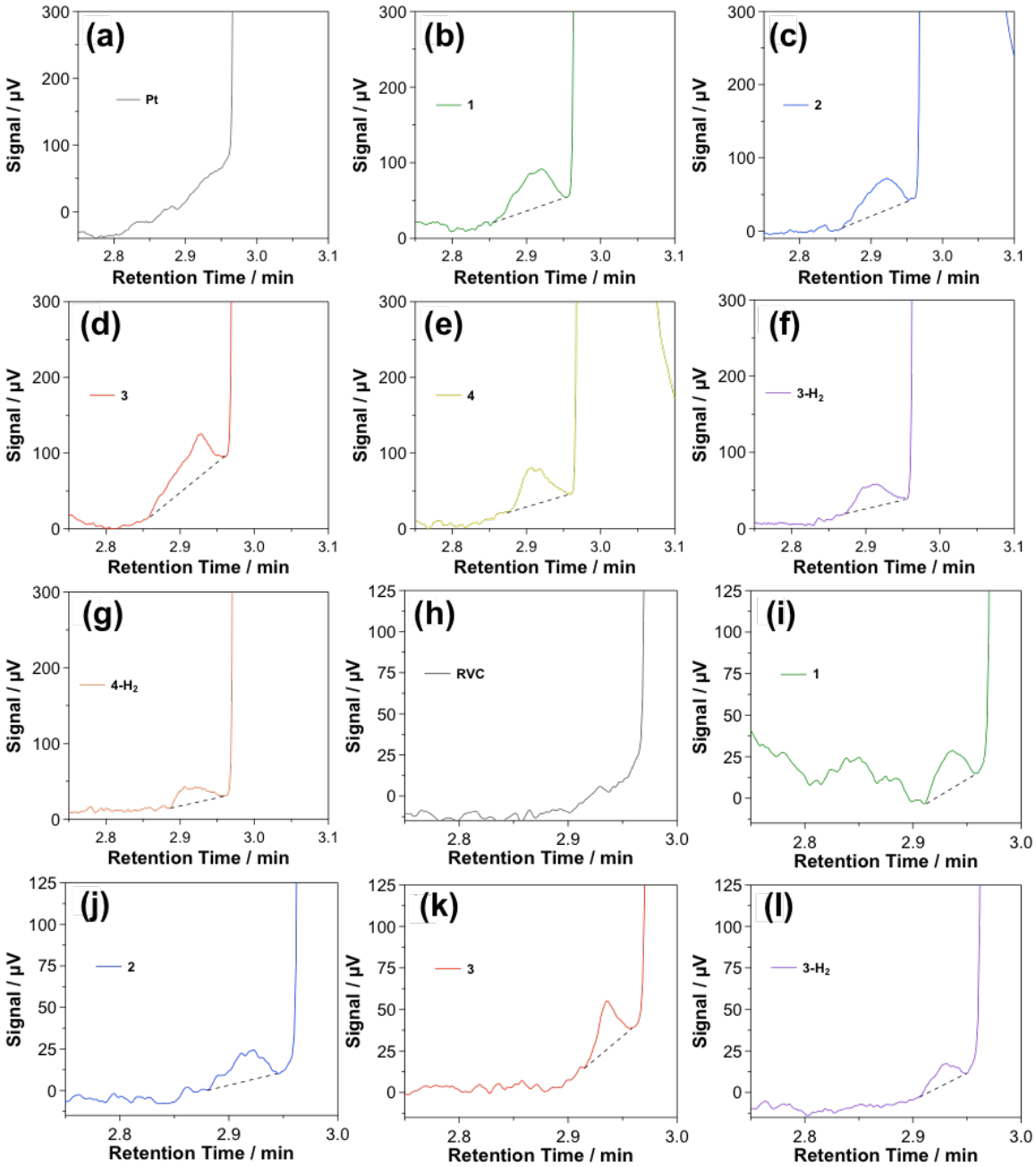

Figure 2.16. GC-FID traces of de-salted samples from bulk electrolyses of (a) blank, (b) **1**, (c) **2**, (d) **3**, (e) **4**, (f) **3-H$_2$**, and (g) **4-H$_2$** under CO_2 at a Pt mesh electrode. GC-FID traces of de-salted samples from bulk electrolyses of (h) blank, (i) **1**, (j) **2**, (k) **3**, and (l) **3-H$_2$** under CO_2 at a RVC mesh electrode. Solvent peak at 3.0 min; dashed line represents baseline used for integration. Adapted from Reference [67]. Copyright 2017 American Chemical Society.

For identification and quantification of formic acid content, LC-MS was conducted on bulk electrolyzed samples. Due to the tolerance of the column and

conditions employed to salt content, no desalting process was necessary. As with methanol determination, low amounts of formic acid were generated under bulk electrolysis (10-250 μM), with the chromatograms shown in Figures 2.17 and 2.18. Due to the less sensitive nature of the formic acid determination, larger corresponding errors were determined for the formic acid content of electrolyzed samples. To again ensure that the formic acid observed is a result of ANH/DHP based electrolysis of CO_2, blank solutions were electrolyzed and passed through the LC-MS, with no formic acid observed at Pt surfaces. At RVC surfaces, some formic acid was produced without any ANH or DHP present. Given the potential applied, this agrees with other work investigating the reduction of CO_2 at GCEs, where trace amounts of formic acid are observed. Thus, while low amounts are observed, the methanol and formic acid observed via ^{1}H NMR, GC-MS, GC-FID and LC-MS are the result of ANH/DHP based reduction of CO_2 under electrochemically reducing conditions rather than solely by some background process or impurity.

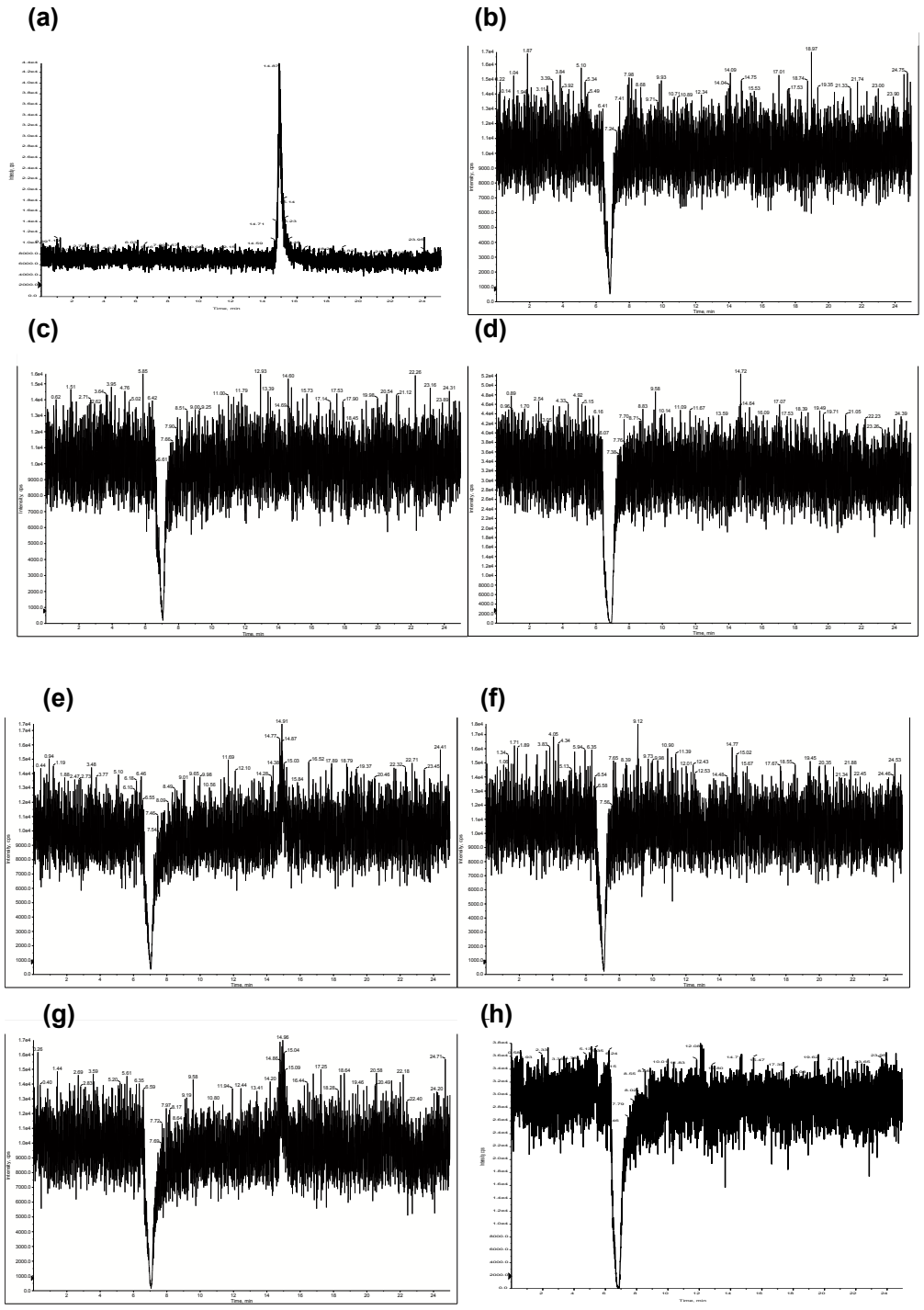

Figure 2.17. Representative LC-MS traces at M/Z = -45 Da of (a) standard (130 μM HCOOH), and bulk electrolyses of CO_2 by (b) Pt, (c) **1**, (d) **2**, (e) **3**, (f) **4**, (g) **3-H$_2$**, (h) **4-H$_2$** at $E_{applied}$ = -0.75 V vs. $FcH^{0/+}$, 0.1 M $LiClO_4$. Taken from Reference [67]. Copyright 2017 American Chemical Society.

With the main products formic acid and methanol quantified, the %FE and TONs can be determined as shown in Table 2.3. Due to the low concentrations of products generated, the TONs and the TOFs reported for this system are substoichiometric relative to the amount of DHP/ANH added and time required for bulk electrolysis, in line with the literature on **1**.[24, 47] CO and H_2 determination was not conducted in this work. For DHPs **3-H$_2$** and **4-H$_2$**, %FEs determined from bulk electrolysis experiments at Pt are comparable with those observed for parent ANHs **3** and **4**. Furthermore, electrolysis of **3-H$_2$** at RVC also led to methanol and formate production with %FE similar to that seen at Pt electrodes, and with %FE higher than that observed for **3** at RVC electrodes. This demonstrates that isolated DHPs can function as additives in a fashion similar to that of their parent ANHs, which is consistent with the proposed role of DHPs as intermediates relevant in ANH-mediated reduction of CO_2 to methanol.[55b, 57b]

No reduced products were detected when electrolysis of **3-H$_2$** under CO_2 was performed at the potential applied at Pt surfaces (−0.75 V vs. $FcH^{0/+}$) at RVC electrodes, and little to no charge was passed. This agrees with previous CV studies by Bélanger of **1/[1-H]$^+$** at RVC electrodes,[46] where it was observed that there was a significant increase in the overpotential for CO_2 reduction facilitated by **1** moving from Pt to RVC surfaces. This increase in overpotential is attributed to the inertness of the RVC electrode to both CO_2 reduction and proton reduction,[75] which can allow for other reduction mechanisms to become more prominent such as surface deposition. Thus, the DHP/ANH-based CO_2 reduction in this work appears to be surface-dependent, with a DHP outperforming its ANH counterpart at more inert surfaces.

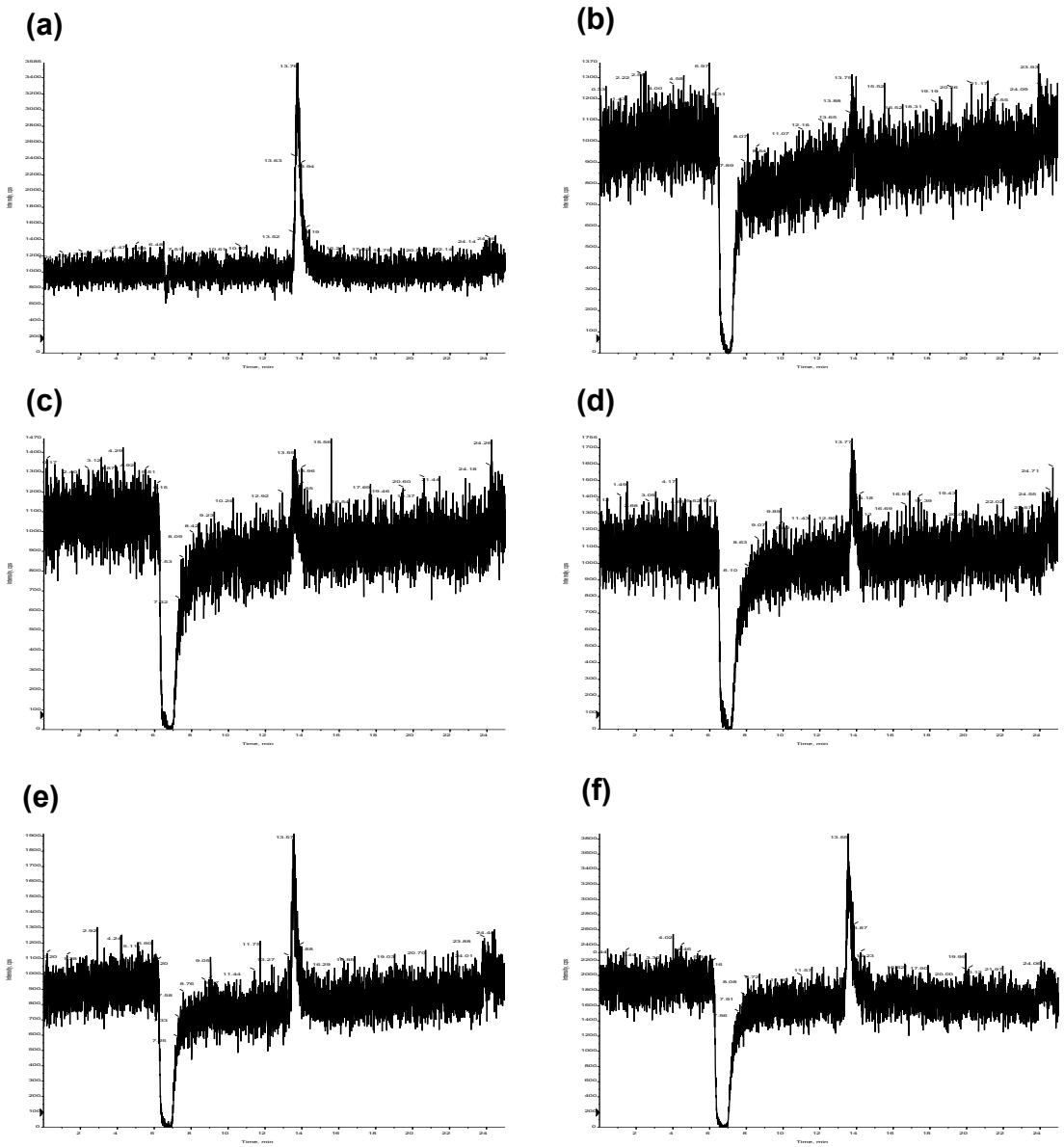

Figure 2.18. Representative LC-MS traces at M/Z = -45 Da of bulk electrolyses of CO_2 by (a) standard (26 μM HCOOH), and bulk electrolyses of CO_2 by (b) RVC, (c) **1**, (d) **2**, (e) **3**, (f) **3-H$_2$** at $E_{applied}$ = -1.20 V vs. $FcH^{0/+}$, 0.1 M $LiClO_4$. Taken from Reference [67]. Copyright 2017 American Chemical Society.

Table 2.3. Faradaic efficiencies for electrochemical CO_2 reduction in the presence of DHP or ANH additives. Copyright 2017 American Chemical Society.

ANH/ DHP	Electrode	%FE CH_3OH[a]	%FE $HCOO^-$	TON CH_3OH (10^{-3})	TOF CH_3OH (10^{-3} hr^{-1})	TON $HCOO^-$ (10^{-3})	TOF $HCOO^-$ (10^{-3} hr^{-1})
1	Pt	30(10)	not det.[b,c]	12.0(1.0)	4.3(4)	-	-
1	RVC	7(7)	1.0(0.3)[b,c]	0-4	0-1	0.76(24)	0.27(8)
2	Pt	36(16)	4(6)[b,c]	15(7)	5.2(2.7)	6.6(9)	2.1(4)
2	RVC	11(7)	4(3)[b,c]	3.9(1.9)	1.4(9)	0.8-20	0.2-5
3	Pt	12(8)	4(1)[b,c]	7(3)	2.5(1.2)	5.4(1.0)	1.9(4)
3	RVC	5(3)	1.1(0.2)[b,c]	2.2(1.6)	0.8(6)	1.56(22)	0.54(19)
3-H_2	Pt	19(7)	3(4)[b,c]	9(3)	1.9(5)	0-8	0-2
3-H_2	RVC	15(7)	8(3)[b,c]	4.3(2.4)	1.3(6)	5.9(2.2)	1.9(8)
4	Pt	17(13)	not det.[b,c]	6(4)	2.1(1.6)	-	-
4	RVC	-[d]	-[d]	-	-	-	-
4-H_2	Pt	13(10)	not det.[b,c]	4(3)	1.2(9)	-	-
4-H_2	RVC	-[d]	-[d]	-	-	-	-

[a]Via peak area of GC-FID traces with standard deviation of bulk electrolysis samples. [b]Via peak area from LC-MS traces. [c]Signals for ANH overlap with product signals in ^{1}H NMR. [d]Significant electrode fouling (deposition).

Turning to the ANHs themselves, CO_2 reduction in the presence of an ANH additive was also seen at more inert electrode surfaces (RVC) at more reducing potentials.[46] ANHs **1**−**3** all exhibit a significant drop in %FE at RVC compared to Pt electrodes with no products detected at a lower $E_{applied}$ (−0.75 V vs. $FcH^{0/+}$; RVC). The %FEs determined in this work for **1** are slightly higher, though not statistically different within error, than %FEs reported for aqueous cells in the literature; however, it should be noted that in a mixed organic/aqueous solvent system CO_2 is expected to be more soluble,[21] and direct comparisons to literature %FEs should be made cautiously. Quinoline (**2**), recently proposed as a viable ANH additive on thermodynamic considerations,[59a] exhibits the highest overall %FE and the highest methanol production of the series at both electrode surfaces. Pyridine (**1**) and acridine (**4**) exhibit the highest selectivity for methanol formation, with no formate observed by ^{1}H NMR or LC-MS at

Pt, indicating only trace amounts produced under the experimental conditions employed. Unlike the previously reported correlation between pK_a and total Faradaic yields,[52] the highest overall activity is observed for the ANH with an intermediate pK_a (**2**), with lower %FEs observed for ANHs with higher (**1**, **4**) and lower (**3**) pK_a's. The ease with which an ANH participates in a "weak acid" reduction to form H_{ads} is apparently not %FE-determining in our system. This agrees with the observation that acetic acid, which has a pK_a close to **[1-H]**$^+$, does not mediate methanol production.[48]

The differences in %FE observed at Pt compared with RVC for the ANH series and the lower applied potential is consistent with an important role for the electrode surface in the observation of CO_2 reduction.[30, 53, 57b] Nevertheless, we tested the possibility of a homogeneous reaction between CO_2 and DHPs **3-H$_2$** and **4-H$_2$** by conducting NMR scale reactions of **3-H$_2$/4-H$_2$** under CO_2 (1 atm) in CD_3CN/D_2O (1:0.1 v:v) in Teflon-capped J-Young valve tubes to probe chemical reactivity in the absence of an electrode surface or applied potential. To ensure no degradation of the DHPs due to the presence of oxygen, the mixture was degassed through three freeze-pump-thaw cycles, and subsequently placed under 1 atm of CO_2. While the presence of residual ANH is observed initially, ^{1}H NMR analysis showed no appreciable conversion of the DHP to ANH at room temperature. No CO_2-derived products such as methanol, formic acid or formaldehyde (9.6 ppm) could be observed above the background, nor was any H_2 generation (4.6 ppm), or H/D scrambling observed after three hours (Figure 2.19), in agreement with reported results for **1/1-H$_2$** mixtures under CO_2, and **1** under CO_2 in the presence of acid and Pt nanoparticles.[24, 51]

The absence of direct chemical reaction suggests that participation of the electrode surface and an applied potential is critical for CO_2 reduction mediated by a preformed DHP in an electrochemical system. Recent computational analysis of the CO_2 reduction pathway to CO at Ag (111) surfaces indicates that product formation is stabilized by the electric field resulting from the increased presence of cations at the electrode surface under reducing conditions.[78] Similarly, in the ANH/DHP-based system, the increased presence of protonated ANH-species or DHP-species at the surface under reducing conditions may help stabilize CO_2 reduced intermediates. However, there exists a limit as to how much ANH/DHP could be added to the solution, whereby stabilization of the CO_2 reduction process is superseded. For instance, the reduction of CO_2 to methanol has been shown to occur in the presence of pyridine at $CuInS_2$ electrodes.[50] When the concentration of pyridine is increased, however, a strong surface adsorption of pyridine occurs, slowing down the CO_2 reduction rate, effectively poisoning the electrode surface.[79]

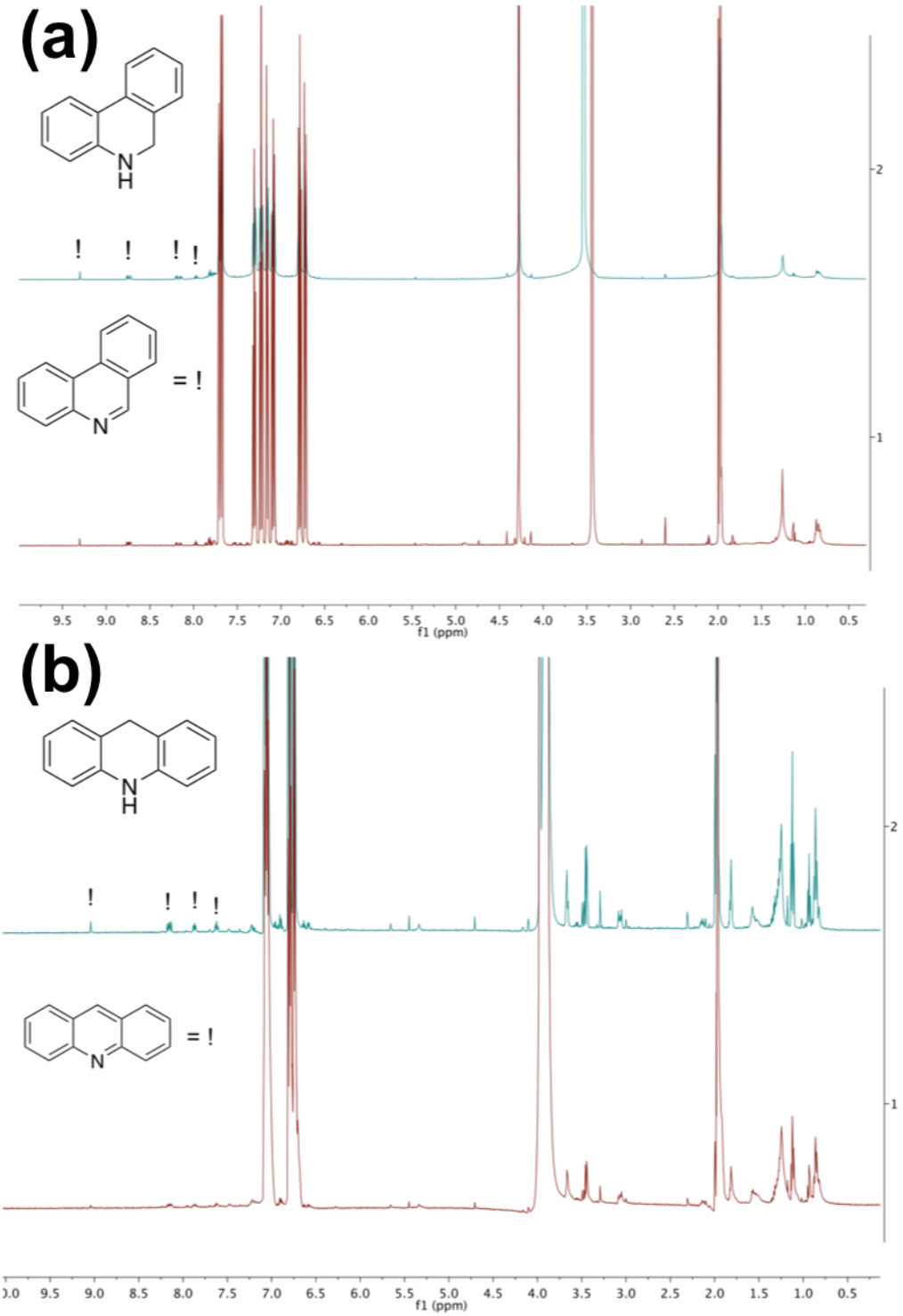

Figure 2.19. (a) ^{1}H NMR spectrum of the chemical reaction between **3-H$_2$** (5 mg) and CO_2 (1 atm) in D_2O/CD_3CN (10% v/v) before (red) and after (blue) 3 h at room temperature. (b) ^{1}H-NMR of the chemical reaction between **4-H$_2$** (6 mg) and CO_2 (1 atm) in D_2O/CD_3CN (10% v/v) before (red) and after (blue) 3 h at room temperature. DHP and ANH peaks are indicated on each spectrum. Adapted from Reference [67]. Copyright 2017 American Chemical Society.

2.4 Discussion

The potentials applied in this work for bulk electrolysis experiments are well positive of those reported necessary for direct CO_2 reduction in acetonitrile/water mixtures at a Pt electrode (-2.0 to -3.5 V vs. $FcH^{0/+}$).[21] Background CO_2 reduction by glassy carbon alone has been reported to occur at potentials 600 mV more negative than those applied here, and accordingly only trace amounts of formate and no methanol were observed in our experiments in the absence of added ANH/DHP.[80] All bulk electrolyses of the ANHs and DHPs at Pt and RVC electrodes were conducted a minimum of three times, with no increase or decrease in methanol or formate content observed over a storage period of three months. Thus, we conclude that any methanol or formate observed is a result of bulk electrolysis of ANH under CO_2 rather than a contaminant in the systems used in this work.[48, 61]

If the reactivity of ANH additives **1**−**4** is via formation of a DHP, the comparably high activity of **2** is derived from a balance between the Lewis acidity of the parent ANH (ease of formation of a DHP, lower susceptibility to side reactions) and hydride donor ability of the DHP once formed. This agrees with the Sabatier principle for ANH-based CO_2 reduction as proposed by Keith (see Chapter 1, Figure 1.8), where Brønsted acidity and hydride donor ability must be balanced to manage both H^+ and H^- transfer to CO_2.[59]

While phenanthridine (**3**) and acridine (**4**) mediate reduction of CO_2 with similar %FEs, **4** additionally undergoes a more prominent deposition process. Access to *ortho*- (available in **3**, not available in **4**) or *para*-positions (available in **4**, not available in **3**) likely governs the interaction of an ANH at the electrode surface. Electrochemical deposition of 1,10-phenanthroline in acid, for example, was shown to occur via covalent modification of GCE surfaces through the *para*-position of the ANH.[81]

Given the electrode dependence of the %FEs for CO_2 reduction by ANHs and the absence of product formation by DHPs both without any applied potential or at RVC electrodes at lower $E_{applied}$ (−0.75 V vs. $FcH^{0/+}$), a strictly solution-based DHP mechanism for CO_2 reduction appears unlikely.[55b] Lessio *et al.* recently established that a surface-bound 2-pyridinyl radical formed via transfer of photoexcited electrons from p-GaP to **[1-H]**$^+$ is thermodynamically feasible *in silico* and is calculated to be more reactive than the more stable surface-adsorbed DHP $\mathbf{[1\text{-}H_2]_{ads}}$ (Figure 2.20).[57b] Both are proposed as competent intermediates in ANH-mediated photoelectrochemical CO_2 reduction at p-GaP.

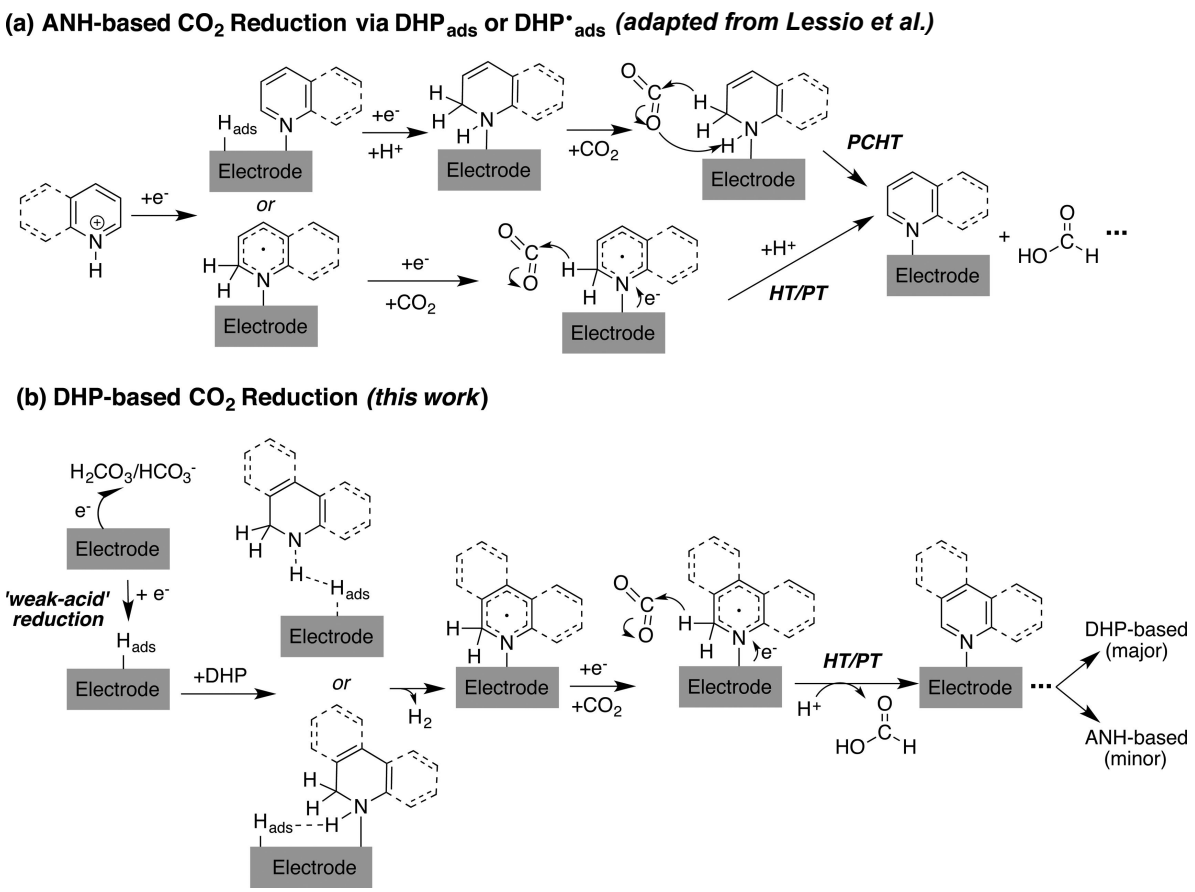

Figure 2.20. (a) Mechanism for ANH-based CO_2 reduction via DHP_{ads} or $DHP^{\bullet}_{ads}$; PCHT, proton-coupled hydride transfer. (Adapted from Reference [57b]. Copyright 2016 American Chemical Society.) (b) Proposed mechanism for observed CO_2 reduction in the presence of isolated DHP additives (this work) via formation of a surface-bound DHP-derived radical, $DHP^{\bullet}_{ads}$. HT, hydride transfer; PT, proton transfer. Only the initial reduction to HCOOH is illustrated, with subsequent steps leading to CH_3OH formation occurring in a similar fashion. Taken from Reference [67]. Copyright 2017 American Chemical Society.

In the system investigated in this work, reactivity via surface-adsorbed $\mathbf{[3\text{-}H_2]_{ads}}$ would not necessarily account for the appearance of a reductive event in CVs of $\mathbf{3\text{-}H_2}$ under CO_2. Formation of a surface-bound DHP-derived radical ($DHP^{\bullet}_{ads}$) via H_{ads} would explain the observation that different potentials are required for methanol and formate production in bulk electrolyses of DHPs $\mathbf{3\text{-}H_2}$ and $\mathbf{4\text{-}H_2}$ at RVC compared with Pt, because the surfaces require different potentials for H_{ads} formation, and that no

homogeneous reactivity occurs between **3-H$_2$/4-H$_2$** and CO_2 in the absence of an electrode or potential. The mechanism proposed in Figure 2.20 would account for all the components required to observe methanol production: **3-H$_2$**, CO_2, a surface, and a sufficiently reducing potential. Participation of H_{ads} (formed via 'weak-acid reduction' of carbonic acid in solution, as observed in the background current of CO_2 alone)[53] accounts for the difference in potential required for methanol production at RVC versus Pt. CO_2 reduction is postulated to then occur via hydride transfer from the DHP-derived surface species, potentially stabilized by surface-organized waters,[57-58] followed by proton transfer from the acidic solution completing the initial reduction to formic acid.

Bulk electrolyses of ANHs under CO_2 in dry, acidified CH_3CN at RVC and Pt electrodes resulted in no observable CO_2 reduction products, indicating a critical role for water in the reduction mechanism. The formation of H_{ads} also appears to be critical to the activity of ANH additives and we cannot distinguish here between a PCHT mechanism[53] or reactivity of a surface-bound DHP_{ads} or DHP-derived radical generated via H_{ads}, as proposed by Carter and co-workers.[57b] The decrease in %FE of the ANHs moving from Pt to RVC could result from increased ANH adsorption on RVC surfaces, though only **4** was observed to form a noticeable film after electrolysis under CO_2 at Pt surfaces and after one CV cycle at GCEs.

2.5 Conclusions

This work presents the first evidence for the participation of isolated dihydropyridine-type species in surface dependent electrochemical CO_2 reduction. This is based on the following observations: (1) Methanol and formic acid are generated in electrolyses of isolated DHPs **3-H$_2$** or **4-H$_2$** under 1 atm of CO_2 at both Pt and RVC electrodes; (2) CV and NMR studies show that the parent ANHs **3** and **4** are not

generated from the corresponding DHPs in appreciable amounts in the absence of CO_2, ruling out ANH-only mediated activity; (3) No homogeneous reactivity is observed between DHPs **3-H$_2$** or **4-H$_2$** and CO_2 in the absence of an electrode surface/applied potential; (4) DHP **3-H$_2$** exhibits an electrode dependence (Pt versus RVC) on the $E_{applied}$ required to observe methanol production, though not on the observed %FE.

The ability to carry out electrochemical CO_2-to-methanol conversion using carbon-based electrodes instead of precious metals such as Pt or Pd is an important milestone for the scaleability of reduction schemes employing DHP or ANH additives.[80, 82] Consistent with previous studies on **1**, however, the overall yields of reduced organic products in our experiments remain substoichiometric, even in reactions mediated by preformed DHPs. Moreover, we did not observe evidence of electrochemical generation of DHP **3-H$_2$** from ANH **3**. These experimental findings will hopefully motivate better understanding of the mechanism of multi-H^+/e^- processes occurring in CO_2 electrochemical reduction in the presence of simple organic additives and lead to improvements in turnover numbers, for example, by targeting biomimetic hydride shuttles capable of cooperative interactions with electrode surfaces and electric potentials.[83]

CHAPTER 3: Formic Acid Reduction Mediated by Aromatic *N*-Heterocycles: Methanol Production and the Observation of Electrochemical Generation of Dihydrophenanthridine

3.1 Introduction.

In Chapter 2, it was demonstrated that when pre-formed DHPs such as 1,2-dihydrophenanthridine (**3-H$_2$**) or 9,10-dihydroacridine are added to mixed aqueous/organic solutions of CO_2 and an appropriately reducing potential applied, methanol and formate can both be identified as products of bulk electrolysis, with similar %FE as observed in the presence of their parent ANHs.[67] These results support the viability of dihydropyridines (DHPs) as relevant intermediates in aromatic *N*-heterocycle (ANH) mediated electrochemical CO_2 reduction. However, the formation of DHPs in electrolyzed solutions of their parent ANHs was not observed under the conditions investigated. Given the low (sub-stoichiometric) turnover numbers of ANHs in CO_2 reduction, it is anticipated that if DHPs play a role, they are generated in relatively small amounts. We further hypothesized that by supplying a sufficiently acidic solution, DHP generation and methanol production might be observed simultaneously. Thus, the direct electrochemical reduction of formic acid (HCOOH), a proposed intermediate in CO_2, to methanol conversion by ANH additives, was investigated (Figure 3.1). We chose phenanthridine (**3**) as the ANH additive as (i) the corresponding DHP (**3-H$_2$**) has been shown to facilitate methanol production from CO_2 (see reference [67] and Chapter 2); (ii) formation of only one DHP isomer (1,2-dihydrophenanthridine) is possible, simplifying its characterization in solution; and (iii) the DHP **3-H$_2$** is stable enough to facilitate characterization, but reactive enough to act as a transfer hydrogenation agent.[84]

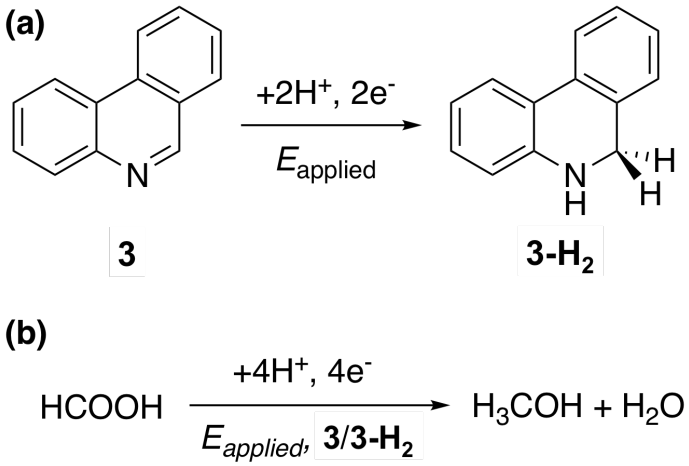

Figure 3.1. Schematic for (a) the electrochemical reduction of ANH **3** to DHP **3-H_2**; (b) the electrochemical reduction of formic acid to methanol in the presence of **3**/**3-H_2** attempted in this work.

3.2 Experimental

3.2.1 Materials

All chemicals and reagents were used as received unless otherwise noted. Solutions for electrochemical experiments were made using MilliQ water (18.2 Ω·cm) and HPLC grade CH_3CN, with $LiClO_4$ (98%, Sigma) as the supporting electrolyte. Pyridine (**1**, 98%, Fisher Scientific), quinoline (**2**, 99%, Acros Organic), and phenanthridine (**3**, 98%, Acros Organic) were used as received in 1 to 10 mM concentrations in non-aqueous (CH_3CN), and mixed solutions (10%, 60% (v:v) H_2O /CH_3CN). Formic acid (HCOOH, 98% Alfa Aesar), acetic acid (AA), and perchloric acid ($HClO_4$) were used as received in 3 to 1000 mM concentrations. $LiAlH_4$ (Sigma) and diethyl ether were used as received for synthesis of DHP-species **3-H_2** and **4-H_2**. Tetrahydrofuran (THF) was dried using sodium wire (benzophenone indicator) prior to use.

3.2.2 Synthetic Methods

Synthesis of 1,2-Dihydrophenanthridine (3-H_2)

The synthesis of 1,2-dihydrophenanthridine (**3-H_2**) was conducted as described in Section 2.2.2.

3.2.3 CV Experiments

CV experiments were performed on a CHI 760c bipotentiostat at scan rates of 50-800 mV s^{-1} using freshly polished (with 0.05 μm alumina paste) Pt or glassy carbon (GCE) disc working electrodes, a Pt wire counter electrode, and a Ag/AgCl aqueous quasi-reference electrode. Ferrocene was added as an internal standard to each solution upon completion of all cyclic voltammetry experiments, allowing potentials to be referenced to the ferrocene/ferrocenium ($FcH^{0/+}$) redox couple. To account for the use of a mixed solvent system, any shift of the $FcH^{0/+}$ redox couple due to the CH_3CN/H_2O ratio employed was considered, as previously described.[72]

3.2.4 Bulk Electrolysis Experiments

Bulk electrolyses were conducted using a Pt mesh electrode (125 cm^2) and a reticulated vitreous carbon (RVC) electrode (~ 700 cm^2) with Ar constantly bubbled into the solution (1 atm) and the solution stirred, with a graphite rod counter electrode in a fritted tube and a Ag/AgCl quasi-reference electrode (total volume of 90 mL). Potentials ranging from -0.50 V vs. Ag/AgCl (-0.83 V vs. $FcH^{0/+}$) to -0.90 V vs. Ag/AgCl at Pt mesh, and –0.90 V versus Ag/AgCl (-1.23 V vs. $FcH^{0/+}$) at RVC electrodes, to -1.1 V vs. Ag/AgCl (-1.43 V vs. $FcH^{0/+}$), were applied for all ANHs investigated for approximately 10 000 s.

3.2.5 Product Analysis

NMR Characterization Protocol

NMR Technique for Synthetic & Isolated Products

For analyses of isolated, synthetic products, NMR experiments were performed on a 300 MHz NMR spectrometer (Bruker) on 5-30 mg of the product in 0.6 mL $CDCl_3$ or CD_3CN. 1D techniques such as ^1H and ^{13}C NMR, as well as 2D techniques such as Heteronuclear Single Quantum Coherence-Distortionless Enhancement by Polarization Transfer (HSQC-DEPT) were used for product identification.

NMR Technique for Electrolyzed Solutions.

^1H NMR spectroscopic analyses were performed on a 500 MHz spectrometer (Bruker) using aliquots (0.6 mL) taken directly from the electrolyzed solution and mixed with 0.06 mL CD_3CN, allowing any conversion of the ANH to the DHP to be observed. A pulse sequence suppression was applied to peaks attributed to H_2O (~3.1 ppm) and CH_3CN (~2.0 ppm) peaks, with a delay time of 3.0 s, a 12 μs pulse width, and 0.82 s acquisition time. Due to the large water peak appearing in the methanol peak region, methanol quantification could not be conducted using ^1H NMR spectroscopy.

GC-FID Characterization Protocol

Methanol quantification was also conducted using GC-FID. Prior to injection into the GC, the electrolyzed solution was desalted by a bulb-to-bulb transfer of the volatiles (see Section 2.2.5 in Chapter 2). A 1.0 μL aliquot of the desalted solution in a 1/10 split was then injected into the GC, with the headspace heated to 250 °C and a Supelco Wax column heated at 50 °C for 3 min, raised to 160 °C over 9 min, and maintained for

another 4 min, at a flow rate of 1 mL/min. Methanol content was determined by analyzing the peak produced at a retention time of 6.7 to 6.9 min in the chromatogram, as determined from standard solutions, using CompassCDS 3.0 Software (Bruker) (solvent peak arises at 8.5 min). A linear baseline correction was used for all GC-FID peak integrations conducted in this work, with the peak area determined for each sample to be in the range of 0.8-6.0 μV*min, and with an error of 0.6 μV*min (corresponding to integrating the noise in the blank samples at 6.8 min, 10-80% of the corresponding peak area in the bulk electrolysis samples) from the integration method used. The concentration of methanol was determined through comparison to an external calibration curve. To account for any drift associated with the instrument, the retention times for methanol were determined through comparison to a standard each day samples were run. Care was taken to ensure no contamination from residual methanol from standards prior to running samples.

UV-Vis Spectroscopy Protocol

To identify any production of a DHP species in electrolyzed solutions, UV-Vis Absorbance spectra of **3**, and **3-H$_2$** was conducted on a Cary 50 spectrophotometer using air-tight fused quartz cuvettes (1 cm path length) in the range of 190-1100 nm in 10^{-5}-10^{-6} M concentrations, allowing the oxidized and reduced forms of **3** to be distinguished.

Determination of the pK_a of 1-4

The determination of the pK_a for the conjugate acid of **1-3** was determined using a weak base-strong acid titration in 10% (v:v) H_2O/CH_3CN, with $HClO_4$ acting as the strong acid, as described in Chapter 2, section 2.2.5.

3.3 Results

3.3.1 CV Results

CV studies were conducted on solutions of **3** in the presence of formic acid (HCOOH) to explore the behavior of an ANH in HCOOH-containing solutions. In the absence of **3**, HCOOH was found to exhibit an irreversible reduction at both Pt and RVC surfaces in 60% and 10% (v:v) water/acetonitrile mixtures (Figure 3.2), and is assigned to proton reduction by formic acid based on literature studies of formic acid at Pt surfaces.[85] A 150 mV cathodic shift in the HCOOH reductive wave is observed going from 60% to 10% water mixtures, going from -0.95 V to -1.1 V. Addition of **3** resulted in a 100-150 mV anodic shift in this reductive wave at Pt surfaces to -0.77 V in 60% (v:v) H_2O/CH_3CN, close to the reported $E_{1/2}$ value of -0.73 V for the phenanthridium redox couple in Chapter 2 (Figure 2.3; pH < pK_a).[67] In 10% (v:v) H_2O/CH_3CN, the $E_{1/2}$ for the **3**/**[3-H]**$^+$ couple is shifted cathodically 140 mV to -0.91 V. This shift is similar in size to the cathodic shift observed for HCOOH going from 60% to 10% water mixtures, and is similar to the reported trend for proton reduction in water:acetonitrile mixtures and in organic media, where the increased presence of acetonitrile results in an increase in the necessary overpotential for proton reduction.[66, 72] As such, the 150 mV shift observed when the solution was altered from 60% to 10% water mixtures is attributed to the increase in acetonitrile content rather than a change in the nature of the reduction process occurring. The irreversible nature of this reduction event in both 60% and 10% water mixtures precluded any Randles-Sevcik analysis. Thus, as in Chapter 2, the weak-acid mechanism is maintained in HCOOH-based solutions containing **3**, and as no deposits were observed on the electrode surface, is assumed to be a solution-based or weakly

adsorbing reductive process. However, in this case, the more strongly acidic solution (pH ~ 3) appears to lead to greater rates of H_2 evolution, diminishing the return wave typically observed for oxidation of H_{ads} on the return scan.

No significant current enhancement was observed upon addition of **3** to HCOOH-containing solutions (7% increase at Pt surfaces in 10% H_2O in CH_3CN). In fact, in 60% water mixtures, a reduction in the current is observed at Pt surfaces. These results are similar to the results obtained under CO_2 in Chapter 2 (Figure 2.3), where it was concluded that the CO_2 reduction process was not observable on the CV timescale (see Chapter 2).[47, 67] The reduction of HCOOH (as opposed to proton reduction) in the presence of an ANH is also not observable on the CV timescale at Pt surfaces. At RVC electrodes, the irreversible reductive peak that appears at ca. -1.3 V when **3** is added into both 10% and 60% H_2O solutions is attributed to weak acid reduction of the ANH at GCEs (Figure 3.2; also see Figure 2.5), where the cathodic shift in the reductive wave is a result of the inability of RVC electrodes to produce hydrogen as readily as at Pt surfaces, allowing other processes, such as increased surface interactions, to occur.[46, 75]

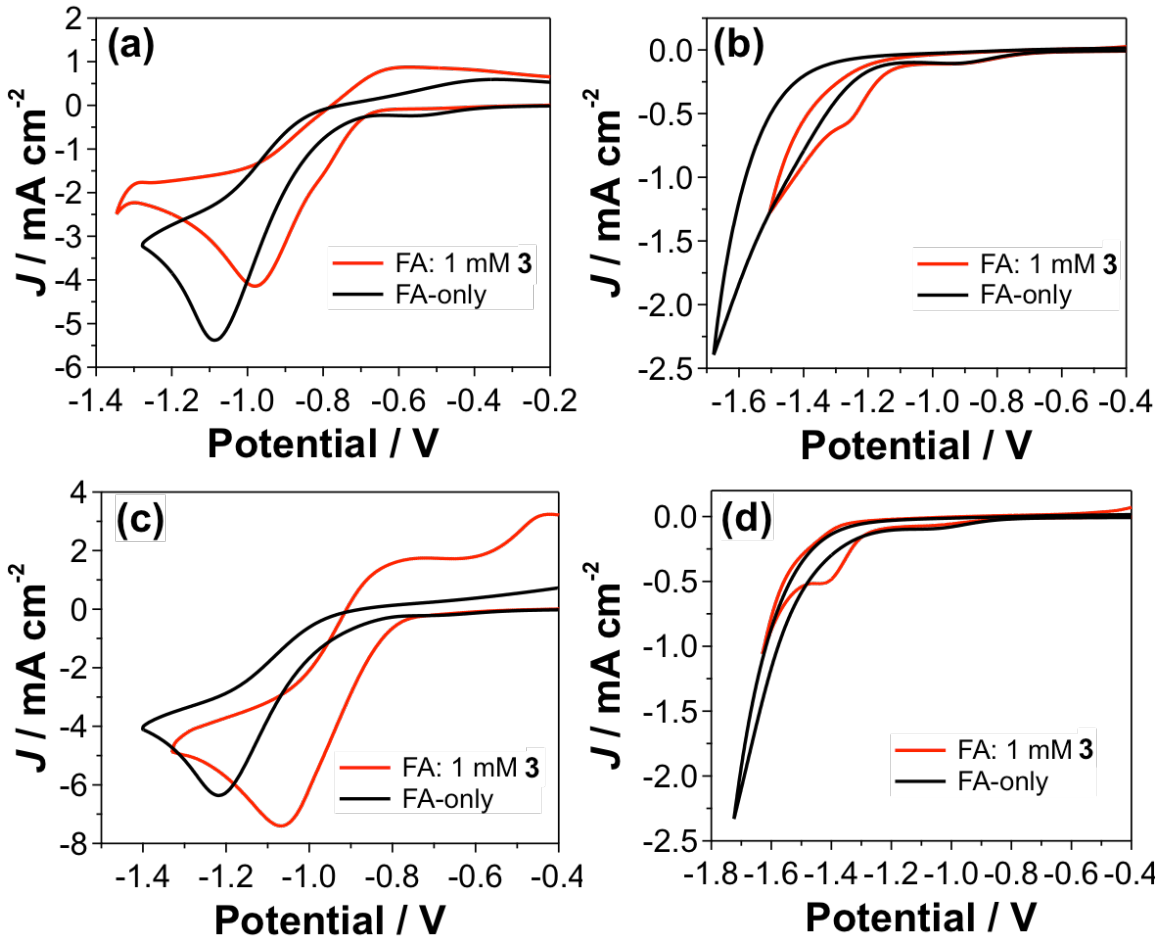

Figure 3.2. CV comparison of 10 mM HCOOH (FA) with and without 1 mM **3** added at (a) Pt and (b) RVC disc electrodes in 60% (v:v) H_2O/CH_3CN; and (c) Pt and (d) RVC disc electrodes in 10% (v:v) H_2O/CH_3CN. Scan rate 100 mV s^{-1}; 0.1 M $LiClO_4$; Potential vs. $FcH^{0/+}$.

To determine if the reduction process observed for HCOOH was somehow catalyzed by the presence of **3**, a CV titration was conducted, shown in Figure 3.3. As the HCOOH content was increased, an increase in the current is observed, with the disappearance of the reduction peak associated with the **3**/**[3-H]**$^+$ redox couple at both RVC and Pt surfaces, regardless of the solvent mixture employed. No current saturation was observed, indicating that no catalytic reaction was occurring.[64b] Rather, the CV titration indicates that there exists two competing reductive mechanisms, namely the reduction of **[3-H]**$^+$, and the reduction of HCOOH directly. As shown, the current

becomes dominated by the direct reduction of HCOOH at large excesses of HCOOH, with the reduction of the $[ANH\text{-}H]^+$ becoming a background process.

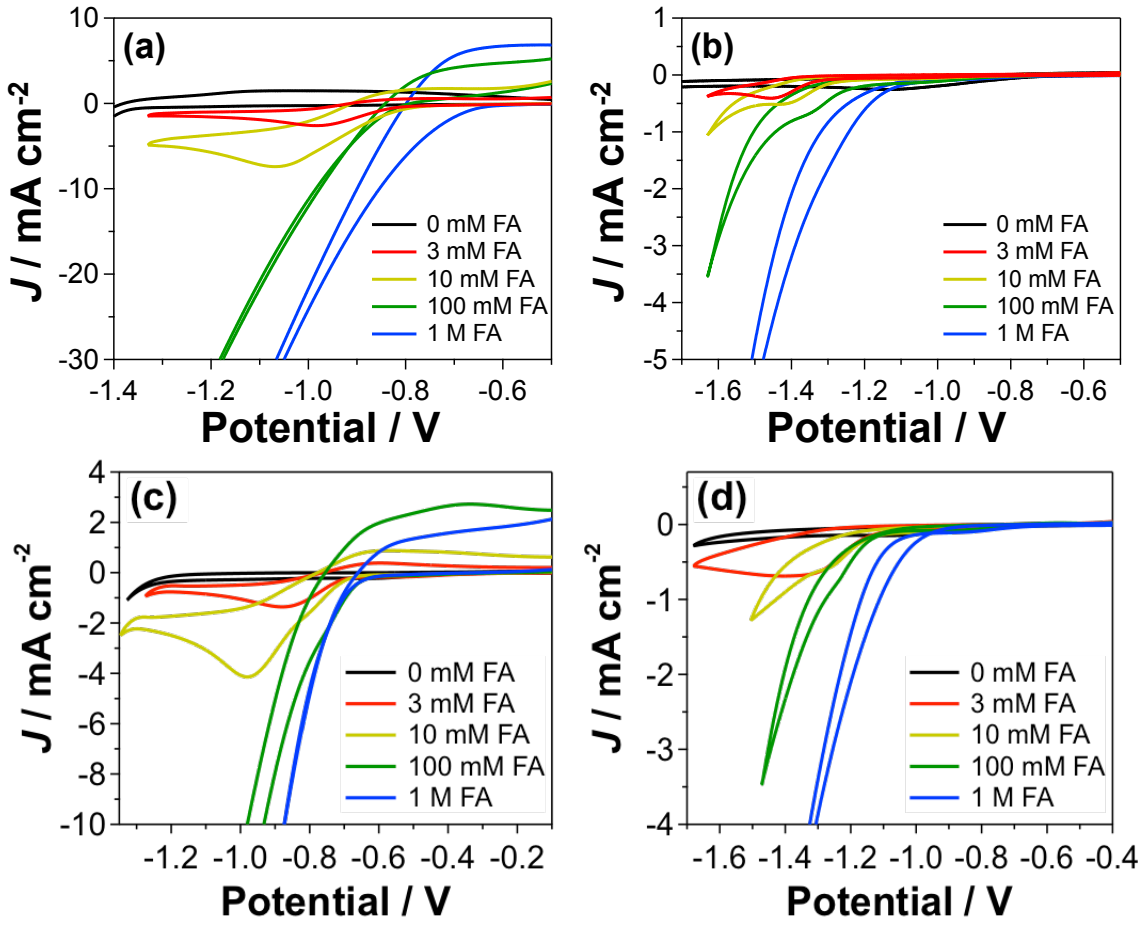

Figure 3.3. CVs of 1 mM **3** in the presence of 3, 10, 100, 1000 equivalents of HCOOH (FA) at (a) Pt and (b) RVC disc electrodes at 100 mV s^{-1}. 10% (v:v) H_2O/CH_3CN. CVs of 1 mM **3** in the presence of 3, 10, 100, 1000 equivalents of HCOOH (FA) at (c) Pt and (d) RVC disc electrodes at 100 mV s^{-1}. 60% (v:v) H_2O/CH_3CN. 0.1 M $LiClO_4$; Potential vs. $FcH^{0/+}$.

To confirm the identity of the HCOOH reduction observed as a 'weak acid' reduction, a CV study was conducted with acetic acid (AA, Figure 3.4), which is a weaker acid (pK_a of 4.75) than formic acid (pK_a of 3.75). As with HCOOH, an irreversible wave is observed at Pt surfaces with AA alone, with an anodic shift in the reductive wave upon addition of **3** to the solution. At RVC, the introduction of **3** results in a peak at ~ -1.2 V, as observed with HCOOH solutions. All of the peaks observed

using **3** in AA are shifted cathodically by ~70 mV from the peaks observed under HCOOH, consistent with the fact that a weaker acid has been used (59 mV shift per unit pH/pK_a). A pre-wave feature is observed in AA solutions when **3** is introduced at RVC surfaces (~ -1 V), and is attributed to a weak-adsorption process of **3** at the electrode surface under the conditions used, similar to work investigating the pyridinium redox couple at Pt surfaces.[51] Comparison of the relative current densities of AA-containing and HCOOH-containing solutions indicates that no catalytic event is observed on the CV timescale with HCOOH under the applied conditions, with both solutions passing similar amounts of current. Thus, on the CV timescale, **3** in the presence of HCOOH and AA is undergoing a 'weak acid' process at Pt and RVC surfaces.

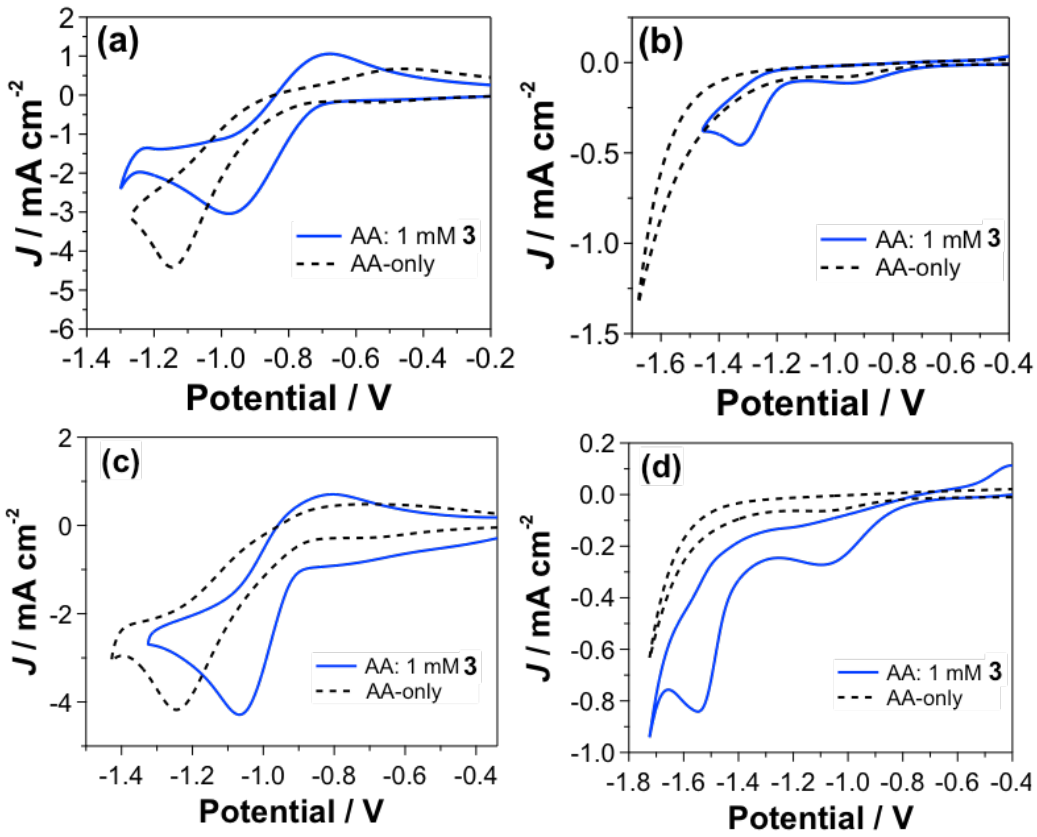

Figure 3.4. CV comparison of 10 mM AA with and without 1 mM **3** added at (a) Pt and (b) RVC disc electrodes in 60% (v:v) H_2O/CH_3CN; and (c) Pt and (d) RVC disc electrodes in 10% (v:v) H_2O/CH_3CN. Scan rate 100 mV s^{-1}; 0.1 M $LiClO_4$; Potential vs. $FcH^{0/+}$.

3.3.2 Bulk Electrolysis Results

Potentiostatic electrolyses of **3** in HCOOH-containing solutions were conducted to determine if DHP formation and/or methanol production could be observed. The initial $E_{applied}$, charge passed, and the mixed aqueous/organic solvent system were chosen based on the results of Chapter 2, with the conditions attempted summarized below (Table 3.1).[67] ^{1}H NMR analysis of aliquots of electrolysis reaction mixtures of **3** in 60% (v:v) H_2O/CH_3CN and 10 equivalents of HCOOH revealed near complete formation of a DHP-type species at both Pt and RVC electrodes (Entries 5 and 10 in Table 3.1, Figure 3.5). Full identification of the reduced ANH species in aliquots of the electrolyzed solutions by ^{1}H NMR was precluded by the presence of a large water peak in the region corresponding to the NH and CH_2 peaks of **3-H$_2$**. Thus, initial screens looking for DHPs in electrolyzed solutions compare just the peaks that can be observed in similar solvent mixtures containing pre-formed **3-H$_2$** (see Chapter 2, Figure 2.13, Figure 3.17). Furthermore, the water peak was also found to overlap with the methanol peak in 10% water mixtures in acetonitrile, and thus methanol content could not be observed via ^{1}H NMR. No decomposition products of **3** under the reducing conditions employed were observed in solutions electrolyzed at both RVC and Pt surfaces, indicating that any methanol production, as in Chapter 2, will be the result of formic acid reduction under the conditions employed.

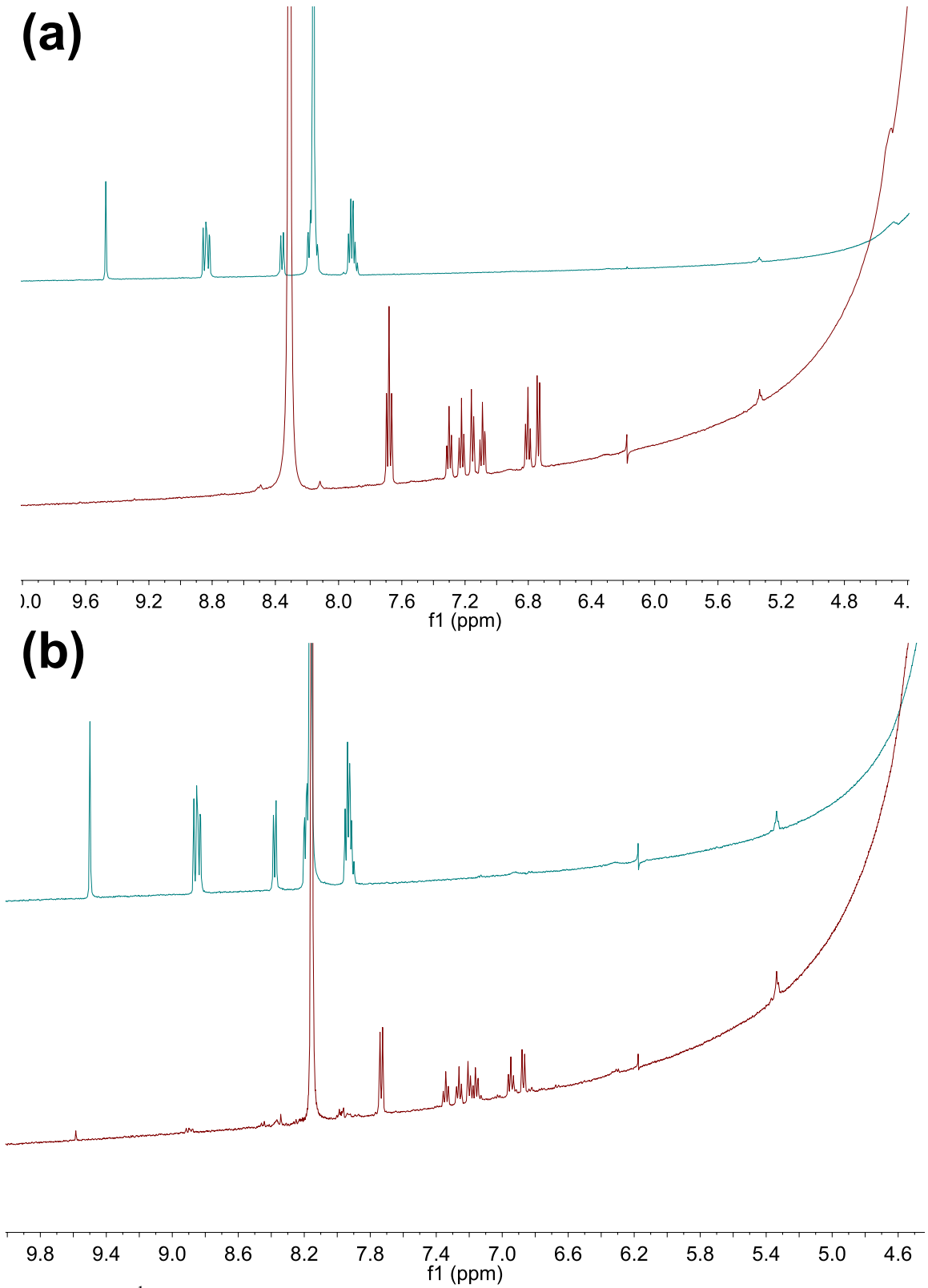

Figure 3.5. ^{1}H NMR before (blue, top) and after (red, bottom) bulk electrolysis for 1 mM **3**: 10 mM HCOOH in 60% (v:v) H_2O/CH_3CN at (a) Pt mesh electrode and (b) RVC mesh electrode; $E_{applied}$ = -1.23 V vs. $FcH^{0/+}$.

Table 3.1. Electrochemical generation of **3-H$_2$** and methanol from electrolysis of HCOOH-containing solutions of **3**.

Entry	3:HCOOH[a]	$E_{applied}$[b]	Solvent[c]	3-H$_2$ (%)[d]	%FE[e] 3-H$_2$	[CH$_3$OH][f]	%FE[g] CH$_3$OH	pH[h]
1	1:10	-1.23 (Pt)	10%	43(5)	3.2(0.6)	35(1)	0.55(0.11)	3.76
2	1:100	-1.23 (Pt)	10%	49(11)	2.6(0.6)	30(3)	0.34(0.03)	3.23
3	1:1000	-1.23 (Pt)	10%	80(1)	3.5(0.6)	73(7)	0.63(0.04)	2.05
4	1:100	-1.23 (Pt)	CH$_3$CN	93(5)	10(4)	ND, 18	-, 0.24	-
5	1:10	-1.23 (Pt)	60%	99(1)	5.4(0.1)	28(1)	0.31(0.01)	3.22
6	1:10	-0.83 (Pt)	10%	5(2)	5.2(1.5)	ND	-	3.76
7	1:10	-0.83 (Pt)	60%	36(10)	19(6)	23(5)	2.1(1.1)	3.22
8	1:10	-1.23 (RVC)	10%	35(10)	21(8)	27(2)	3.2, 3.2	3.76
9	1:10	-1.43 (RVC)	10%	86(8)	40(1)	28(12)	2.8(1.4)	3.76
10	1:10	-1.23 (RVC)	60%	95(2)	56(24)	31(2)	3.6(1.5)	3.22
11	1:100	-1.23 (RVC)	10%	90(2)	18.2(3)	29(11)	1.1(0.2)	3.23
12	1:1000	-1.23 (RVC)	10%	87(7)	6.0(0.7)	76(25)	1.2(0.6)	2.05
13	1:100	-1.23 (RVC)	CH$_3$CN	75(5)	16(5)	27(13)	1.0(0.01)	-
14	10:100	-1.23 (Pt)	10%	19	1.2	31	0.4	3.55
15	1:100	-1.23 (Pt)	10%; CO_2-atm	76	4.4	47	0.5	3.26

[a] in mM. [b] in V vs. $FcH^{0/+}$; RVC = reticulated vitreous carbon (glassy carbon). [c] % (v:v) H_2O/CH_3CN. [d] % conversion as determined by ^{1}H NMR analysis of aliquots from post-electrolysis reaction mixtures. Shown with the standard deviation. [e] Faradaic Efficiency of DHP formation. Shown with the standard deviation. [f] in μM as determined by GC-FID analysis. Shown with the standard deviation. [g] Faradaic Efficiency of Methanol formation. Shown with the standard deviation. [h] pH of solution pre-electrolysis

Reducing the proportion of water in CH_3CN to 10% but otherwise maintaining identical conditions led to a decrease in conversion of **3** to **3-H$_2$** (Entries 1 and 8, Table 3.1). The total charge passed at Pt and RVC electrodes remained unchanged, however, suggesting that water may help stabilize DHP formation but also suppress further reactivity (Figure 3.6). The charge passed in solutions of 10% H_2O, however, was found

to level off over the timescale investigated (~10 000 s), while the solutions in 60% H_2O were still found to pass charge at the same rate (CPE plots in Figure 3.6). This can be explained by the relative water content, where an increase in water content is expected to reduce the overpotential necessary for proton reduction, and thus facilitate easier proton reduction, as observed by CV (Figure 3.2-3).[66] In contrast, when the same process is conducted in dry CH_3CN, near complete formation of the DHP can be observed at both RVC and Pt surfaces, but requires higher concentration of HCOOH for full conversion (100 equivalents; entries 4 and 13). The charge passed was also found to saturate in a similar fashion as that observed at Pt surfaces in 10% H_2O, indicating that other reductive processes (e.g., H_2 evolution) may be shut down through a similar mechanism. Analysis of the charge passed in dry CH_3CN at Pt surfaces indicates that only ca. 30-40% of the acid source is consumed during the electrolysis experiment and the lower reactivity may be due to an increase in overpotential associated with a decrease in the available protons in a non-aqueous environment.

The conversion of **3** to **3-H$_2$** at Pt surfaces measured by ^{1}H NMR spectroscopy was found to increase with increased concentrations of HCOOH (entries 1-3) and increased applied potential (entries 1, 5-7). Increasing the HCOOH content increases the concentration of available protons for DHP formation and lowers the pH of the solution, reducing the prominence of any energy barriers towards surface-hydride formation (weak acid reduction). Similarly, by increasing the applied potential, any activation barrier towards DHP formation is overcome, which may not necessarily be coupled to a 'weak-acid' reduction mechanism. The majority of the %FEs for DHP formation at Pt surfaces,

however, are low (<10%) likely due to the increased relevance of proton reduction under the conditions applied.

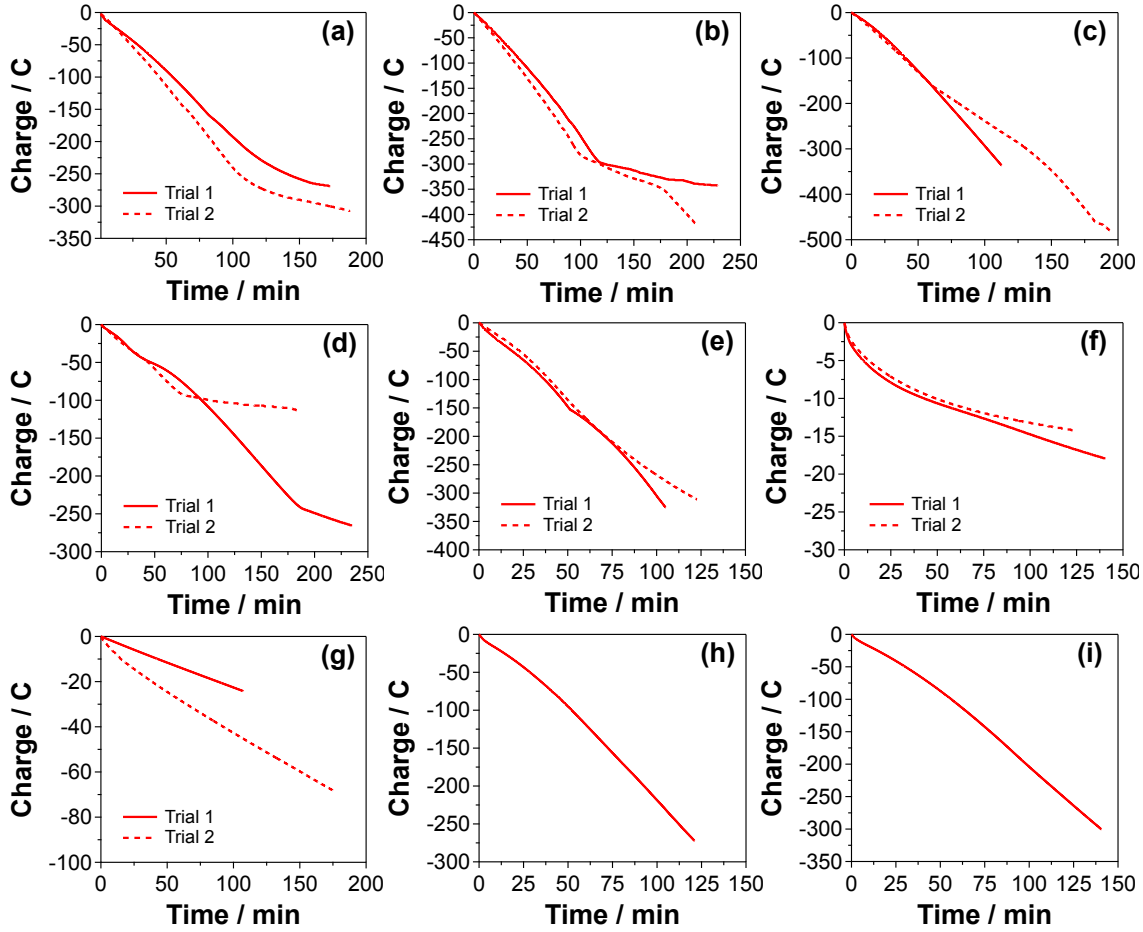

Figure 3.6. CPE plots for (a) 1 mM **3**: 10 mM HCOOH (b) 1 mM **3**: 100 mM HCOOH (c) 1 mM **3**: 1000 mM HCOOH in 10% (v:v) H_2O/CH_3CN (d) 1 mM **3**: 100 mM HCOOH in CH_3CN (e) 1 mM **3**: 10 mM HCOOH in 60% (v:v) H_2O/CH_3CN with $E_{applied}$ = -1.23 V vs. $FcH^{0/+}$; (f) 1 mM **3**: 10 mM HCOOH in 10% (v:v) H_2O/CH_3CN (g) 1 mM **3**: 10 mM HCOOH in 60% (v:v) H_2O/CH_3CN, $E_{applied}$ = -0.83 V vs. $FcH^{0/+}$; (h) 10 mM **3**: 100 mM HCOOH, (i) 1 mM **3**: 100 mM HCOOH with CO_2 (1 atm), in 10% (v:v) H_2O/CH_3CN, $E_{applied}$ = -1.23 V vs. $FcH^{0/+}$. 0.1 M $LiClO_4$; Pt mesh electrode.

Unlike at Pt surfaces, a significant reduction in the charge passed is observed at RVC surfaces (Figure 3.7), with charge passed at a constant rate except at high potentials (Figure 3.7f). The decrease in the charge passed moving from Pt to RVC is attributed to

the decrease in the proclivity of RVC towards proton reduction, which dominates the current response at Pt surfaces (see CPEs and CVs above).[75] When the concentration of HCOOH is increased significantly, however, proton reduction becomes more prominent even at RVC surfaces, similar to the response observed in the CVs above.

The use of a more inert electrode towards proton reduction such as RVC is expected to increase the contributions of alternative processes such as DHP formation and methanol formation to the charge passed. This is observed when investigating the %FE for DHP formation, where a significant increase is observed moving from Pt to RVC surfaces (~5 %FE → ~20 %FE). While no significant change in DHP formation was observed (all entries but entry 8 were >75% DHP formation), the highest %FE was observed at low acid loadings (56 %FE). This observation is again consistent with the increased prominence of acid reduction as the acid loading is increased, as observed by CV titration. However, the charge passed is not strictly associated with DHP formation, even at these low acid loadings (only ~30% of the charge is accounted for), and thus other processes such as proton reduction and methanol formation are also likely occurring.

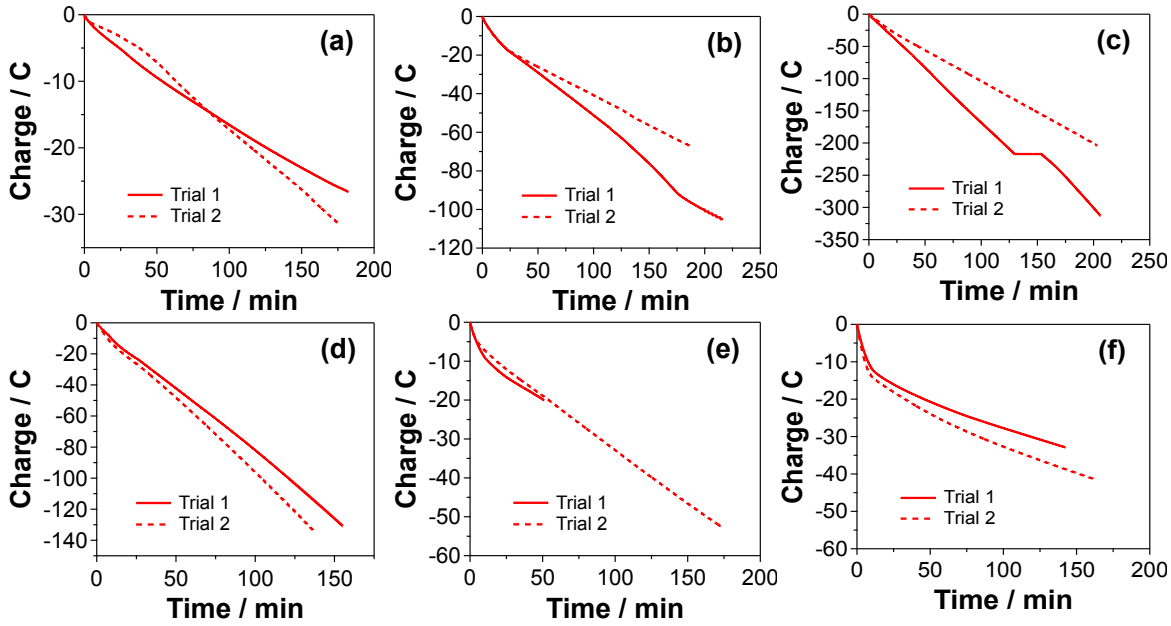

Figure 3.7. CPE plots for (a) 1 mM **3**: 10 mM HCOOH (b) 1 mM **3**: 100 mM HCOOH (c) 1 mM **3**: 1000 mM HCOOH in 10% (v:v) H_2O/CH_3CN; (d) 1 mM **3**: 100 mM HCOOH in CH_3CN; (e) 1 mM **3**: 10 mM HCOOH in 60% (v:v) H_2O/CH_3CN with $E_{applied}$ = -1.23 V vs. $FcH^{0/+}$; and (f) 1 mM **3**: 10 mM HCOOH in 10% (v:v) H_2O/CH_3CN with $E_{applied}$ = -1.43 V vs. $FcH^{0/+}$. 0.1 M $LiClO_4$; RVC mesh electrode.

While the aromatic region of ^{1}H NMR spectra of aliquots of the electrolyzed solutions are consistent with formation of **3-H$_2$**, and consumption of **3**, resonances for the NH and CH_2 groups of **3-H$_2$** could not be observed. As such, we sought to isolate **3-H$_2$** generated by electrolysis at a Pt electrode and examine the product using ^{1}H NMR, ^{13}C NMR, HSQC-DEPT and UV-Vis spectroscopy to confirm its identity. Isolation of electrochemically-generated **3-H$_2$** from the electrolyzed solution (10 mM HCOOH used) gave a yellow-orange solid in 91% isolated yield after a dichloromethane extraction. Comparison of ^{1}H NMR and ^{13}C NMR spectra collected for the electrolyzed product with those of both **3** and **3-H$_2$** reveals that the isolated species contains both **3** and **3-H$_2$** (Figures 3.8 and 3.9). The NMR conversion of **3** to **3-H$_2$** was determined through comparison of the integral for the singlet associated with **3** at ~9.5 ppm, to the integral of the doublet associated with **3-H$_2$** at ~6.7 ppm in the ^{1}H NMR, indicating that **3-H$_2$** was

generated at 89% conversion. Two singlet resonances assigned to the CH_2 group and the NH group of **3-H₂** are also observed (3.8 and 4.3 ppm). A slight shift in the NH and the peaks corresponding to **3** is observed in the electrolyzed product due to the presence of a large amount of acetonitrile in solution, altering the H-bonding environment of the NH proton.[86] Comparing the $^{13}C\{^1H\}$ NMR spectra reveals that the dihydro-species generated electrochemically contains peaks with identical chemical shifts as those of the chemically synthesized **3-H₂**, with smaller peaks corresponding to the presence of the ANH and residual dichloromethane and acetonitrile solvent peaks.

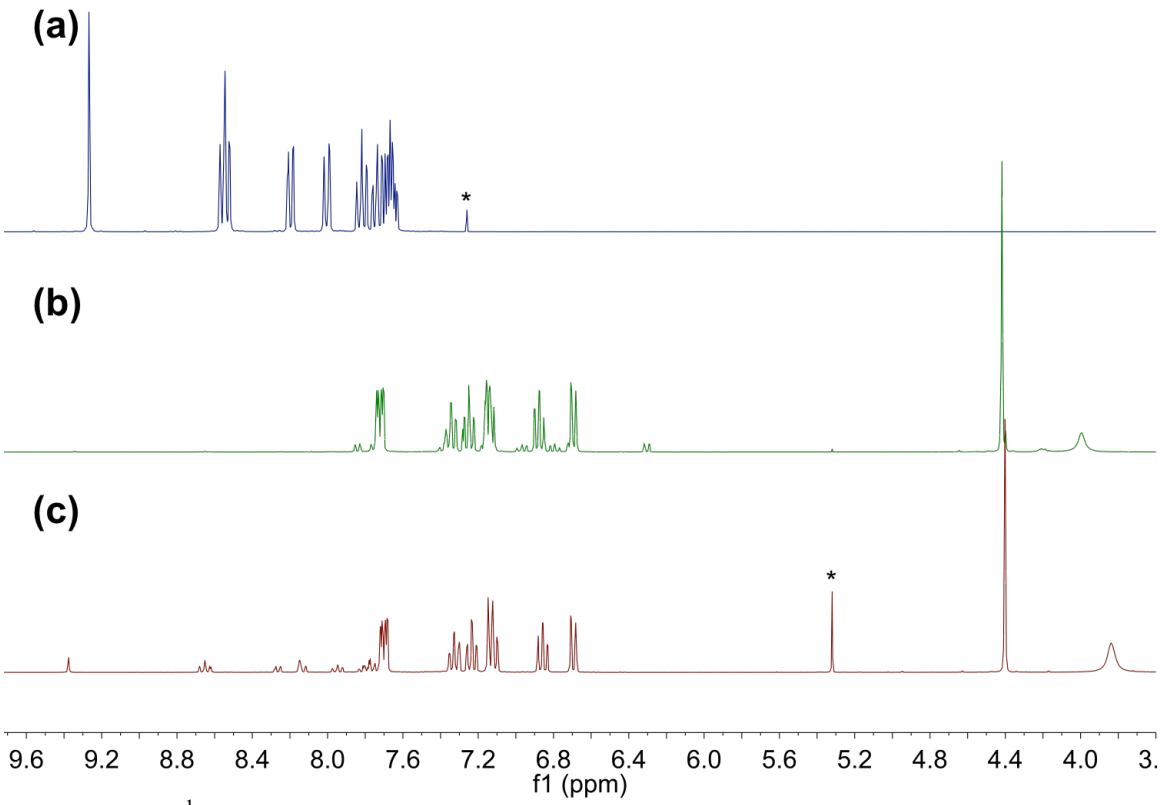

Figure 3.8. ^1H NMR ($CDCl_3$) Comparison of (a) **3** (blue) (b) **3-H₂** (green) (c) electrochemically-generated **3-H₂** (red). Residual solvent peaks indicated.

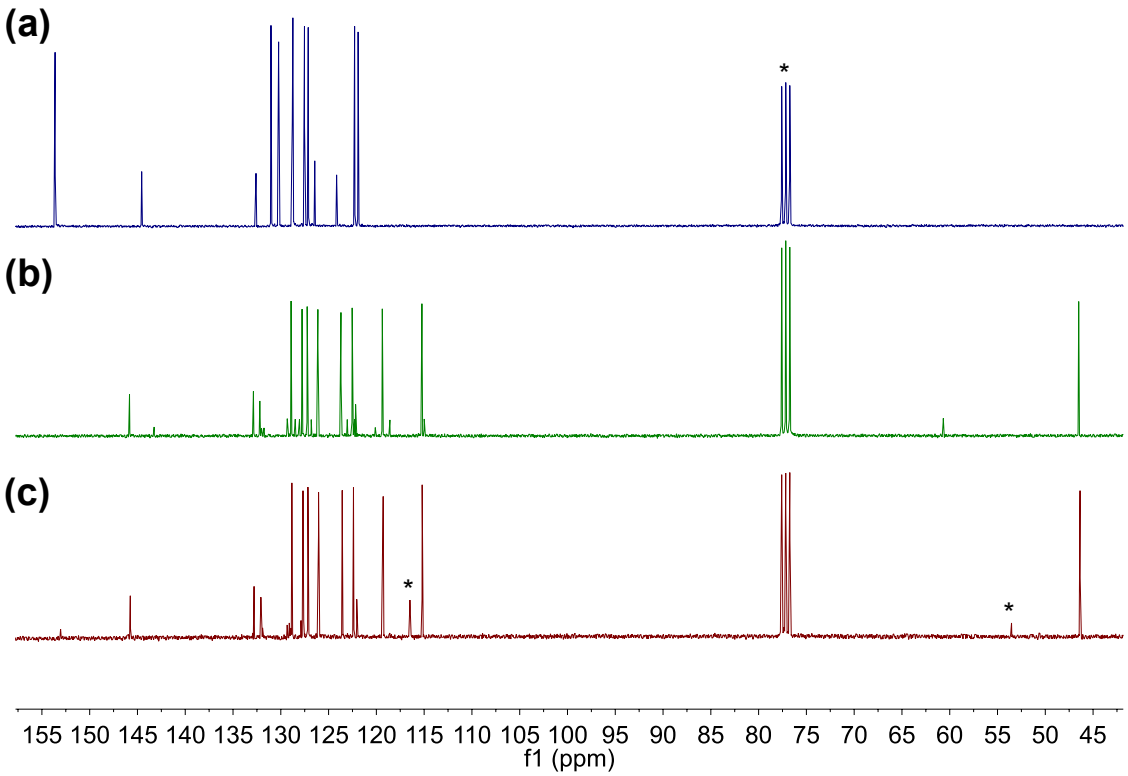

Figure 3.9. Comparison of $^{13}C\{^{1}H\}$ NMR spectra of ($CDCl_3$) (a) **3** (blue) (b) **3-H$_2$** (green) (c) electrochemically-generated **3-H$_2$** (red). Residual solvents indicated.

Further confirmation of the identity of the species was conducted using HSQC-DEPT, where any carbon atom attached to a proton(s) can be determined. The addition of a DEPT sequence also allows for the distinction of CH_3 and CH peaks from CH_2 peaks based on the phasing of the resulting signal (CH, CH_3 groups red, CH_2 groups blue in the spectra shown). As shown in Figure 3.10, a CH_2 group is observed (blue peak), and eight aromatic CH peaks are observed, with peak alignments corresponding to **3-H$_2$** (see Appendix, Figures A7 and A8 for spectra of **3** and chemically synthesized **3-H$_2$**). Further comparison of the $^{13}C\{^{1}H\}$ NMR and the HSQC-DEPT data reveals four quaternary carbon peaks in the $^{13}C\{^{1}H\}$ NMR (no protons attached) at identical chemical shifts as for chemically synthesized **3-H$_2$**, further confirmation of the identity of the species in solution as majority **3-H$_2$**.

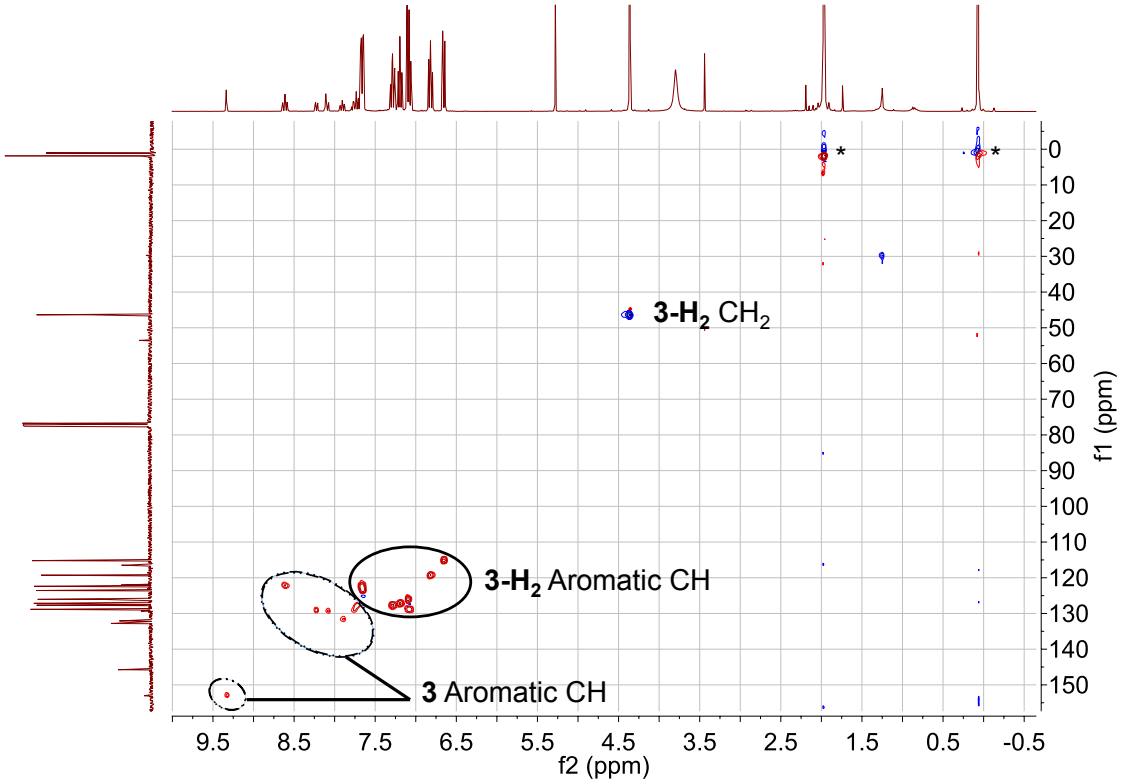

Figure 3.10. HSQC-DEPT of electrochemically-generated **3-H$_2$**. Residual solvent and grease peaks denoted by asterisk. $^{13}C\{^1H\}$ NMR shown on left axis, ^1H NMR shown on top axis.

UV-Vis absorption spectroscopy was also conducted to compare electrochemically generated **3-H$_2$** with the chemically synthesized control and **3**, based on its absorption profile in CH_3CN. As shown in Figure 3.11, the absorption spectra of the electrochemically generated **3-H$_2$** overlays with that of the chemically synthesized DHP, exhibiting absorption maxima at 345 nm, 267 nm, 245 nm and 195 nm. In contrast, **3** exhibits absorption maxima at 315 nm, 250 nm, 209 nm, and a broad absorption at 350 nm. To ensure accurate comparisons and to account for any dilution factors, the absorption profiles were normalized to the absorption peaks at 240 nm. Thus, based on the NMR and UV-Vis techniques utilized, the DHP **3-H$_2$** is electrochemically generated

in solution without any secondary aromatic products generated, with minor decomposition to the parent ANH.

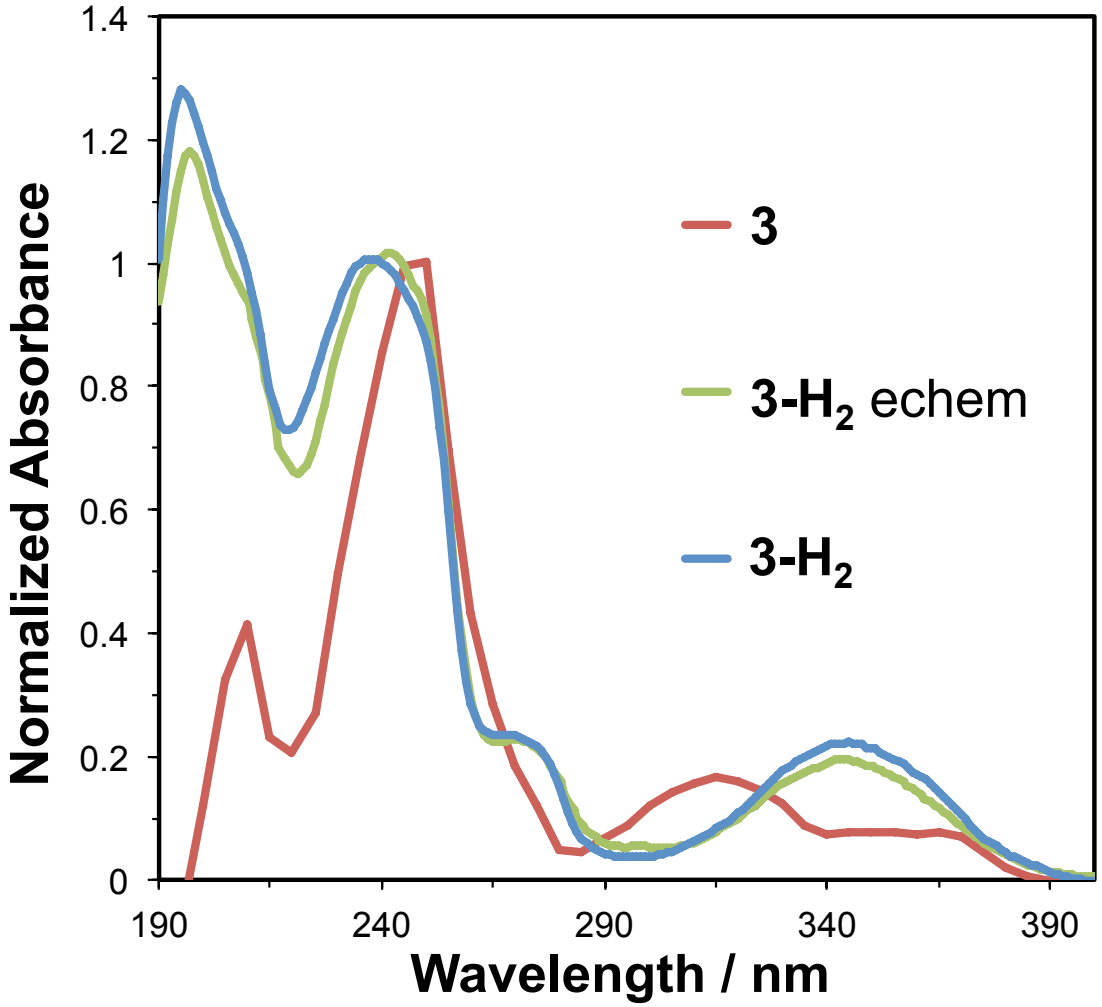

Figure 3.11. UV-Vis Spectra of **3** (red); **3-H$_2$** (blue); and electrochemically generated **3-H$_2$** (green). Spectra are normalized to their respective absorbance peak at 240-245 nm to allow for accurate comparison.

Methanol production (GC-FID plots in Figure 3.12-3.13) was determined through GC-FID on desalted bulk electrolysis solutions, following the same bulb-to-bulb procedure as utilized in Chapter 2 (Section 2.2.5).[67] Determination of methanol concentration in solutions was conducted using an external standard calibration curve (see Appendix, Figure A9), with the peak area determined using a linear baseline

correction. Small amounts of methanol (10-100 μM) were consistently observed, with low %FEs and TONs (0.015-0.1) in the same range as the direct electrochemical reduction of CO_2 using **3** (~10% FE for methanol production, see Chapter 2, Table 2.3), and **1**.[47, 67] No background methanol production was observed in the absence of ANH at Pt or RVC surfaces (see Appendix, Figure A9), indicating that the ANH is needed for methanol production from formic acid to occur. This represents the first tandem observation of an isolable DHP forming in a solution alongside methanol during electrochemical reduction of a key postulated intermediate, HCOOH, in electrochemical CO_2 reduction in the presence of ANH additives.

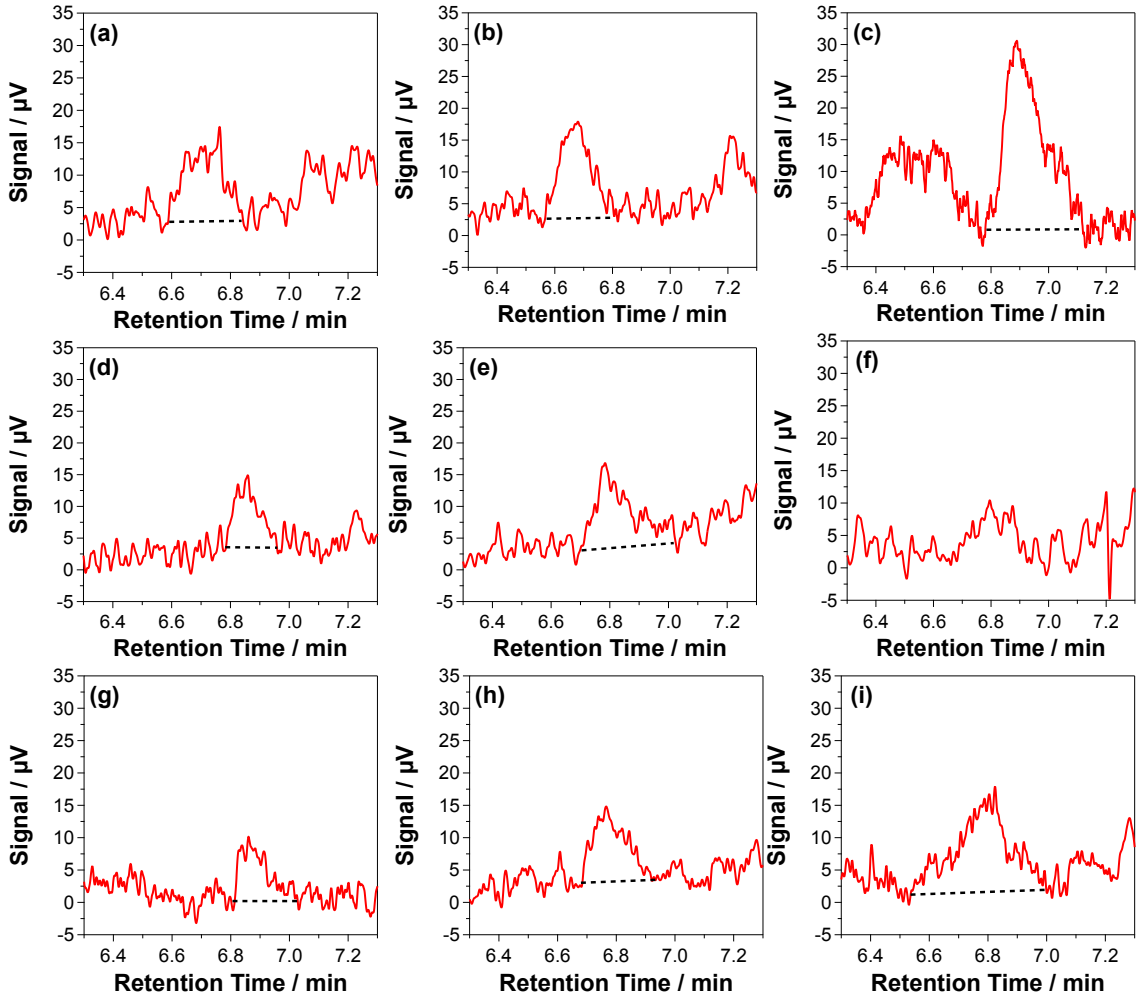

Figure 3.12. GC-FID chromatograms of bulk electrolysis samples at Pt mesh electrodes for (a) 1 mM **3**: 10 mM HCOOH (b) 1 mM **3**: 100 mM HCOOH (c) 1 mM **3**: 1000 mM HCOOH in 10% (v:v) H_2O/CH_3CN (d) 1 mM **3**: 100 mM HCOOH in CH_3CN (e) 1 mM **3**: 10 mM HCOOH in 60% (v:v) H_2O/CH_3CN with $E_{applied}$ = -1.23 V vs. $FcH^{0/+}$; (f) 1 mM **1**: 10 mM HCOOH in 10% (v:v) H_2O/CH_3CN (g) 1 mM **1**: 10 mM HCOOH in 60% (v:v) H_2O/CH_3CN, $E_{applied}$ = -0.83 V vs. $FcH^{0/+}$; (h) 10 mM **1**: 100 mM HCOOH, (i) 1 mM **3**: 100 mM HCOOH with CO_2 (1 atm), in 10% (v:v) H_2O/CH_3CN, $E_{applied}$ = -1.23 V vs. $FcH^{0/+}$. Dashed line indicates baseline used for peak integration.

Increasing the ratio of HCOOH to **3** has a moderate impact on the absolute amount of methanol observed (compare entries 1 and 3, 11 and 12, Table 3.1, Figure 3.12a,c; 3.13a,c), while increasing the concentration of **3** and HCOOH but keeping the ratio constant had a negligible effect on methanol production (compare entries 1 and 14, Figure 3.12a,h). This implies that overall HCOOH content does impact methanol

formation, while the ANH concentration does not significantly affect methanol generation at the concentrations investigated. Previous work investigating the reduction of CO_2 in the presence of pyridine found that increased pyridine concentrations resulted in poisoning of the electrode surface, resulting in a decrease in methanol generation.[79] As the concentration of methanol generated in this work was found to stay relatively constant upon increasing the ANH concentration (entry 2, 14 in Table 3.1), and as no surface deposits were observed on the Pt surfaces, electrode poisoning by deposition of **3** is unlikely under the conditions investigated in this work.

Addition of CO_2 (1 atm) to the solution was attempted to determine if there existed any stabilizing effect or enhancement in methanol generation due to the presence of a H_2CO_3/HCO_3^- buffer in solution. However, no enhancement towards methanol production from HCOOH was observed (entry 15, Table 3.1; Figure 3.12i), and no increase in the %FE towards methanol production. This result suggests that the HCOOH reduction event is independent of the CO_2 reduction event, and given the TON and %FE observed, is likely the limiting step towards CO_2 reduction to methanol provided HCOOH is a reaction pathway intermediate.

We next examined the dependence of conversion to **3-H$_2$** and methanol production on the potential applied. At Pt surfaces, methanol production and DHP formation were both suppressed when the potential was decreased to -0.83 V in solutions containing 10% water in CH_3CN (entry 6), while at higher water concentrations (60% H_2O in CH_3CN, entry 7) both species could again be observed. This result can be explained through observation of the CVs of **3** in HCOOH (Figures 3.2-3.3), where a 150 mV cathodic shift in the reduction event is observed moving from 60% to 10% H_2O

mixtures. Similar studies investigating the reduction of CO_2 in the presence of pyridine also have indicated a minimum potential for methanol production, where the necessary applied potential corresponded to undergoing a 'weak acid' reduction mechanism.[43a, 47, 67] As such, the reduction of HCOOH to methanol and DHP formation require an applied potential that corresponds to 'weak acid' reduction and the formation of a surface hydride, as observed on the CV timescale.

RVC surfaces were used to determine the dependence of methanol generation and its corresponding %FE on the electrode surface used. Results from CO_2 reduction in Chapter 2 suggest that the reduction process to methanol is less efficient at RVC surfaces, and is attributed to the inertness of RVC surfaces when compared to Pt surfaces. Experimental and computational studies of glassy carbon electrodes indicate that a large overpotential exists towards proton reduction in comparison to Pt surfaces.[46, 75] As shown in Table 3.1 and Figure 3.13, the methanol generated from HCOOH is equivalent to the amount generated at Pt surfaces. Furthermore, the %FE towards both DHP and methanol generation is higher at RVC surfaces, indicating that the contribution of the proton reduction pathway to the observed current passed is reduced under the conditions employed.

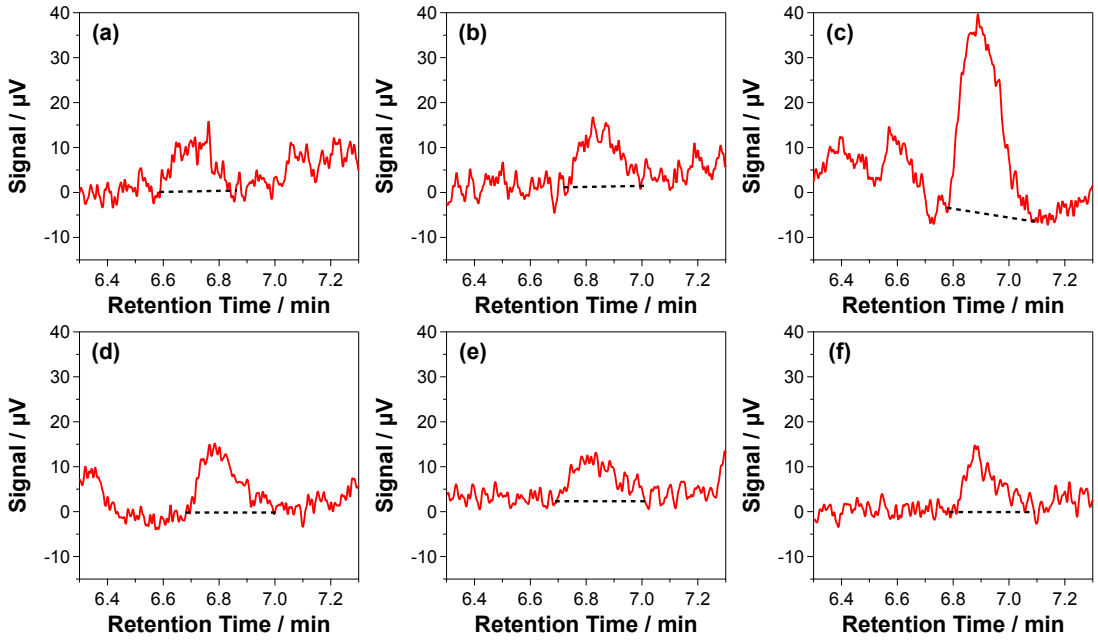

Figure 3.13. GC-FID Chromatograms of bulk electrolysis samples run at RVC mesh electrodes for (a) 1 mM **3**: 10 mM HCOOH (b) 1 mM **3**: 100 mM HCOOH (c) 1 mM **3**: 1000 mM HCOOH in 10% (v:v) H_2O/CH_3CN; (d) 1 mM **3**: 100 mM HCOOH in CH_3CN with $E_{applied}$ = -1.23 V vs. $FcH^{0/+}$; (e) 1 mM **3**: 10 mM HCOOH in 10% (v:v) H_2O/CH_3CN with $E_{applied}$ = -1.43 V vs. $FcH^{0/+}$; and (f) 1 mM **3**: 10 mM HCOOH in 60% (v:v) H_2O/CH_3CN with $E_{applied}$ = -1.23 V vs. $FcH^{0/+}$. Dashed line indicates baseline used for peak integration.

In the absence of **3**, no methanol formation was observed at RVC and Pt electrodes (see Appendix, Figure A9), indicating that the presence of **3** is necessary for methanol production. To determine the total contribution of acid reduction towards the charge passed, the CPE plots of blank solutions are compared to CPE plots of solutions with **3** present under the same conditions (Figure 3.14). At RVC surfaces, a 30% increase is observed in the charge passed upon introduction of **3** for the same time frame. This 30% increase matches with the %FE of DHP and methanol generation, indicating that the remaining 70% of the charge is diverted to other reactivity such as proton reduction. This is not the case at Pt surfaces, where DHP formation and methanol formation account for only a fraction of the charge passed (~ 4 %FE). The additional charge passed can be understood when looking at the CVs in Figure 3.2, where a large anodic shift (100-200

mV) in the $E_{1/2}$ of the reductive process associated with proton reduction occurs when **3** is added into a solution of HCOOH, unlike at RVC surfaces. Furthermore, when a CV titration of **3** was conducted with HCOOH at Pt and RVC surfaces, a significant increase in the current passed is observed with HCOOH addition, where proton reduction dominates the current response past 100 mM HCOOH in the presence of 1 mM **3** at Pt surfaces, and at 1 M HCOOH for RVC surfaces (Figure 3.3). Thus, while more charge is being passed in the presence **3** at Pt surfaces, the majority of the charge is still attributed to proton reduction and charge compensations, with proton reduction playing a significantly larger role at Pt surfaces than at RVC surfaces at low HCOOH concentrations.

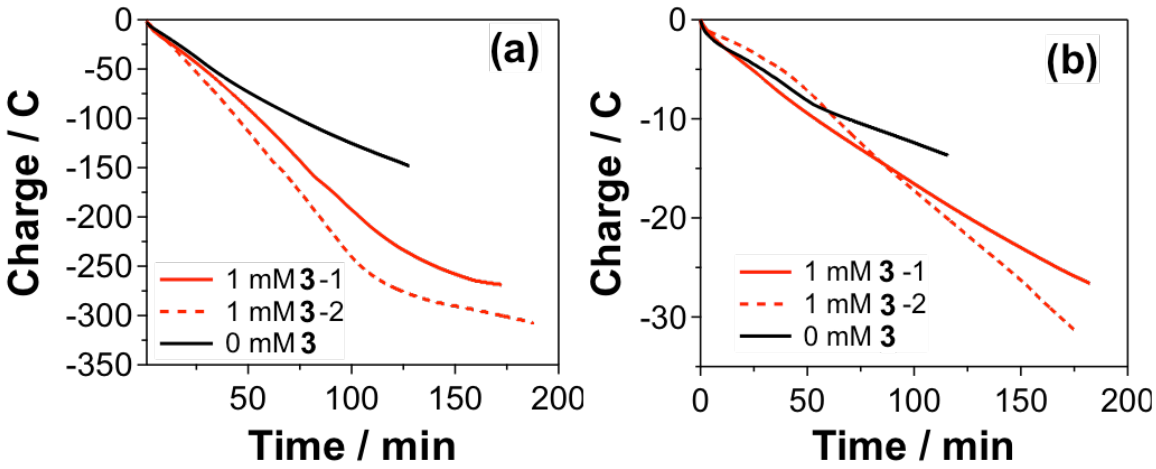

Figure 3.14. CPE plots for 10 mM HCOOH at (a) Pt and (b) RVC mesh electrodes in the presence of 1 mM **3** (red traces) and without (black traces). $E_{applied}$ = -1.23 V vs. $FcH^{0/+}$; 0.1 M $LiClO_4$; 10% (v:v) H_2O/CH_3CN.

Curious as to the effect of Brønsted acidity on DHP formation, $HClO_4$ and acetic acid (AA) were also used as a proton source, with acetic acid having a slightly larger reported pK_a (4.75) than formic acid (3.75) in water, and perchloric acid being a strong Brønsted acid in both water and acetonitrile. In Chapter 2, 0.2 equivalents of perchloric

acid was used (pH ~ 5) in an attempt to form **3-H$_2$** under CO_2 reducing conditions at Pt surfaces (Figure 2.13; -0.75 V vs. $FcH^{0/+}$). No DHP generation was observed under these conditions or under CO_2, and was attributed to the lack of excess protons relative to the ANH in solution. In this work, the ratio of acid to ANH in solution was instead increased to a minimum of three equivalents. As shown in Table 3.2, when the solvent mixture, electrode surface and applied potential are kept constant, the amount of DHP generated differs between AA and perchloric acid, with perchloric acid showing near full conversion to the DHP (entries 4 and 7, 5 and 6). However, when $E_{applied}$ is increased from -1.23 V to -1.43 V, near full conversion of **3** to **3-H$_2$** is observed in the presence of acetic acid regardless of the solvent system used (entries 2 and 3).

Comparing the pH of pre-electrolysis solutions, the pH of acetic acid-containing solutions are higher than under perchloric acid or formic acid conditions, and higher than the pK_a value determined for **3** in 10% H_2O (2.6, see Table 3.3), indicating that **[3-H]$^+$** is a minor species in solution (ca. one equivalent for every 200 equivalents of **3** in solution). The observed decrease in DHP formation at the same applied potential in the presence of acetic acid when compared to HCOOH is due to the shift in the $E_{1/2}$ associated with acid reduction at the CV timescale (Figures 3.2 and 3.4), where an overpotential is required to reduce the ANH to the DHP in the presence of a weaker acid. As such, the overpotential necessary for DHP formation is pH dependent, and thus dependent on the Brønsted acidity of the acids used. This observation indicates that DHP formation must be initially activated through a 'weak acid' reduction mechanism, where a surface hydride is required to help generate the DHP in solution.

Table 3.2. Electrochemical generation of **3-H$_2$** in the presence of different Brønsted acids.

Entry	[3][a]	[HA][b]	$E_{applied}$[c]	Electrode	Solvent[d]	pH[e]	3-H$_2$ (%)[f]	%FE 3-H$_2$[g]
1	1	3 (AA)	-1.23	RVC	CH_3CN	-	ND	0
2	1	3 (AA)	-1.43	RVC	CH_3CN	-	87	92
3	1	3 (AA)	-1.43	RVC	10%	4.70	95(1)	57(1)
4	1	3 (AA)	-1.23	RVC	60%	4.06	11	15
5	10	30 (AA)	-0.83	Pt	60%	4.15	2	5
6	10	30 ($HClO_4$)	-0.83	Pt	60%	1.55	17(4)	10(2)
7	1	3 ($HClO_4$)	-1.23	RVC	60%	2.54	98	39

[a] in mM. [b] in mM. [c] V vs. $FcH^{0/+}$. [d] % (v:v) H_2O/CH_3CN. [e] pH of solution pre-electrolysis. [f] % conversion as determined by ^{1}H NMR analysis of aliquots from post-electrolysis reaction mixtures. [g] Faradaic Efficiency of DHP formation.

The pH of CO_2 saturated solutions have been reported to be around pH ~ 5 in the presence of pyridine, with similar values determined in Chapter 2.[41, 43a, 47, 51, 67, 87] In this work, the pH of solutions containing three equivalents of perchloric acid or HCOOH are much lower (pH ~ 1-3), and as such cannot not offer a direct comparison to the acidic environment created under CO_2 and the possibility of DHP formation under CO_2 reducing conditions. Acetic acid, however, offers the ability to provide an excess of acid necessary for DHP formation while sustaining a pH ~ 4-5 in both 10% and 60% H_2O, thereby allowing a more direct comparison to CO_2-containing solutions. Reduction of **3** at Pt and RVC under CO_2-reducing potentials (-0.83 V at Pt; -1.23 V at RVC) in 60% H_2O resulted in low but observable amounts of **3-H$_2$** (Table 3.2). This is the first example of the generation of a DHP at a pH and applied potential relevant to CO_2 reduction. Previous work has observed the formation of a *dihydromercaptopteridine* under CO_2-reducing conditions,[60] but with methanol generation still under dispute (Figure 3.15).[61-62]

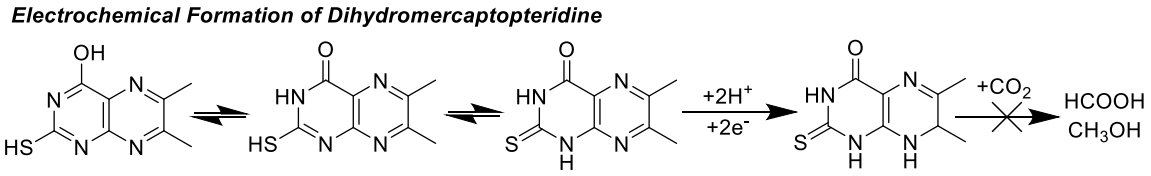

Figure 3.15. Tautomerization of mercaptopteridine followed by electrochemical formation of the dihydromercaptopteridine. Electrochemical CO_2 reduction to formic acid and methanol is still under dispute.[60-62]

Table 3.3. Experimentally determined pK_a values for phenanthridine (**3**), quinoline and pyridine in mixed CH_3CN/H_2O solvent systems.

ANH	pK_a in 60% (v:v) H_2O/CH_3CN[1]	pK_a in 10% (v:v) H_2O/CH_3CN
Phenanthridine (**3**)	3.6	2.6
Quinoline	4.0	2.9
Pyridine	4.5	3.3

[1]From Chapter 2.

By examining the reduction of a likely intermediate, HCOOH, in the reaction of CO_2 to methanol, it is expected that introduction of the DHP to the system would increase methanol production as fewer steps are required. However, when **3-H$_2$** is utilized instead of the parent ANH **3** under the same conditions for HCOOH reduction, methanol is still only observed in low amounts (Figures 3.16 and 3.17), with comparable methanol concentrations to those generated in the presence of the parent ANH (Table 3.4). The %FE at RVC surfaces was found to be higher, but still comparable to the %FE observed for ANH-based HCOOH reduction, with the %FE at Pt surfaces being comparable to the values obtained for ANH-based HCOOH reduction. Unlike in Chapter 2 where the %FE of the reduction of CO_2 to methanol was found to be electrode independent, the reduction of HCOOH to methanol by a DHP is electrode dependent. It is argued here that this is due to the lower pH of the solutions investigated (pH~3 compared to pH~5), resulting in a larger contribution of the charge passed to be associated with proton reduction rather than a reduction in the amount of methanol generated. In particular, proton reduction

dominates the charge passed at Pt surfaces in this work, regardless of the presence of an ANH or DHP in solution.

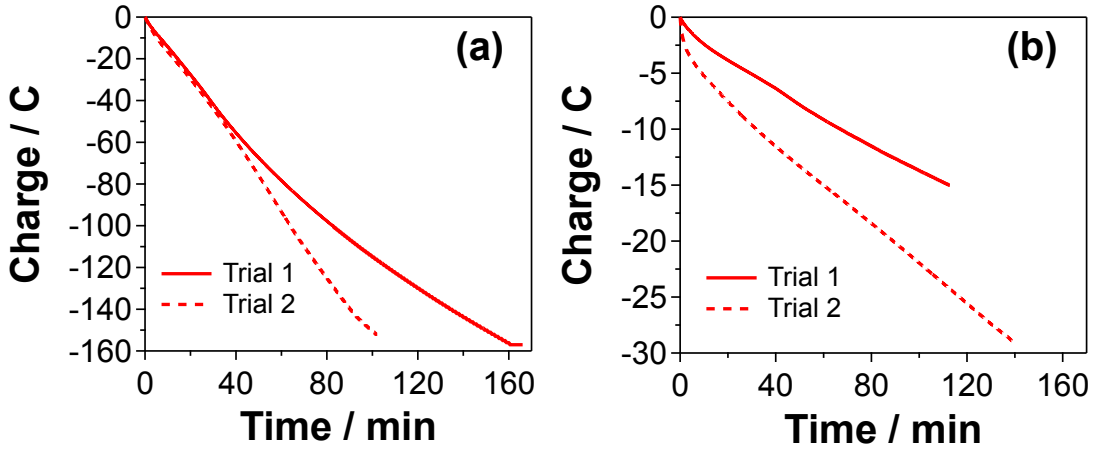

Figure 3.16. CPE plots for 1 mM **3-H$_2$** in the presence of 10 mM HCOOH at (a) Pt and (b) RVC mesh electrodes. *E* = -1.23 V vs. $FcH^{0/+}$; 0.1 M $LiClO_4$; 10% (v:v) H_2O/CH_3CN.

Comparison of the DHP CPE plots and the blank CPE plots shown in Figure 3.14 and Figure 3.16 showed no significant enhancement in the charge passed (140 C passed after 120 min for **3-H$_2$**, 150 C passed after 120 min for HCOOH alone at Pt surfaces; 14 C passed for both at RVC surfaces), indicating that the DHP reduction mechanism is a slow and minor process in solution. In contrast, a current enhancement was observed when a DHP was placed in a CO_2 saturated solution (see Chapter 2, Figure 2.11). No degradation of the DHP was observed over the course of the bulk electrolysis via ^{1}H NMR, indicating that little to none of the DHP reacted, or that it was consumed then regenerated during this reductive process (Figure 3.18a). Given that the %FEs observed are low, the methanol generation pathway appears to be much slower relative to proton reduction in the presence of formic acid for both **3** and **3-H$_2$**.

Table 3.4. Electrochemical Methanol Generation from Formic Acid in the Presence of **3-H_2.**

3-H_2:HCOOH[a]	$E_{applied}$[b]	**Electrode**	**Solvent**[c]	**[MeOH]**[d]	**%FE**[e] **MeOH**
1:10	-1.23	Pt	10% H_2O	32, ND	0.7, -
1:10	-1.23	RVC	10% H_2O	42, ND	9.7, -

[a]Ratio of DHP to HCOOH in mM. [b]V vs. $FcH^{0/+}$. [c]% (v:v) H_2O/CH_3CN. [d]in µM. [e]Faradaic Efficiency for Methanol Formation. Shown individually for each trial.

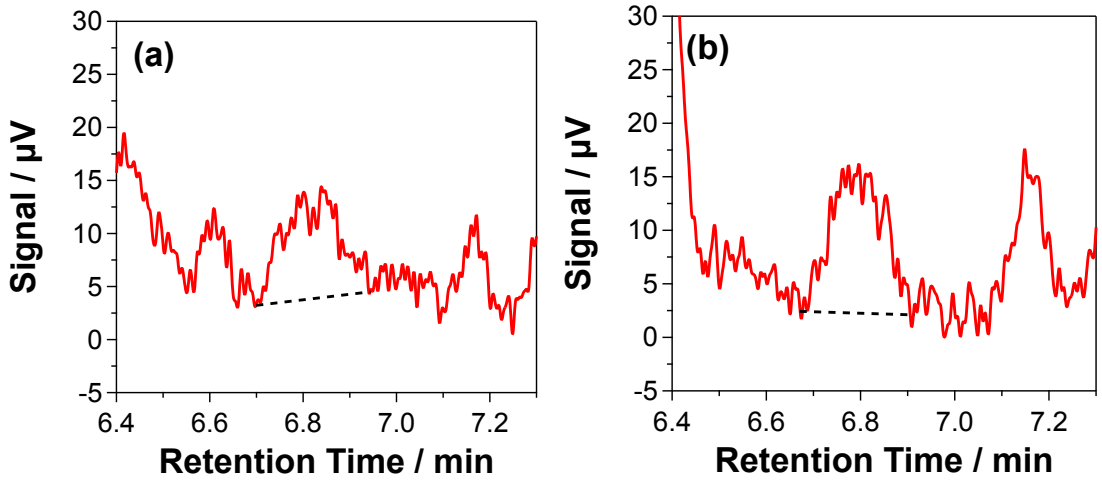

Figure 3.17. GC-FID Chromatograms of bulk electrolysis samples run at (a) Pt and (b) RVC mesh electrodes for 1 mM **3-H_2**: 10 mM HCOOH in 10% (v:v) H_2O/CH_3CN with $E_{applied}$ = -1.23 V vs. $FcH^{0/+}$. Dashed line indicates baseline used for peak integration.

To confirm the electrochemical generation of methanol from HCOOH in the presence of a DHP, an NMR scale reaction of HCOOH (27 µL, 0.73 mmol) and **3-H_2** (13 mg, 0.073 mmol) was conducted in 0.6 mL CD_3CN in a Teflon-capped J-Young valve NMR tube. The solution was allowed to sit for five hours at room temperature (the timescale of a bulk electrolysis experiment and bulb-to-bulb transfer) and the reaction monitored by ^1H NMR spectroscopy for any conversion of **3-H_2** to **3**, and any loss of HCOOH with the generation of methanol peaks. The NMR spectra are shown in Figure 3.18b, where an apparent growth of singlet peaks at 9.5 ppm, 5.4 ppm, 4.8 ppm, and 4.6 ppm is observed. When these peak integrals are compared to both the formic acid singlet

at 8.0 ppm and the CH_2 singlet of **3-H$_2$** at 4.3 ppm before and after five hours of reaction, the singlet peak at 4.8 ppm is found to grow in from 0.02 to 0.08 when compared to the CH_2 peak of **3-H$_2$** (set to a value of two), and corresponds to H_2 dissolved in solution.[88] Similarly, the singlet peak area at 9.5 ppm of **3** increases from 0.02 to 0.03 (when compared to a CH_2 peak area of two), while the CH_2 singlet peak area of **3-H$_2$** was found to decrease by 2% when compared to the formic acid peak, the dichloromethane peak, and the residual CD_3CN solvent peak. Furthermore, no singlets corresponding to methanol (~3.3 ppm) or formaldehyde (~9.8 ppm) formation was observed via ^{1}H NMR over the course of five hours under Ar conditions, indicating that a thermal reaction between the DHP and HCOOH is not occurring over the course of bulk electrolysis and product analysis. Rather, the only process observed was the formation of H_2 from the DHP, forming the ANH. This result agrees with the observed inactivity of the DHP towards CO_2 reduction (Chapter 2, Figure 2.19), indicating that an applied potential and electrode surface are required for the reduction of CO_2 and HCOOH to methanol using a DHP.[51, 67]

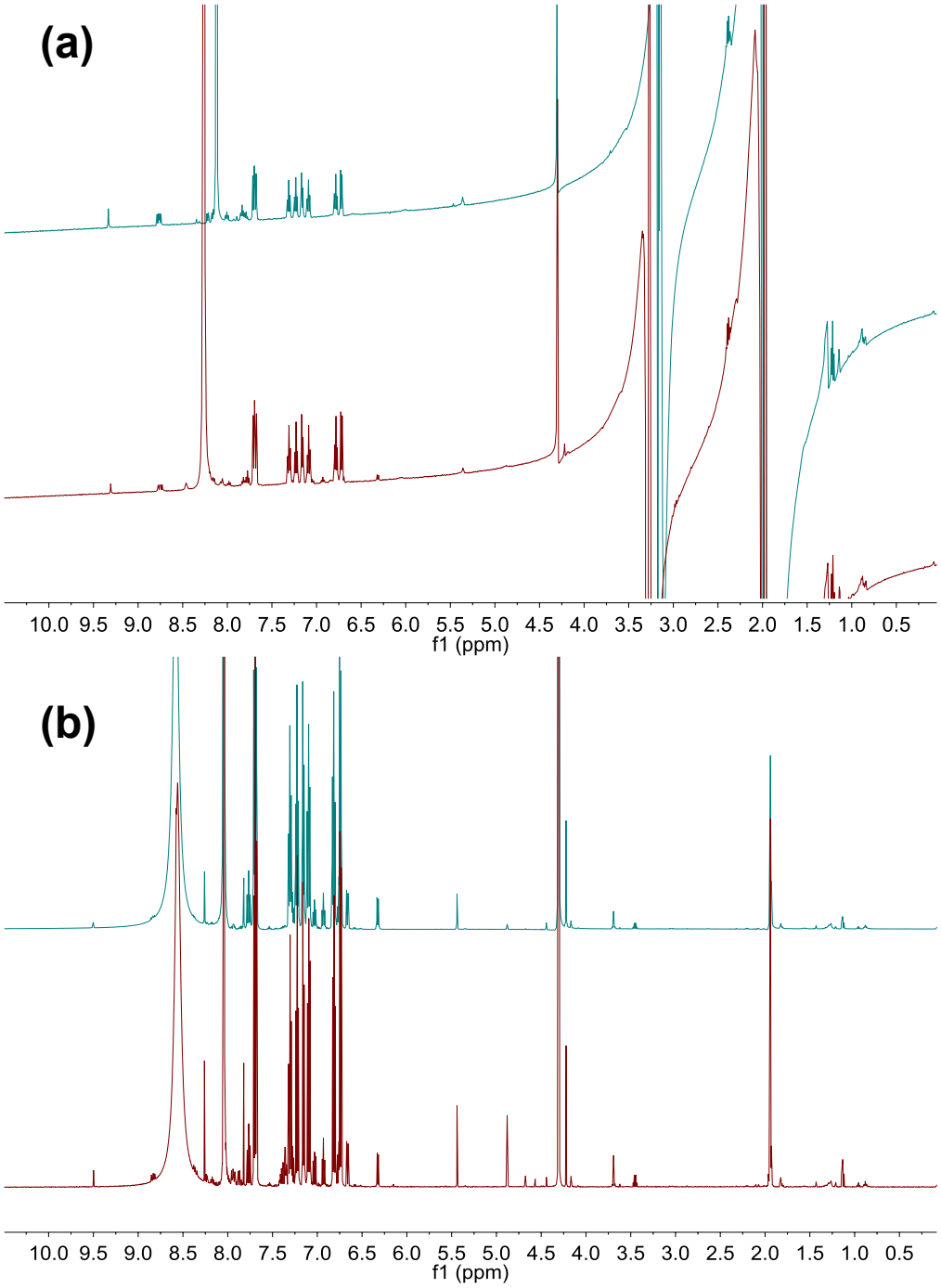

Figure 3.18. (a) ^{1}H NMR before (blue, top) and after (red, bottom) bulk electrolysis for 1 mM **3-H$_2$**: 10 mM HCOOH at Pt mesh electrode; $E_{applied}$ = -1.23 V vs. $FcH^{0/+}$; 10% (v:v) H_2O/CH_3CN. (b) ^{1}H NMR before (blue, top) and after five hours (red, bottom) for the thermal reaction of 121 mM **3-H$_2$**: 1.2 M HCOOH in CD_3CN.

Out of the series of ANHs investigated towards CO_2 reduction in Chapter 2, phenanthridine exhibited the lowest %FE towards CO_2 reduction, where it was argued

that this could be a result of its Pourbaix triple-point relative to CO_2-reducing conditions, as well as steric effects. Thus, to determine if the low yields of methanol was a result of the lower reactivity of **3** as the additive, pyridine and quinoline were also run under the same conditions, providing a dependence on the ANH present, particularly the effect of altering the pK_a, hydricity and size of the ANH used/potential DHP generated. No pyridine or quinoline DHP formation was observed above the background for bulk electrolyzed solutions containing pyridine or quinoline under the same conditions used for **3**, indicating that either (a) DHP formation from quinoline and pyridine was not occurring under the applied conditions; or (b) the DHP was formed then reacted over the course of the bulk electrolysis experiment. Furthermore, significant amounts of methanol were not observed (Figure 3.19), suggesting that the reduction mechanism of HCOOH relies on the interplay of the pK_a and hydricity of the ANH/DHP used (**3/3-H$_2$**), as well as the pH of the solution and the solvent mixture employed. This result agrees with work by Keith, where the ability to reduce CO_2, and thus HCOOH relies on the equilibrium between ANH/$[ANH\text{-}H]^+$/ANH-H_2, which is greatly affected by the solvent system and pH employed.[59] Since HCOOH was the substrate reduced in this work rather than CO_2, the optimal position of the ANH's triple point is likely altered from the positions obtained for CO_2 reduction (*vide infra*).

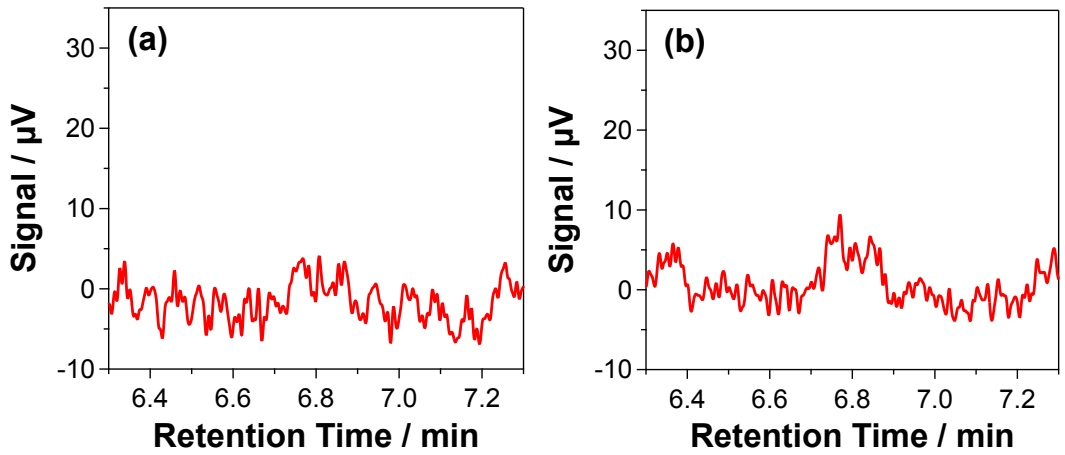

Figure 3.19. GC-FID Chromatograms of bulk electrolysis samples run at Pt electrodes for (a) 1 mM pyridine: 10 mM HCOOH; (b) 1 mM quinoline: 10 mM HCOOH, $E_{applied}$ = -1.23 V vs. $FcH^{0/+}$; 10% (v:v) H_2O/CH_3CN.

3.4 Discussion

The direct electrochemical reduction of formic acid under acidic conditions has been conducted at a number of metallic electrodes. At Pb and Sn electrodes, the generation of methanol was found to be strongly dependent on the potential window utilized (-0.9 to -1 V vs. SCE), with %FE for methanol production of up to 100% observed at Sn electrodes.[89] At Pt surfaces, no HCOOH reduction to methanol has been observed, but rather proton reduction was found to dominate at both the CV and bulk electrolysis time scale.[85] The use of Cu-electrodes and a Cu-Sn-Pb alloy was found to reduce formic acid to methanol at low %FE (~30%), with any increase in acid content resulting in acid reduction, inhibiting the HCOOH reduction pathway.[90] Furthermore, at Cu electrodes, the generation of a CO surface species was found to be key in the reduction pathway for formic acid.[30]

Recently, the ability of pyridine to reduce CO_2 at Pt surfaces was investigated using IR-spectroscopic techniques.[56] Under the applied potentials necessary for methanol production, the generation of CO and COOH surface species were observed, with the

COOH species than undergoing further reduction to HCOOH. Furthermore, no pyridine-based surface species was observed to form at chemically deposited Pt surfaces on a silicon wafer at potentials relevant to CO_2 reduction, suggesting that the reduction of CO_2 occurs via a mechanism similar to the proton-coupled, surface-hydride mediated process proposed by Batista (see Chapter 1, Figure 1.6). However, no methanol was detected in the study by Dunwell *et al.*,[56] potentially due to the different surface morphology and construction of the Pt electrode utilized compared to previous experimental methods, where Pt mesh (this work)[67] and Pt foil[43a] have been utilized with methanol observed. Since no methanol production was observed in this IR study, no computational, surface-based or (electro)chemical study of HCOOH reduction to methanol in the presence of ANH/DHP additives has been conducted to date. As such, the results presented in this Chapter will be cautiously compared to the mechanisms proposed computationally and spectroscopically for CO_2 reduction to HCOOH.

From the results presented herein, a mechanism towards methanol and DHP generation can be proposed. DHP generation was found to be strongly dependent on the applied potential, with the necessary potential dependent on the pH or Brønsted acidity of the acid used (compare DHP formation in perchloric acid and acetic acid solutions). This suggests that DHP formation is dependent on the formation of a surface hydride based on a 'weak acid' reduction mechanism. In solution, either a protonated ANH **[3-H]**$^+$ or the acid present is reduced by 1e$^-$ to form a surface hydride (H_{ads}), and **3** in the case of **[3-H]**$^+$, with the potential of this process strongly dependent on the pH of the solution and the electrode surface utilized. This is readily apparent at RVC surfaces, where from electrolyses and CV experiments, a larger overpotential is observed for proton reduction.

Furthermore, an increase in DHP formation is observed moving from Pt to RVC surfaces, indicating that surface-based interactions play an important role in DHP formation. As such, DHP formation is hypothesized to occur through a surface-coupled mechanism, whereby either (i) a surface-adsorbed ANH **3** is reduced by two H_{ads}/PCETs;[57b] (ii) **[3-H]**$^+$ is reduced by a $1e^-/1H^+$ process to a surface-adsorbed radical **[3-H]*** that is further reduced to a surface-adsorbed **3-H$_2$** which can dissociate;[57b] or (iii) a solution-based **[3-H]**$^+$ is reduced by H_{ads} in a $2e^-/1H^+$ reduction process (Figure 3.20).[53] These proposed mechanisms are similar to those proposed for DHP formation under CO_2 at p-GaP and Pt electrodes by Carter,[57b] Keith[54b, 57a, 58] and Batista.[53] Given the higher NMR conversions and %FE at RVC electrodes compared to Pt electrodes, it is expected that a surface-adsorbed mechanism is more likely to result in the formation of a DHP.

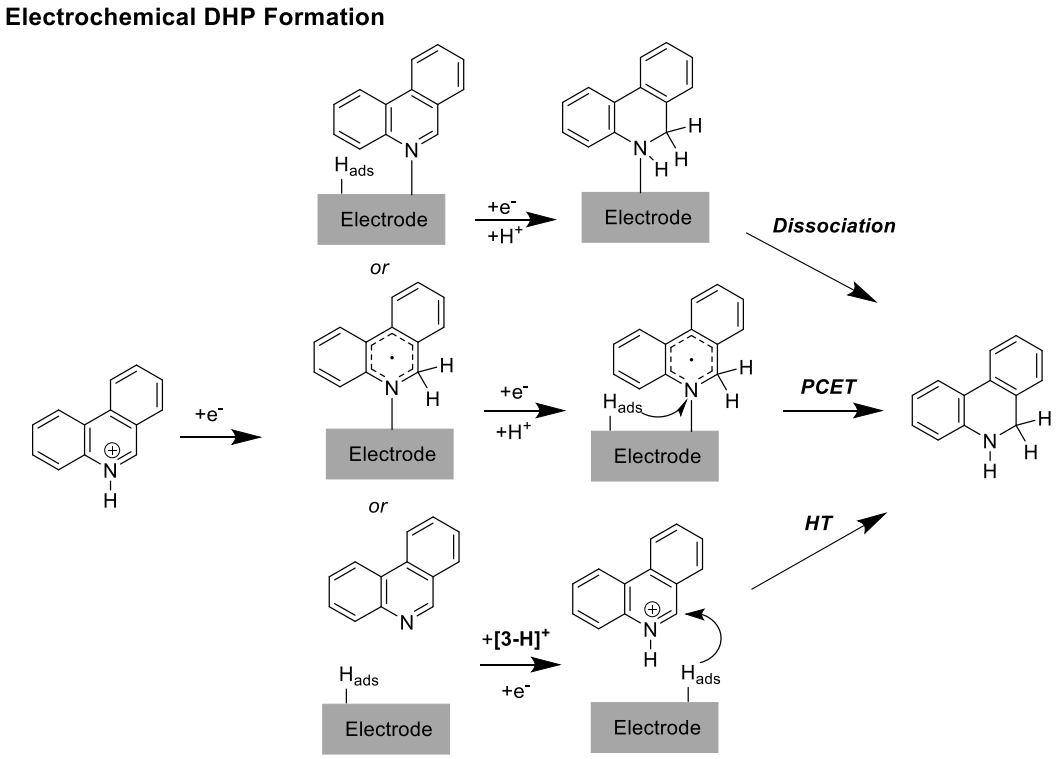

Figure 3.20. Proposed mechanisms for electrochemical formation of **3-H$_2$**. In the acidic conditions employed, either the acid or **[3-H]**$^+$ is reduced to form H_{ads} and a surface adsorbed **3** (top) that can undergo another $1H^+/1e^-$ to **3-H$_2$** that can dissociate from the surface; a surface-based **[3-H]*** (middle) that can undergo a $1H^+/1e^-$ reduction to **3-H$_2$** and dissociate from the surface; or form H_{ads} and a solution-phase **3** (bottom), where a secondary **[3-H]**$^+$ can be reduced to **3-H$_2$** through a HT ($1H^+/2e^-$ transfer) by H_{ads}.

Since no reaction occurred between chemically synthesized DHP and HCOOH in the absence of an applied potential and electrode surface, a surface-coupled reaction mechanism towards HCOOH reduction to methanol is also likely. In ANH-based solutions, the reduction of HCOOH could occur via any of three distinct mechanisms, similar to the mechanisms proposed by Carter and Batista (Figure 3.21). Similar to a solution-based formation of the DHP, **[3-H]**$^+$ and a H_{ads} can reduce HCOOH through a proton-coupled hydride transfer (PCHT), forming formaldehyde and water, with a secondary PCHT step producing methanol (mechanism shown in Chapter 1, Figure 1.6).[53] Alternatively, a surface based **3-H$_2$** can be generated, which can then attack

HCOOH through direct hydride transfer (HT), which is either coupled with, or followed by proton transfer (PT), forming formaldehyde and **3**, with a secondary PCHT in the same fashion producing methanol from formaldehyde.[57b]

While DHP solutions exhibited larger %FE for methanol generation at RVC surfaces, the methanol concentration generated was similar to ANH solutions under the same conditions, indicating that this process is a slow process that exhibits a large energy barrier to methanol formation, and is occurring at similar rates in both DHP and ANH-containing solutions. Given that no degradation of the DHP to the parent ANH was observed via ^{1}H NMR spectroscopy during bulk electrolyses or in thermal reactions with HCOOH, we hypothesize that the DHP reacts with a H_{ads}, generating H_2 to form a surface-adsorbed **[3-H_2]*** that can then undergo a secondary reduction and perform a HT to HCOOH that is coupled with a PT, generating formaldehyde and **3** at the surface (Figure 3.21). This newly generated **3** can then be reduced through one of the mechanisms from ANH-based reduction, regenerating the DHP.

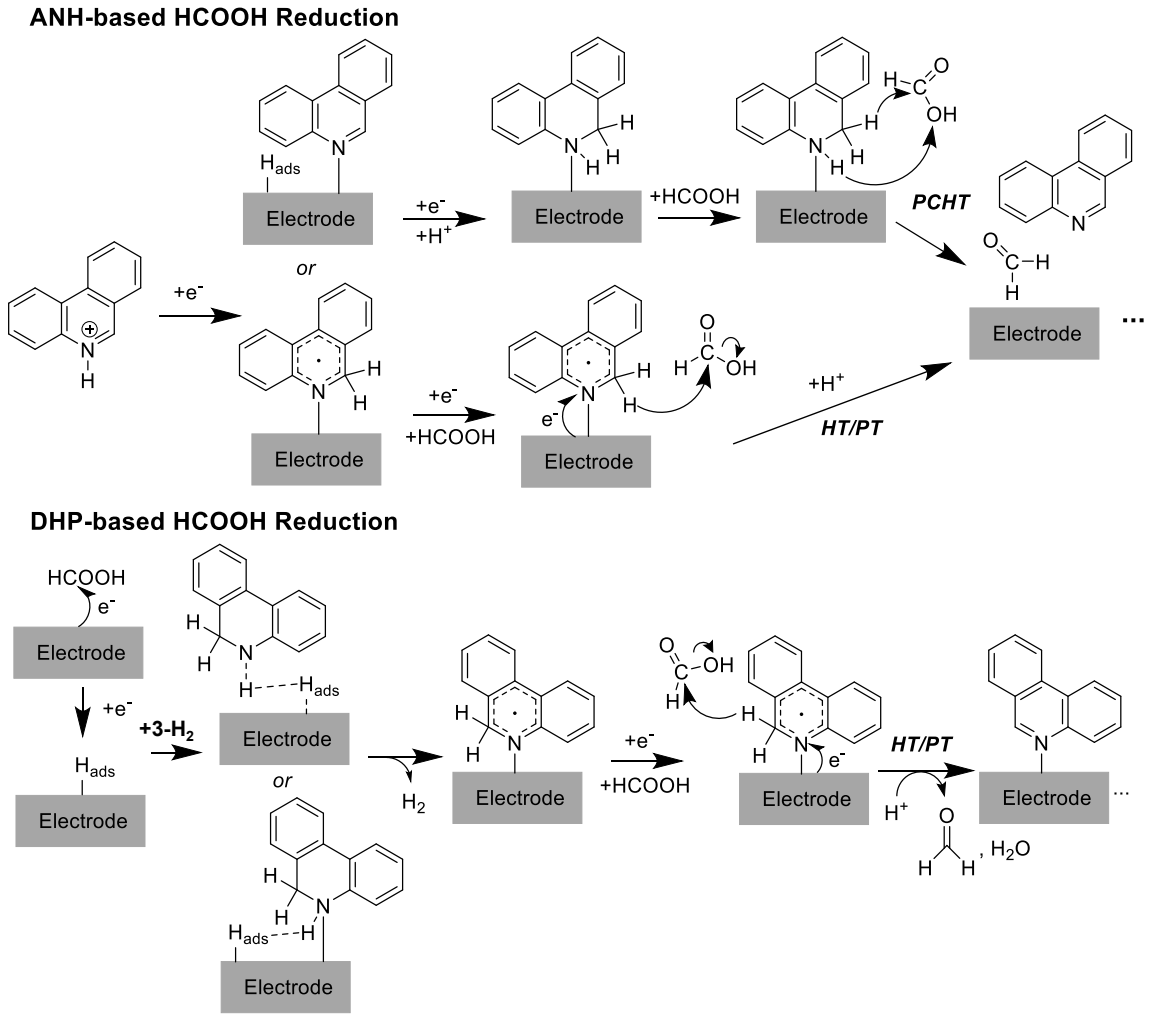

Figure 3.21. Proposed mechanisms for formic acid reduction to methanol facilitated by ANH or DHP. In the acidic conditions employed, either the acid or **[3-H]**$^+$ is reduced to form H_{ads} and a surface adsorbed **3** (top) that can undergo another $1H^+/1e^-$ to **3-H$_2$** that can attack HCOOH in a PCHT fashion, with **3** dissociating from the surface; a surface-based **[3-H]*** (middle) that can undergo a $1e^-$ reduction and attack HCOOH through a HT followed by a PT. For DHP reduction of HCOOH, the DHP reacts with a surface hydride, generating H_2 and a surface-adsorbed **[3-H]*** radical that can undergo a $1e^-$ reduction and attack HCOOH through a HT followed by a PT.

Analysis of the charge passed in the presence of **3-H$_2$** to that passed in the presence of HCOOH alone reveals little to no charge enhancement due to the addition of the DHP. Furthermore, CVs of DHP under acidic conditions revealed little to no current being passed (Chapter 2, Figure 2.8). Thus it is not expected that proton reduction can occur through a DHP route at a comparable rate to acid reduction. Rather, once the DHP

is generated, it is unlikely that it will generate **3** and H_2 in the timeframe and conditions employed, and the large amount of charge passed at Pt surfaces in the presence of **3** and HCOOH compared to HCOOH alone is more likely from the **3**/**[3-H]**$^+$ couple than a result of the **3**/**3-H$_2$** couple. This is consistent with a low reactivity of the ANH/DHP towards the reduction of HCOOH.

Attempts at HCOOH reduction using quinoline and pyridine as the ANH did not produce any observable amounts of methanol, with none of their corresponding DHPs observed via ^{1}H NMR, suggesting that DHP formation either did not occur, or the DHPs are too reactive to be observed using the methods employed here. Computational studies by Keith have predicted that the ability of the ANH to facilitate CO_2 reduction, and thus HCOOH reduction to methanol, was due to the position of its Pourbaix triple-point of ANH/[ANH-H]$^+$/DHP in relation to the pH and applied potential necessary for CO_2 reduction to HCOOH.[59] All three of these species have been observed through electrochemical and ^{1}H NMR techniques for **3** under the acidic conditions applied. Since the pH of the solutions involved in HCOOH reduction in this work are more acidic (pH ~ 1-3), it is expected that an ANH with a lower pK_a and thus a more acidic Pourbaix triple point can facilitate HCOOH reduction to methanol more readily than ANHs more apt for CO_2 reduction to HCOOH at higher pH values (pH ~5), under similar applied potentials to that utilized for CO_2 reduction. **3** fits this criterion, whereas pyridine and quinoline exhibit higher pK_a values and thus more basic Pourbaix triple points that can facilitate CO_2 or HCOOH reduction more readily at higher pH values, and as a result, may not be able to undergo HCOOH reduction and DHP formation as readily under the experimental conditions studied.

3.5 Conclusion

We have presented here the first evidence of an electrochemical generation of a DHP with simultaneous generation of methanol under conditions relevant to CO_2 reduction. The generation of the DHP was found to be dependent on the applied potential/pH, solvent mixture and surface used, with high NMR conversions and %FE at RVC surfaces. Methanol was generated at both Pt and RVC electrodes under electrochemically reducing conditions at low %FEs, with similar, low concentrations being observed for ANH and DHP based solutions. Furthermore, the identity of the ANH/DHP used was critical for methanol and DHP production, with neither observed above the limit of detection in pyridine or quinoline solutions. Based on the low %FEs and TONs, it appears that formic acid reduction is the limiting step in CO_2 reduction to methanol for ANH-based electrochemical systems. These findings will hopefully further the investigation into these synergistic type of reaction schemes, particularly in overcoming the barrier towards formic acid reduction, where optimizing the proton-hydride shuttle interaction with the electrode surface, substrate, applied potential, and solvent mixture is expected to increase the TON in electrochemical hydrogenation frameworks.[83]

CHAPTER 4: Conclusions and Outlook

In this thesis, the ability of benzannulated pyridines and their corresponding dihydropyridines to mediate the electrochemical reduction of CO_2 to liquid fuel products such as formic acid and methanol was investigated. While the simplest variant, pyridine, has been studied extensively in the literature (see Chapter 1) using electrochemical, chemical and computational techniques, little is still known as to the exact role it and its dihydro-variant plays in the facilitation of methanol production from CO_2. This work sought to elucidate mechanistic insights by altering the electronic structure of pyridine through benzannulation, as well as develop and use isolable 1,2-DHP and 1,4-DHP variants to determine their significance in the CO_2 reduction mechanism.

In Chapter 2, pyridine was found to exhibit the highest selectivity towards methanol production, while quinoline exhibited the highest Faradaic efficiency of the benzannulated series. This was taken as an indication that a balance between the size, the acidity and the hydricity of the ANH/DHP utilized, i.e. its Pourbaix triple point,[59a] for CO_2 reduction plays a significant role in determining which ANH will reduce CO_2. Access to the *para*-position of the ANH was found to lead to significant deposition processes using acridine, while access to the *ortho*-position of the ANH did not in the case of phenanthridine, indicating that the configuration of the different DHP isomers has a significant contribution towards any surface-based interactions. The DHPs investigated also required the use of an electrode and an applied surface to facilitate CO_2 and HCOOH reduction, indicating that an electrochemical surface-coupled reduction is likely to occur, as proposed by Carter,[57b] Keith,[54b, 57a] and Batista.[53] Furthermore, 1,2-dihydrophenanthridine was found to exhibit an observable current enhancement both at

the CV and electrolysis timescale not associated with weak acid buffering, unlike the ANHs investigated, with %FE towards methanol and formic acid production that were electrode independent.

In Chapter 3, the reduction of HCOOH to methanol was observed in the presence of either phenanthridine or 1,2-dihydrophenanthridine, with similar TON and TOF as seen for CO_2 reduction to methanol. Thus, if HCOOH is an intermediate in the CO_2 reduction process, its reduction appears to be turnover-limiting. Furthermore, simultaneous DHP and methanol generation was observed under conditions relevant for CO_2 reduction using phenanthridine, but not with quinoline or pyridine, where no methanol or DHP generation was observed in this work. This result indicates that the position of the ANH's Pourbaix triple point must be at more acidic pH values to facilitate HCOOH reduction to methanol under the experimental conditions employed.

While CO_2 and HCOOH reduction are reported in this work, the amounts of methanol and formic acid produced are low. Methanol and formic acid generated were confirmed to not be a result of a contamination in the ANH/DHP, degradation of the ANH/DHP, a contaminant in the CO_2/HCOOH used, a contaminant from post-electrolysis processing, or a contaminant from the electrode setups used. Future work might investigate the ability to conduct CO_2 reduction and HCOOH reduction to methanol using isotopic labeling, such as the use of $^{13}C^{16}O_2$; $^{12}C^{18}O_2$; D_2O/CD_3CN as the solvent; DCOOD; $H^{13}COOH$ and/or deuterated pyridine, with determination of products using high-resolution GC-MS/LC-MS, ^1H NMR, ^2H NMR, and ^{13}C NMR spectroscopy. Furthermore, application of deuterated DHP species could provide definitive proof of the role DHPs play in CO_2 reduction. These isotopically-labeled species would provide

spectroscopic and spectrometric handles to observe the exact origin of the CO_2 and HCOOH reduced species produced in this system, which might help alleviate much of the controversy associated with this promising system.[48, 56, 61]

In this work, both ANH and DHPs are observed to help facilitate the reduction of CO_2 to methanol, with both species proposed to undergo a surface adsorption process in order to do so. As such, future work could investigate the role of ANH/DHPs at the electrode surface for CO_2 reduction using IR-spectroscopic techniques, as described by Dunwell *et al*.[56] This would allow observation of any N-H, CH_2, C-N, and C=N bonds either adsorbed on the electrode surface or in solution near the electrode surface. From this, the degradation pathway of the DHP to the ANH under CO_2 reducing conditions, as well as the surface-adsorption process observed for acridine at Pt and RVC surfaces, could be better understood, helping determine the exact mechanism ANH/DHP-based CO_2 reduction undergoes.

The majority of the studies involving pyridine-based CO_2 reduction involve the use of pyridine-containing solutions, with only a few studies investigating the interaction at the electrode surface spectroscopically.[43b, 56] By instead tethering the pyridine ring to the electrode surface, any surface-adsorbed processes can be suppressed with the promotion of solution-based CO_2 reduction. Recent work has investigated the ability of pyridine-functionalized Au surfaces to reduce CO_2 to HCOOH and CO, with pyridine appended in the *para*-position.[91] Similarly, the appendage of pyridine to other surfaces such as Pt and carbon can be investigated, whereby any surface adsorption processes that pyridine can undergo are suppressed. Alkene monolayers have been recently appended onto Pt surfaces through oxidation of the Pt-surface.[92] Carbon electrodes can be

functionalized through reduction of a diazonium pyridine salt, or with pyridine covalently attached to graphene/graphene oxide.[81a, 93] By investigating these functionalized surfaces electrochemically and spectroscopically, the ability of pyridine to facilitate CO_2 reduction to methanol without any pyridine-based adsorption processes can be observed.

Another avenue currently being explored is the use of the acidic conditions employed in Chapter 3 to perform hydrogenation reactions of unsaturated bonds such as imines and ketones to their corresponding amines and alcohols. This will not only help determine the generality of the 1,2-dihydrophenanthridine formation observed in Chapter 3 to other unsaturated substrates, but also allow the possibility for asymmetric hydrogenation using electrochemical methods. It is expected that from these results a more facile, environmentally friendly, industrial-scale hydrogenation framework can be developed.

APPENDIX

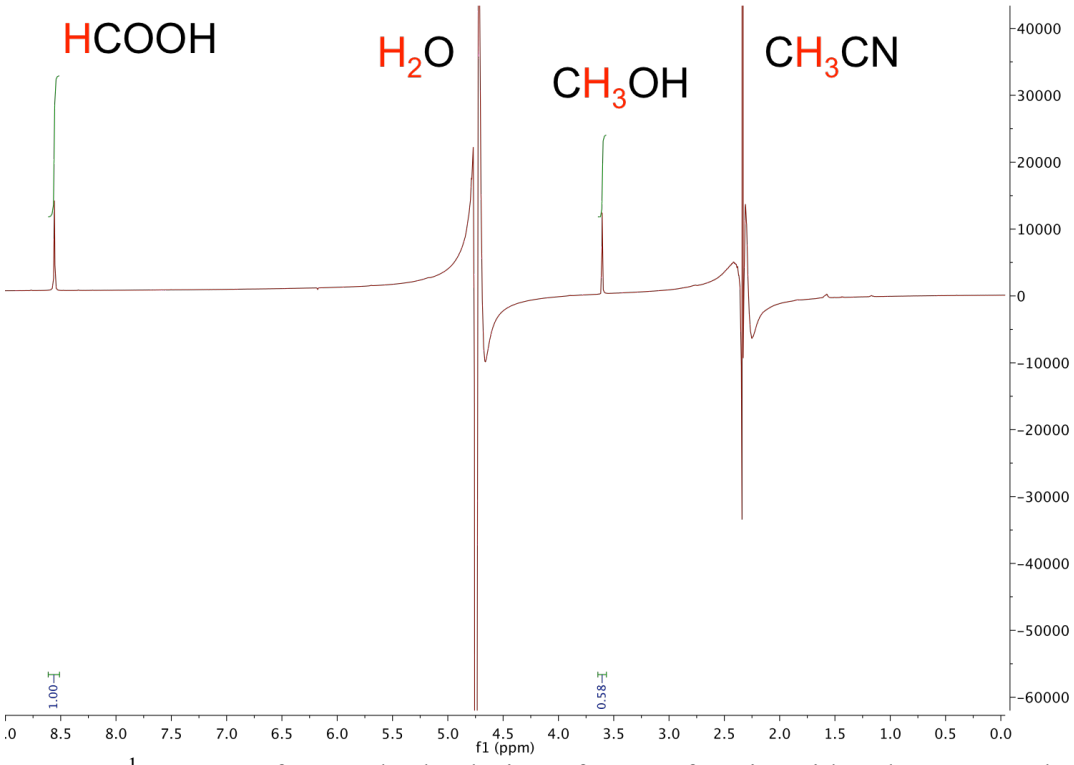

Figure A1. ^{1}H NMR of a standard solution of 5 mM formic acid and 5 mM methanol in 40% v/v CH_3CN/H_2O. As shown, a suppression of the CH_3OH signal of approximately 5x is observed. Taken from Reference [67]. Copyright 2017 American Chemical Society.

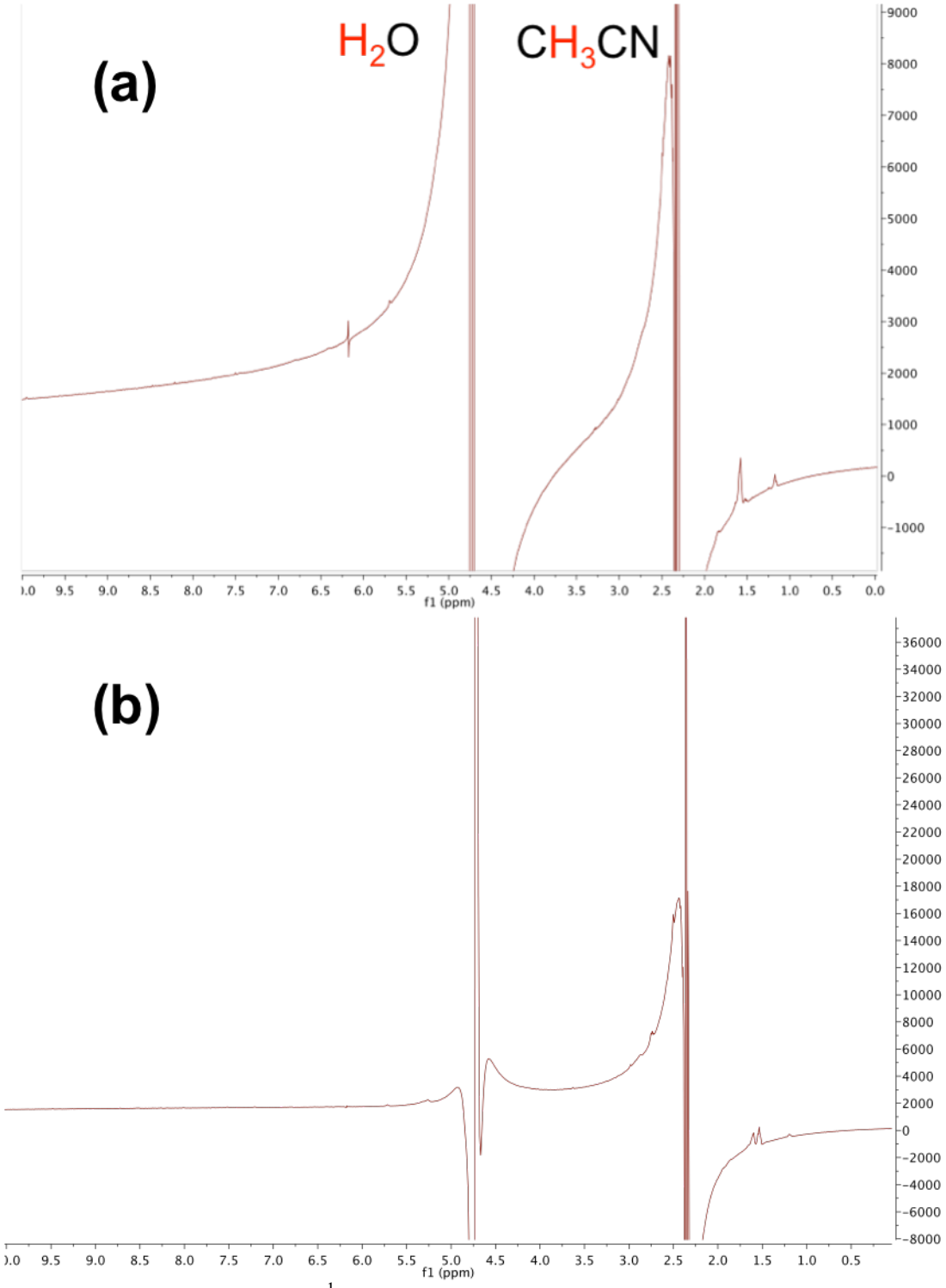

Figure A2. Representative ^{1}H NMR spectrum of an aliquot taken from a bulk electrolysis by a (a) Pt and a (b) RVC electrode under CO_2. 0.1 M $LiClO_4$, 60% (v:v) H_2O/CH_3CN. Adapted from Reference [67]. Copyright 2017 American Chemical Society.

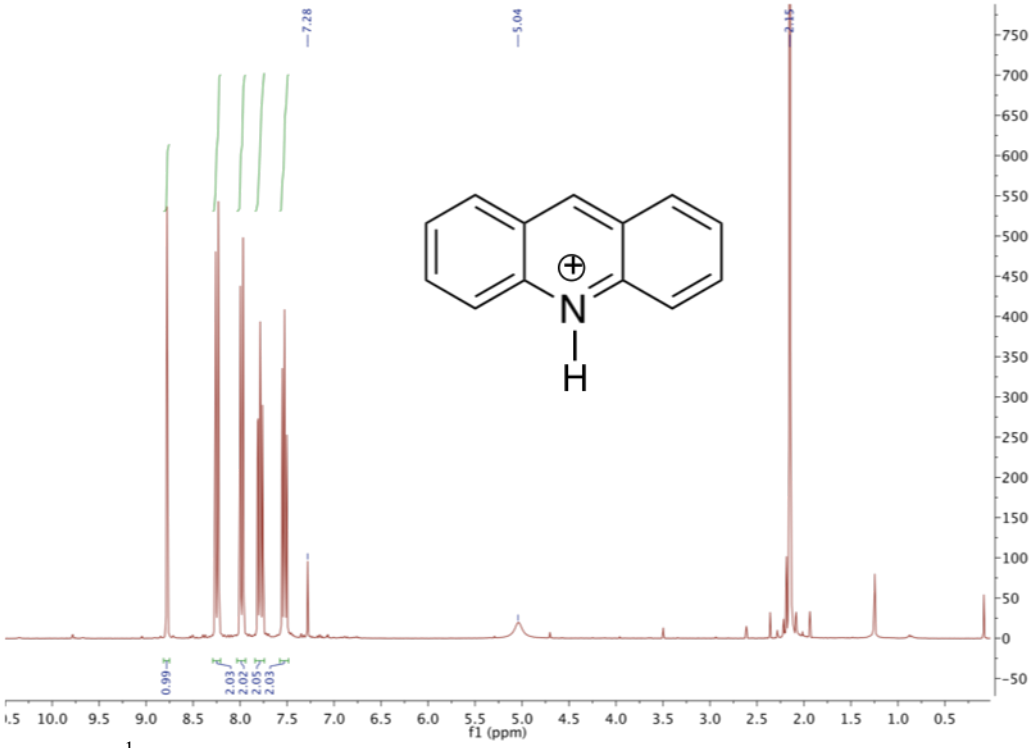

Figure A3. ^{1}H NMR ($CDCl_3$) of film deposit of **4** after 1 CV cycle under CO_2 at a GCE (see Figure 2.5). No **4-H$_2$** observed, only peaks corresponding to **[4-H]$^+$** are observed in the aromatic region. Solvent peaks indicated in spectrum. Adapted from Reference [67]. Copyright 2017 American Chemical Society.

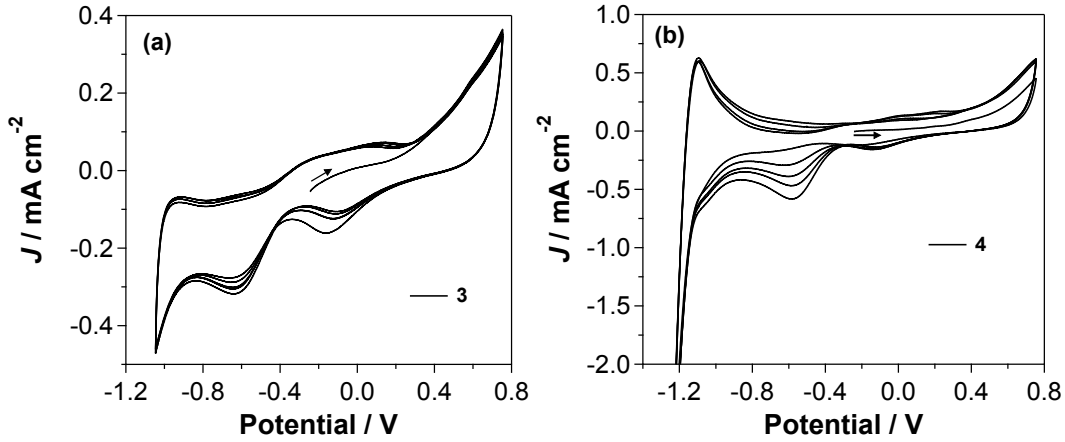

Figure A4. Anodic CV scans of (a) **3** and (b) **4** in 0.1 M $LiClO_4$ at pH of 5.5; 60% (v:v) H_2O/CH_3CN. Scan rate of 100 mV/s, Pt disk electrode; Potential referenced vs. $FcH^{0/+}$. Taken from Reference [67]. Copyright 2017 American Chemical Society.

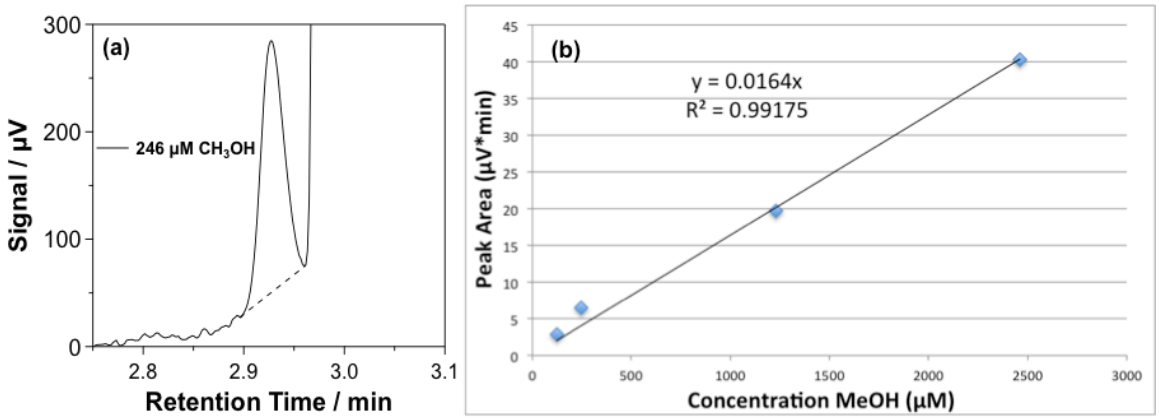

Figure A5. (a) GC-FID Chromatogram of a methanol (CH_3OH) standard solution. (b) Calibration curve of the peak area vs. methanol (MeOH) concentration in 60% (v:v) H_2O/CH_3CN for GC-FID detection. Adapted from Reference [67]. Copyright 2017 American Chemical Society.

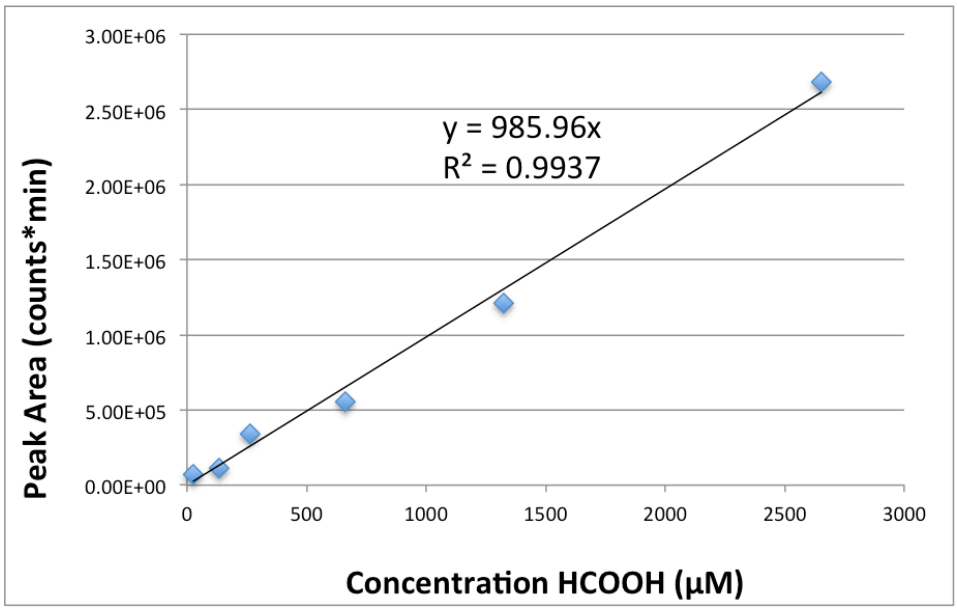

Figure A6. LC-MS calibration curve of peak area vs. formic acid concentration in 60% (v:v) H_2O/CH_3CN (M/Z = -45 Da). Taken from Reference [67]. Copyright 2017 American Chemical Society.

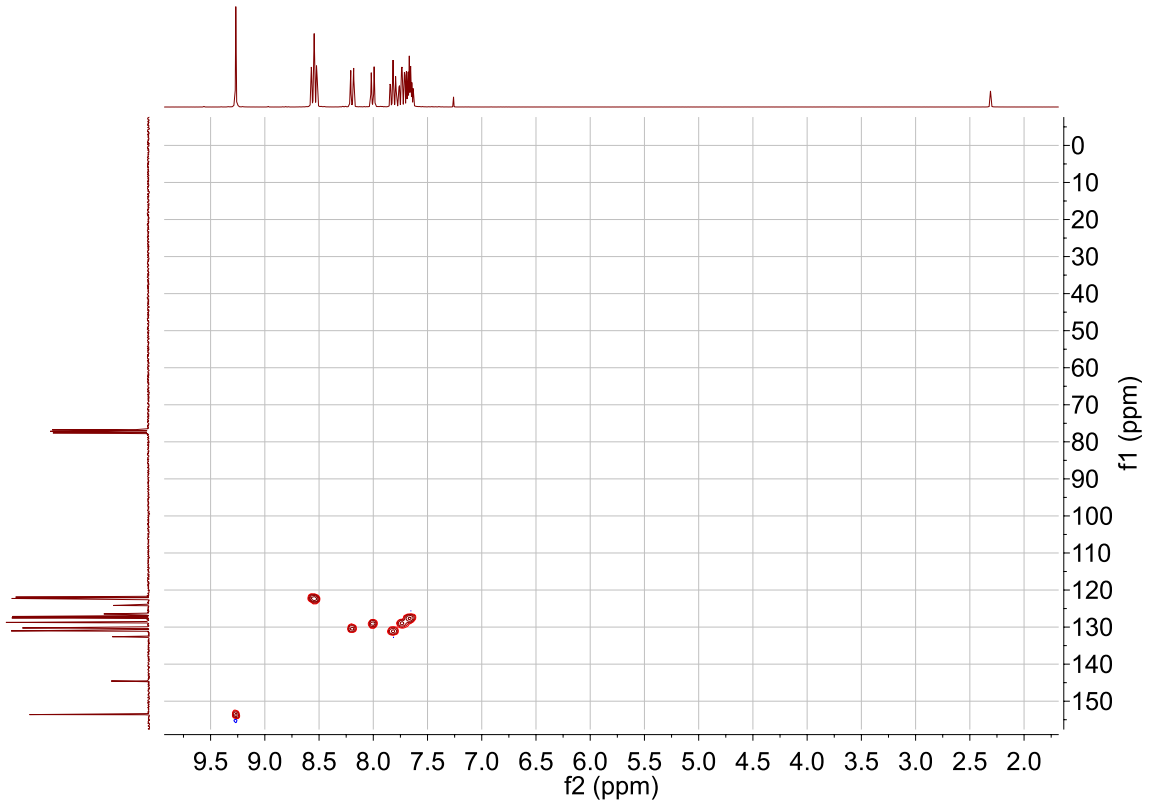

Figure A7. HSQC-DEPT Spectrum of **3** in $CDCl_3$.

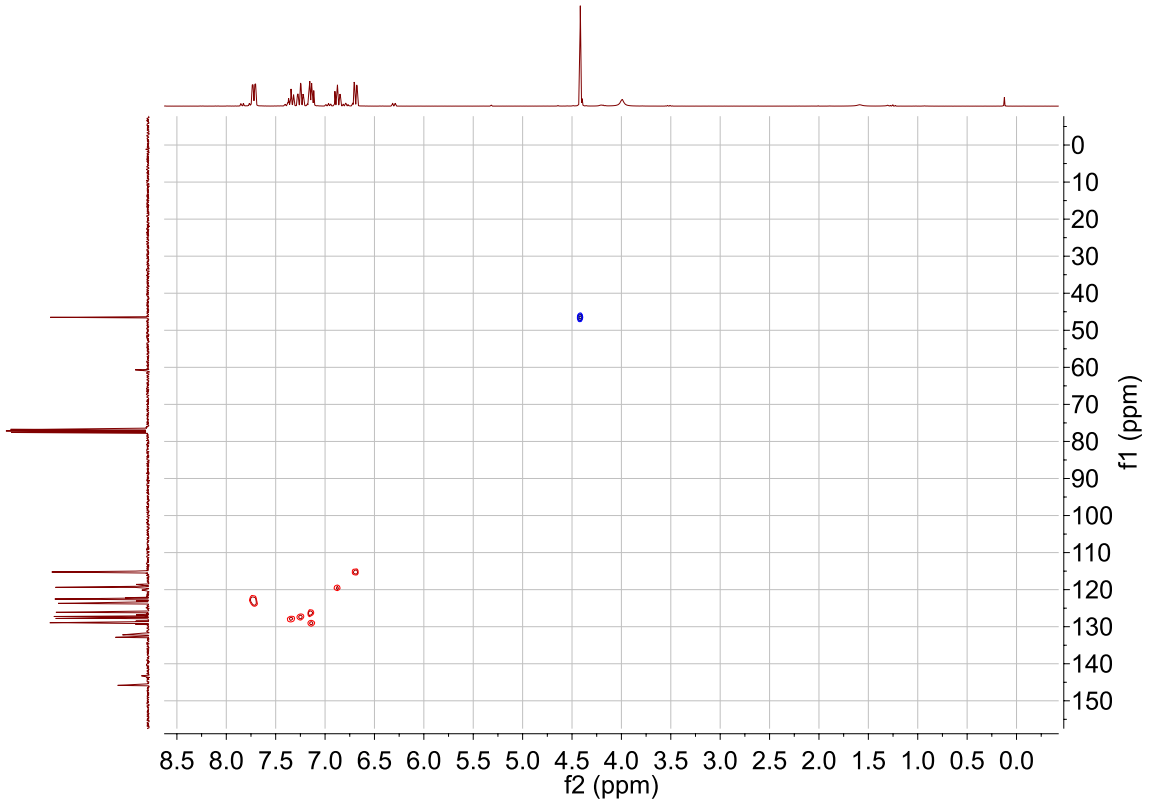

Figure A8. HSQC-DEPT Spectrum of **3-H_2** in $CDCl_3$.

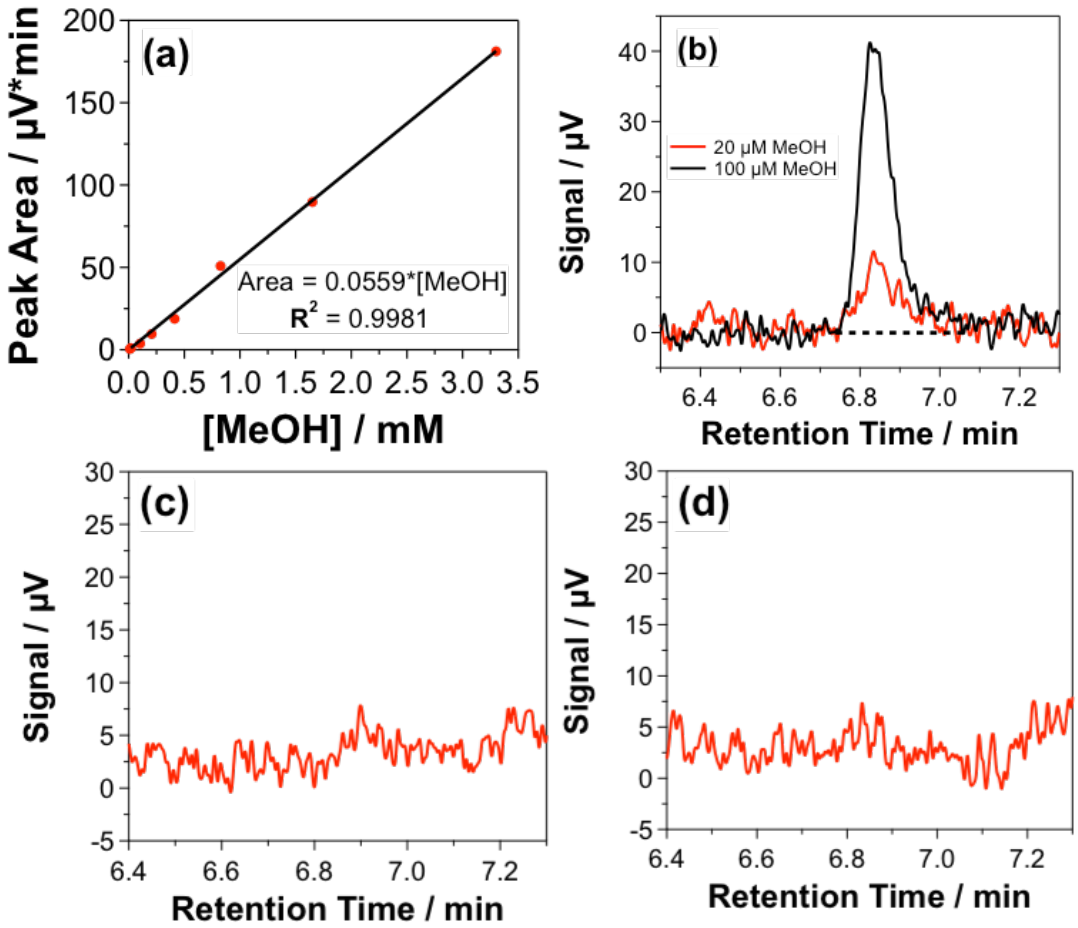

Figure A9. (a) Calibration curve of GC-FID Peak Area versus Concentration of MeOH. (b) Corresponding GC-FID chromatograms for 20 and 100 μM CH_3OH in 10% (v:v) H_2O/CH_3CN. Dashed line indicates baseline used for peak integration. GC-FID Chromatograms of bulk electrolysis control samples run at (c) Pt and (d) RVC mesh electrodes for 10 mM HCOOH, $E_{applied}$ = -1.23 V vs. $FcH^{0/+}$; 10% (v:v) H_2O/CH_3CN. No methanol observed.

REFERENCES

1. Lewis, N. S.; Nocera, D. G., Powering the Planet: Chemical Challenges in Solar Energy Utilization. *Proceedings of the National Academy of Sciences of the United States of America* **2006,** *103* (43), 15729-35.
2. DOE Energy Sources. https://energy.gov/science-innovation/energy-sources (accessed July 10).
3. (a) Gray, H. B., Powering the Planet with Solar Fuel. *Nat. Chem.* **2009,** *1* (1), 7; (b) Administration, U. S. E. I. Solar Energy and the Environment. https://www.eia.gov/energyexplained/?page=solar_environment (accessed July 11).
4. E.A.C, A National Grid Energy Storage Strategy. 2014.
5. (a) Winter, M.; Brodd, R. J., What Are Batteries, Fuel Cells, and Supercapacitors? *Chem. Rev.* **2004,** *104* (10), 26; (b) Kang, D. H. P.; Chen, M.; Ogunseitan, O. A., Potential Environmental and Human Health Impacts of Rechargeable Lithium Batteries in Electronic Waste. *Environ. Sci. and Tech.* **2013,** *47* (10), 9; (c) Janek, J.; Zeier, W. G., A Solid Future for Battery Development. *Nat. Energy* **2016,** *1*, 4.
6. Barnhart, C. J.; Benson, S. M., On the Importance of Reducing the Energetic and Material Demands of Electrical Energy Storage. *Energy Environ. Sci.* **2013,** *6* (4), 10.
7. Hammarström, L.; Hammes-Schiffer, S., Artificial Photosynthesis and Solar Fuels. *Acc. Chem. Res.* **2009,** *42* (12), 2.
8. Nocera, D. G., Chemistry of Personalized Solar Energy. *Inorg. Chem.* **2009,** *48* (21), 17.
9. Walter, M. G.; Warren, E. L.; McKone, J. R.; Boettcher, S. W.; Mi, Q.; Santori, E. A.; Lewis, N. S., Solar Water Splitting Cells. *Chem. Rev.* **2010,** *110* (11), 6446-73.
10. DOE Hydrogen Production: Natural Gas Reforming. https://energy.gov/eere/fuelcells/hydrogen-production-natural-gas-reforming (accessed July 19).
11. Demirel, Y., *Energy Production, Conversion, Storage, Conservation, and Coupling*. Springer: 2012.
12. Appel, A. M.; Bercaw, J. E.; Bocarsly, A. B.; Dobbek, H.; DuBois, D. L.; Dupuis, M.; Ferry, J. G.; Fujita, E.; Hille, R.; Kenis, P. J.; Kerfeld, C. A.; Morris, R. H.; Peden, C. H.; Portis, A. R.; Ragsdale, S. W.; Rauchfuss, T. B.; Reek, J. N.; Seefeldt, L. C.; Thauer, R. K.; Waldrop, G. L., Frontiers, opportunities, and challenges in biochemical and chemical catalysis of CO_2 fixation. *Chem. Rev.* **2013,** *113* (8), 6621-58.
13. Kumar, B.; Llorente, M.; Froehlich, J.; Dang, T.; Sathrum, A.; Kubiak, C. P., Photochemical and Photoelectrochemical Reduction of CO_2. *Annu. Rev. Phys. Chem.* **2012,** *63*, 541-69.
14. ExxonMobil Synthetic Fuels. http://corporate.exxonmobil.com/en/company/worldwide-operations/catalysts-and-licensing/synthetic-fuels (accessed July 20).
15. Alvarez, A.; Bansode, A.; Urakawa, A.; Bavykina, A. V.; Wezendonk, T. A.; Makkee, M.; Gascon, J.; Kapteijn, F., Challenges in the Greener Production of Formates/Formic Acid, Methanol, and DME by Heterogeneously Catalyzed CO_2 Hydrogenation Processes. *Chem. Rev.* **2017**.
16. Eppinger, J.; Huang, K.-W., Formic Acid as a Hydrogen Energy Carrier. *ACS Energy Letters* **2017,** *2*, 8.

17. Rice, C.; Ha, S.; Masel, R. I.; Wieckowski, A., Catalysts for Direct Formic Acid Fuel Cells. *J. Power Sources* **2003,** *115* (2), 7.
18. (a) Singh, M. R.; Bell, A. T., Design of an Artificial Photosynthetic System for Production of Alcohols in High Concentration from CO_2. *Energy Environ. Sci.* **2016,** *9* (1), 7; (b) Wang, W.-H.; Himeda, Y.; Muckerman, J. T.; Manbeck, G. F.; Fujita, E., CO_2 Hydrogenation to Formate and Methanol as an Alternative to Photo- and Electrochemical CO_2 Reduction. *Chem. Rev.* **2015,** *115* (23), 38.
19. Arcoumanis, C.; Bae, C.; Crookes, R.; Kinoshita, E., The Potential of di-methyl Ether (DME) as an Alternative Fuel for Compression-ignition Engines: A review. *Fuel* **2008,** *87*, 17.
20. Benson, E. E.; Kubiak, C. P.; Sathrum, A. J.; Smieja, J. M., Electrocatalytic and Homogeneous Approaches to Conversion of CO_2 to Liquid Fuels. *Chem. Soc. Rev.* **2009,** *38*, 11.
21. Tomita, Y.; Teruya, S.; Koga, O.; Hori, Y., Electrochemical Reduction of Carbon Dioxide at a Platinum Electrode in Acetonitrile-Water Mixtures. *J. Electrochem. Soc.* **2000,** *147* (11), 4.
22. Costentin, C.; Savéant, J. M., Catalysis of the Electrochemical Reduction of Carbon Dioxide. *Chem. Soc. Rev.* **2013,** *42*, 14.
23. Yamazaki, Y.; Takeda, H.; Ishitani, O., Photocatalytic Reduction of CO_2 using Metal Complexes. *J. Photochem. and Photobio. C: Photochem. Rev.* **2015,** *25*, 32.
24. Boston, D. J.; Xu, C.; Armstrong, D. W.; MacDonnell, F. M., Photochemical Reduction of Carbon Dioxide to Methanol and Formate in a Homogeneous System with Pyridinium Catalysts. *J. Am. Chem. Soc.* **2013,** *135* (44), 16252-5.
25. Tamaki, Y.; Ishitani, O., Supramolecular Photocatalysts for the Reduction of CO_2. *ACS Catalysis* **2017,** *7* (5), 16.
26. Hagfeldt, A.; Boschloo, G.; Sun, L.; Kloo, L.; Pettersson, H., Dye-Sensitized Solar Cells. *Chem. Rev.* **2010,** *110* (11), 6595-6663.
27. White, J. L.; Herb, J. T.; Kaczur, J. J.; Majsztrik, P. W.; Bocarsly, A. B., Photons to Formate: Efficient Electrochemical Solar Energy Conversion via Reduction of Carbon Dioxide. *J. of CO_2 Utilization* **2014,** *7*, 1-5.
28. (a) Machan, C. W.; Chabolla, S. A.; Yin, J.; Gilson, M. K.; Tezcan, F. A.; Kubiak, C. P., Supramolecular Assembly Promotes the Electrocatalytic Reduction of Carbon Dioxide by Re(I) Bipyridine Catalysts at a Lower Overpotential. *J. Am. Chem. Soc.* **2014,** *136* (41), 14598-607; (b) Machan, C. W.; Sampson, M. D.; Chabolla, S. A.; Dang, T.; Kubiak, C. P., Developing a Mechanistic Understanding of Molecular Electrocatalysts for CO_2 Reduction using Infrared Spectroelectrochemistry. *Organomet.* **2014,** *33* (18), 4550-4559; (c) Machan, C. W.; Sampson, M. D.; Kubiak, C. P., A Molecular Ruthenium Electrocatalyst for the Reduction of Carbon Dioxide to CO and Formate. *J. Am. Chem. Soc.* **2015,** *137* (26), 8564-71; (d) Riplinger, C.; Sampson, M. D.; Ritzmann, A. M.; Kubiak, C. P.; Carter, E. A., Mechanistic Contrasts Between Manganese and Rhenium Bipyridine Electrocatalysts for the Reduction of Carbon Dioxide. *J. Am. Chem. Soc.* **2014,** *136* (46), 16285-98.
29. Bernskoetter, W. H.; Hazari, N., Reversible Hydrogenation of Carbon Dioxide to Formic Acid and Methanol: Lewis Acid Enhancement of Base Metal Catalysts. *Acc. Chem. Res.* **2017,** *50* (4), 1049-1058.

30. Qiao, J.; Liu, Y.; Hong, F.; Zhang, J., A Review of Catalysts for the Electroreduction of Carbon Dioxide to Produce Low-Carbon Fuels. *Chem. Soc. Rev.* **2014,** *43*, 45.
31. Kuhl, K. P.; Cave, E. R.; Abram, D. N.; Jaramillo, T. F., New Insights into the Electrochemical Reduction of Carbon Dioxide on Metallic Copper Surfaces. *Energy Environ. Sci.* **2012,** *5* (5), 7050.
32. Hori, Y.; Kikuchi, K.; Murata, A.; Suzuki, S., Production of Methane and Ethylene in Electrochemical Reduction of Carbon Dioxide at Copper Electrodes in Aqueous Hydrogen Carbonate Solution. *Chem. Lett.* **1986**, 2.
33. Hori, Y.; Murata, A.; Takahashi, R., Formation of Hydrocarbons in the Electrochemical Reduction of Carbon Dioxide at a Copper Electrode in Aqueous Solution. *J. Chem. Soc. Faraday Trans.* **1989,** *85* (8), 18.
34. Schouten, K. J. P.; Qin, Z.; Gallent, E. P.; Koper, M. T. M., Two Pathways for the Formation of Ethylene in CO Reduction on Single-Crystal Copper Electrodes. *J. Am. Chem. Soc.* **2012,** *134* (24), 4.
35. Durand, W. J.; Peterson, A. A.; Studt, F.; Abild-Pedersen, F.; Norskov, J. K., Structure Effects on the Energetics of the Electrochemical Reduction of CO_2 by Copper Surfaces. *Surf. Sci.* **2011,** *605* (15), 6.
36. Tang, W.; Peterson, A. A.; Varela, A. S.; Jovanov, Z. P.; Bech, L.; Durand, W. J.; Dahl, S.; Norskov, J. K.; Chorkendorff, I., The Importance of Surface Morphology in Controlling the Selectivity of Polycrystalline Copper for CO_2 Electroreduction. *Phys. Chem. Chem. Phys.* **2012,** *14* (1), 6.
37. Vasileff, A.; Zheng, Y.; Qiao, S. Z., Carbon Solving Carbon's Problems: Recent Progress of Nanostructured Carbon-Based Catalysts for the Electrochemical Reduction of CO_2. *Adv. Energy Mater.* **2017**.
38. Wu, J.; Ma, S.; Sun, J.; Gold, J. I.; Tiwary, C.; Kim, B.; Zhu, L.; Chopra, N.; Odeh, I. N.; Vajtai, R.; Yu, A. Z.; Luo, R.; Lou, J.; Ding, G.; Kenis, P. J. A.; Ajayan, P. M., A Metal-free Electrocatalyst for Carbon Dioxide Reduction to Multi-Carbon Hydrocarbons and Oxygenates. *Nat. Commun.* **2016,** *7*, 13869.
39. Oh, S.; Gallagher, J. R.; Miller, J. T.; Surendranath, Y., Graphite-Conjugated Rhenium Catalysts for Carbon Dioxide Reduction. *J. Am. Chem. Soc.* **2016,** *138* (6), 1820-1823.
40. Hinogami, R.; Nakamura, Y.; Yae, S.; Nakato, Y., An Approach to Ideal Semiconductor Electrodes for Efficient Photoelectrochemical Reduction of Carbon Dioxide by Modification with Small Metal Particles. *J. Phys. Chem. B* **1998,** *102* (6), 974-980.
41. Barton, E. E.; Rampulla, D. M.; Bocarsly, A. B., Selective Solar-Driven Reduction of CO_2 to Methanol Using a Catalyzed p-GaP Based Photoelectrochemical Cell. *J. Am. Chem. Soc.* **2008,** *130*, 3.
42. Bocarsly, A. B.; Gibson, Q. D.; Morris, A. J.; L'Esperance, R. P.; Detweiler, Z. M.; Lakkaraju, P. S.; Zeitler, E. L.; Shaw, T. W., Comparative Study of Imidazole and Pyridine Catalyzed Reduction of Carbon Dioxide at Illuminated Iron Pyrite Electrodes. *ACS Catalysis* **2012,** *2* (8), 1684-1692.
43. (a) Cole, E. B.; Lakkaraju, P. S.; Rampulla, D. M.; Morris, A. J.; Abelev, E.; Bocarsly, A. B., Using a One-Electron Shuttle for the Multielectron Reduction of CO_2 to Methanol: Kinetic, Mechanistic, and Structural Insights. *J. Am. Chem. Soc.* **2010,** *132*,

13; (b) Peroff, A. G.; Weitz, E.; Van Duyne, R. P., Mechanistic Studies of Pyridinium Electrochemistry: Alternative Chemical Pathways in the Presence of CO_2. *Phys. Chem. Chem. Phys.* **2016,** *18* (3), 1578-1586.
44. Seshadri, G.; Lin, C.; Bocarsly, A. B., A New Homogeneous Electrocatalyst for the Reduction of Carbon Dioxide to Methanol at Low Overpotential. *J. Electroanal. Chem.* **1994,** *372*, 6.
45. Lucio, A. J.; Shaw, S. K., Pyridine and Pyridinium Electrochemistry on Polycrystalline Gold Electrodes and Implications for CO_2 Reduction. *J. Phys. Chem. C* **2015**, 150522120921004.
46. Lebègue, E.; Agullo, J.; Morin, M.; Bélanger, D., The Role of Surface Hydrogen Atoms in the Electrochemical Reduction of Pyridine and CO2 in Aqueous Electrolyte. *ChemElectroChem* **2014,** *1* (6), 1013-1017.
47. Rybchenko, S. I.; Touhami, D.; Wadhawan, J. D.; Haywood, S. K., Study of Pyridine-Mediated Electrochemical Reduction of CO_2 to Methanol at High CO_2 Pressure. *ChemSusChem* **2016,** *9* (13), 1660-1669.
48. Costentin, C.; Canales, J. C.; Haddou, B.; Saveant, J. M., Electrochemistry of Acids on Platinum. Application to the Reduction of Carbon Dioxide in the Presence of Pyridinium Ion in Water. *J. Am. Chem. Soc.* **2013,** *135* (47), 17671-4.
49. Morris, A. J.; McGibbon, R. T.; Bocarsly, A. B., Electrocatalytic Carbon Dioxide Activation: The Rate-Determining Step of Pyridinium-Catalyzed CO2 Reduction. *ChemSusChem* **2011,** *4* (2), 191-196.
50. Yuan, J.; Hao, C., Solar-driven Photoelectrochemical Reduction of Carbon Dioxide to Methanol at $CuInS_2$ Thin Film Photocathode. *Sol. Energy Mater. and Sol. Cells* **2013,** *108*, 170-174.
51. Yan, Y.; Zeitler, E. L.; Gu, J.; Hu, Y.; Bocarsly, A. B., Electrochemistry of Aqueous Pyridinium: Exploration of a Key Aspect of Electrocatalytic Reduction of CO_2 to Methanol. *J. Am. Chem. Soc.* **2013,** *135* (38), 14020-3.
52. Barton Cole, E. E.; Baruch, M. F.; L'Esperance, R. P.; Kelly, M. T.; Lakkaraju, P. S.; Zeitler, E. L.; Bocarsly, A. B., Substituent Effects in the Pyridinium Catalyzed Reduction of CO_2 to Methanol: Further Mechanistic Insights. *Top. Catal.* **2014,** *58* (1), 15-22.
53. Ertem, M. Z.; Konezny, S. J.; Araujo, C. M.; Batista, V. S., Functional Role of Pyridinium during Aqueous Electrochemical Reduction of CO_2 on Pt(111). *J. Phys. Chem. Lett.* **2013,** *4* (5), 745-748.
54. (a) Keith, J. A.; Carter, E. A., Theoretical Insights into Pyridinium-based Photoelectrocatalytic Reduction of CO_2. *J. Am. Chem. Soc.* **2012,** *134* (18), 7580-3; (b) Keith, J. A.; Carter, E. A., Electrochemical Reactivities of Pyridinium in Solution: Consequences for CO_2 Reduction Mechanisms. *Chem. Sci.* **2013,** *4* (4), 1490.
55. (a) Lim, C. H.; Holder, A. M.; Hynes, J. T.; Musgrave, C. B., Role of Pyridine as a Biomimetic Organo-hydride for Homogeneous Reduction of CO_2 to Methanol; (b) Lim, C. H.; Holder, A. M.; Hynes, J. T.; Musgrave, C. B., Reduction of CO_2 to Methanol Catalyzed by a Biomimetic Organo-Hydride Produced from Pyridine. *J. Am. Chem. Soc.* **2014,** *136* (45), 16081-95.
56. Dunwell, M.; Yan, Y.; Xu, B., In Situ Infrared Spectroscopic Investigations of Pyridine-Mediated CO_2 Reduction on Pt Electrocatalysts. *ACS Catalysis* **2017**, 5410-5419.

57. (a) Keith, J. A.; Carter, E. A., Theoretical Insights into Electrochemical CO_2 Reduction Mechanisms Catalyzed by Surface-Bound Nitrogen Heterocycles. *J. Phys. Chem. Lett.* **2013,** *4* (23), 4058-4063; (b) Lessio, M.; Senftle, T. P.; Carter, E. A., Is the Surface Playing a Role during Pyridine-Catalyzed CO_2 Reduction on p-GaP Photoelectrodes? *ACS Energy Letters* **2016,** *1* (2), 464-468.
58. Keith, J. A.; Muñoz-García, A. B.; Lessio, M.; Carter, E. A., Cluster Models for Studying CO_2 Reduction on Semiconductor Photoelectrodes. *Top. Catal.* **2014,** *58* (1), 46-56.
59. (a) Groenenboom, M. C.; Saravanan, K.; Zhu, Y.; Carr, J. M.; Marjolin, A.; Faura, G. G.; Yu, E. C.; Dominey, R. N.; Keith, J. A., Structural and Substituent Group Effects on Multielectron Standard Reduction Potentials of Aromatic N-Heterocycles. *J. Phys. Chem. A* **2016**; (b) Marjolin, A.; Keith, J. A., Thermodynamic Descriptors for Molecules That Catalyze Efficient CO_2 Electroreductions. *ACS Catalysis* **2015,** *5* (2), 1123-1130.
60. Xiang, D.; Magana, D.; Dyer, R. B., CO_2 Reduction Catalyzed by Mercaptopteridine on Glassy Carbon. *J. Am. Chem. Soc.* **2014,** *136* (40), 14007-10.
61. Saveant, J.-M.; Tard, C., Attempts to Catalyze the Electrochemical CO_2-to-Methanol Conversion by Biomimetic $2e^- + 2H^+$ Transferring Molecules. *J. Am. Chem. Soc.* **2016,** *138* (3), 1017-1021.
62. Lim, C.-H.; Holder, A. M.; Hynes, J. T.; Musgrave, C. B., Dihydropteridine/Pteridine as a $2H^+/2e^-$ Redox Mediator for the Reduction of CO_2 to Methanol: A Computational Study. *J. Phys. Chem. B* **2017,** *121* (16), 4158-4167.
63. Bard, A. J.; Faulkner, L. R., *Electrochemical Methods: Fundamentals and Applications*. 2 ed.; Wiley: 2000.
64. (a) McCarthy, B. D.; Martin, D. J.; Rountree, E. S.; Ullman, A. C.; Dempsey, J. L., Electrochemical Reduction of Brønsted Acids by Glassy Carbon in Acetonitrile-Implications for Electrocatalytic Hydrogen Evolution. *Inorg. Chem.* **2014,** *53* (16), 8350-61; (b) Rountree, E. S.; McCarthy, B. D.; Eisenhart, T. T.; Dempsey, J. L., Evaluation of Homogeneous Electrocatalysts by Cyclic Voltammetry. *Inorg. Chem.* **2014,** *53* (19), 9983-10002.
65. Costentin, C.; Savéant, J.-M., Multielectron, Multistep Molecular Catalysis of Electrochemical Reactions: Benchmarking of Homogeneous Catalysts. *ChemElectroChem* **2014,** *1* (7), 1226-1236.
66. Barrette, W. C.; Johnson, H. W.; Sawyer, D. T., Voltammetric evaluation of the effective acidities (pKa') for Brønsted acids in aprotic solvents. *Anal. Chem.* **1984,** *56* (11), 1890-1898.
67. Giesbrecht, P. K.; Herbert, D. E., Electrochemical Reduction of Carbon Dioxide to Methanol in the Presence of Benzannulated Dihydropyridine Additives. *ACS Energy Letters* **2017,** *2* (3), 549-555.
68. Kronawitter, C. X.; Lessio, M.; Zahl, P.; Muñoz-García, A. B.; Sutter, P.; Carter, E. A.; Koel, B. E., Orbital-Resolved Imaging of the Adsorbed State of Pyridine on GaP(110) Identifies Sites Susceptible to Nucleophilic Attack. *J. Phys. Chem. C* **2015,** *119* (52), 28917-28924.
69. Maksić, Z. B.; Barić, D.; Müller, T., Clar's Sextet Rule Is a Consequence of the σ-Electron Framework. *J. Phys. Chem. A* **2006,** *110* (33), 10135-10147.

70. Lu, L.-Q.; Li, Y.; Junge, K.; Beller, M., Iron-Catalyzed Hydrogenation for the In Situ Regeneration of an NAD(P)H Model: Biomimetic Reduction of α-Keto-/α-Iminoesters. *Angew. Chem. Int. Ed.* **2013,** *52* (32), 8382-8386.
71. Tanner, D. D.; Yang, C.-M., On the Structure and Mechanism of Formation of the Lansbury Reagent, Lithium Tetrakis(N-dihydropyridyl)aluminate. *J. Org. Chem.* **1993,** *58* (7), 7.
72. Lanning, J. A.; Chambers, J. Q., Voltammetric Study of the Hydrogen Ion/Hydrogen Couple in Acetonitrile/Water Mixtures. *Anal. Chem.* **1973,** *45* (7), 7.
73. Hamann, C. H.; Schmöde, P., Electric Current from the Direct Conversion of Low Molecular Weight C,H,O-compounds. *J. Power Sources* **1976,** *1* (2), 141-157.
74. Barbosa, J.; Sanz-Nebot, V., Preferential Solvation in Acetonitrile-Water Mixtures. *J. Chem. Soc. Faraday Trans.* **1994,** *90* (21), 6.
75. Nørskov, J. K.; Bligaard, T.; Logadottir, A.; Kitchin, J. R.; Chen, J. G.; Pandelov, S.; Stimming, U., Trends in the Exchange Current for Hydrogen Evolution. *J. Electrochem. Soc.* **2005,** *152* (3), J23.
76. Lim, C. H.; Holder, A. M.; Musgrave, C. B., Mechanism of Homogeneous Reduction of CO_2 by Pyridine: Proton Relay in Aqueous Solvent and Aromatic Stabilization. *J. Am. Chem. Soc.* **2013,** *135* (1), 142-54.
77. Anne, A.; Moiroux, J., Redox Potentials and Acid-Base Equilibria of NADH/NAD^+ Analogs in Acetonitrile. *J. Org. Chem.* **1990,** *55* (15), 4608-4614.
78. Chen, L. D.; Urushihara, M.; Chan, K.; Nørskov, J. K., Electric Field Effects in Electrochemical CO_2 Reduction. *ACS Catalysis* **2016,** *6* (10), 7133-7139.
79. Yuan, J.; Zheng, L.; Hao, C., Role of Pyridine in Photoelectrochemical Reduction of CO_2 to Methanol at a $CuInS_2$ Thin Film Electrode. *RSC Advances* **2014,** *4* (74), 39435-39438.
80. Yang, N.; Waldvogel, S. R.; Jiang, X., Electrochemistry of Carbon Dioxide on Carbon Electrodes. *ACS Appl. Mater. Interfaces* **2016,** *8* (42), 28357-28371.
81. (a) Shul, G.; Weissmann, M.; Bélanger, D., Electrochemical Characterization of Glassy Carbon Electrode Modified with 1,10-Phenanthroline Groups by Two Pathways: Reduction of the Corresponding Diazonium Ions and Reduction of Phenanthroline. *Electrochimica Acta.* **2015,** *162*, 146-155; (b) Shul, G.; Weissmann, M.; Bélanger, D., Electrochemical Formation of an Ultrathin Electroactive Film from 1,10-Phenanthroline on a Glassy Carbon Electrode in Acidic Electrolyte. *Langmuir* **2014,** *30* (22), 6612-6621.
82. Froehlich, J. D.; Kubiak, C. P., Homogeneous CO_2 Reduction by Ni(cyclam) at a Glassy Carbon Electrode. *Inorg. Chem.* **2012,** *51* (7), 3.
83. (a) Murase, M.; Kitahara, G.; Suzuki, T. M.; Ohta, R., Efficient Catalytic Electrode for CO_2 Reduction Realized by Physisorbing Ni(cyclam) Molecules with Hydrophobicity Based on Hansen's Theory. *ACS Appl. Mater. Interfaces* **2016,** *8*, 4; (b) Maurin, A.; Robert, M., Noncovalent Immobilization of a Molecular Iron-Based Electrocatalyst on Carbon Electrodes for Selective, Efficient CO_2-to-CO Conversion in Water. *J. Am. Chem. Soc.* **2016,** *138*, 4.
84. Chen, Q. A.; Gao, K.; Duan, Y.; Ye, Z. S.; Shi, L.; Yang, Y.; Zhou, Y. G., Dihydrophenanthridine: A New and Easily Regenerable NAD(P)H Model for Biomimetic Asymmetric Hydrogenation. *J. Am. Chem. Soc.* **2012,** *134* (4), 2442-8.

85. Miles, M. H.; Fletcher, A. N.; McManis, G. E., Electrochemical Reduction Reactions involving Formic Acid. *J. Electroanal. Chem. and Interfacial Chem.* **1984,** *163* (1), 429-436.
86. Gottlieb, H. E.; Kotlyar, V.; Nudelman, A., NMR Chemical Shifts of Common Laboratory Solvents as Trace Impurities. *J. Org. Chem.* **1997,** *62* (21), 7512-7515.
87. Portenkirchner, E.; Enengl, C.; Enengl, S.; Hinterberger, G.; Schlager, S.; Apaydin, D.; Neugebauer, H.; Knör, G.; Sariciftci, N. S., A Comparison of Pyridazine and Pyridine as Electrocatalysts for the Reduction of Carbon Dioxide to Methanol. *ChemElectroChem* **2014,** *1* (9), 1543-1548.
88. Fulmer, G. R.; Miller, A. J. M.; Sherden, N. H.; Gottlieb, H. E.; Nudelman, A.; Stoltz, B. M.; Bercaw, J. E.; Goldberg, K. I., NMR Chemical Shifts of Trace Impurities: Common Laboratory Solvents, Organics, and Gases in Deuterated Solvents Relevant to the Organometallic Chemist. *Organomet.* **2010,** *29* (9), 2176-2179.
89. Russell, P. G.; Kovac, N.; Srinivasan, S.; Steinberg, M., The Electrochemical Reduction of Carbon Dioxide, Formic Acid, and Formaldehyde. *J. Electrochem. Soc.* **1977,** *124* (9), 10.
90. (a) Kotoulas, I.; Schizodimou, A.; Kyriacou, G., Electrochemical Reduction of Formic Acid on a Copper-Tin-Lead Cathode. *The Open Electrochemistry Journal* **2013,** *5*, 5; (b) Schizodimou, A.; Kotoulas, I.; Kyriacou, G., Electrochemical Reduction of Formic Acid through its Decarbonylation in Phosphoric Acid Solution. *Electrochimica Acta.* **2016,** *210*, 236-239.
91. Fang, Y.; Flake, J. C., Electrochemical Reduction of CO_2 at Functionalized Au Electrodes. *J. Am. Chem. Soc.* **2017,** *139* (9), 3399-3405.
92. Alonso, J. M.; Fabre, B.; Trilling, A. K.; Scheres, L.; Franssen, M. C. R.; Zuilhof, H., Covalent Attachment of 1-Alkenes to Oxidized Platinum Surfaces. *Langmuir* **2015,** *31* (9), 2714-2721.
93. Hoseini, S. J.; Khozestan, H. G.; Fath, R. H., Covalent attachment of 3-(aminomethyl)pyridine to graphene oxide: a new stabilizer for the synthesis of a palladium thin film at the oil-water interface as an effective catalyst for the Suzuki-Miyaura reaction. *RSC Adv.* **2015,** *5* (59), 47701-47708.